Development and Characterization of a Directional Radiation Detection System Using a Fuzzy Logic Algorithm

A Dissertation Presented for the

Doctor of Philosophy

Degree

The University of Tennessee, Knoxville

Michael Joseph Willis

December 2015

© by Michael Joseph Willis, 2015
All Rights Reserved.

This work is dedicated to my wife, Kayla, whose unwavering support and love have been my guide. To my son, Colton, parents, family, friends, mentors, co-workers, thank you for your love, prayers, and encouragement.

Acknowledgements

Many individuals have helped me in the completion of this Ph.D. research. I would like to thank my Ph.D. advisor, Dr. Steven Skutnik, who has patiently guided and motivated me in accomplishing this research. I would also like to thank Dr. Howard Hall for his support from the beginning of this project and allowing me the opportunity to work on it. My wife, Kayla, has been my rock throughout my scholastic endeavors, and without her love I would not be where I am today. To my parents and brother, thank you for your love and encouragement throughout my life. Dr. Matthew Cook has also been a vital part of this journey, and I appreciate his assistance in so many aspects of this project. Thanks also to Dr. Donald Hornback and the Nuclear Material Detection and Characterization group at Oak Ridge National Laboratory for allowing me to accompany them to Fort Indiantown Gap, Pennsylvania, and for the use of their detectors.

Trust in the LORD with all your heart; do not depend on your own understanding.
Seek his will in all you do, and he will show you which path to take.
Proverbs 3:5-6

Abstract

Traditional radiation detection equipment consists of various types of devices that are capable of determining the presence of radioactive sources in the vicinity of the detection unit. Use of these systems typically consists of survey and search methods that employ broad area sweeps to narrow down the location of a radioactive source. Although these methods are effective, they are typically inefficient and lack the ability to produce a directional bearing of the source relative to the measurement location. More efficient methods that provide relative direction information for detected sources would facilitate a more timely response to a potential radiological threat.

The purpose of this research was to develop and test a mobile system capable of detecting radioactive gamma-ray sources and determining the directional bearing relative to the system. This method compares the analogous intensities of a plurality of detectors placed in a specified formation dependent upon the type and size of the detector used. The formation of detectors is designed to take advantage of shadowing in the occluded array of detectors. Based on this shielding principle, a fuzzy logic algorithm was used to analyze the response of each individual detector with respect to the other three to determine the location of a source.

The algorithm was tested using MCNP models of urban environments. This helped determine the limitations of the system and its practicality in real world scenarios where distance and shielding of a source lower the probability of detection. Characterization of the ambient background radiation field was also performed in the area relative to where the system testing would take place. This allowed for

an evaluation of the system performance with the presence of real-world naturally-occurring background radiation. Source injection studies were completed to test the ability of the system and the threshold at which the system can detect radiation sources. Field tests were also performed in an area similar to that modeled in order to validate the model and verify the results of source localization.

Table of Contents

1 Introduction **1**

1.1 Problem Statement 1

1.2 Background 2

2 Fuzzy Logic **6**

2.1 Mamdani-Type Fuzzy Logic 8

2.1.1 Evaluate the Antecedent for Each Rule 8

2.1.2 Obtain Each Rule's Conclusion 9

2.1.3 Aggregate Conclusions 10

2.1.4 Defuzzification 11

2.2 Membership Functions 12

2.3 Rule Sets 14

3 Modeling of Systems **16**

3.1 System Variation 16

3.1.1 Lead Cruciform 17

3.1.2 Ideal Detector Response 19

3.1.3 Modified Detector Layout 19

3.2 Standoff Distance Variation 28

3.3 Rule Set Sensitivity Study 29

3.4 Source Elevation Sensitivity Study 34

4 System Development **37**

4.1 System Design 37

4.2 Background Radiation Studies 44

4.2.1 Background Radiation Sources 49

5 Urban Environment Modeling **57**

5.1 Parking Lot 57

5.2 Urban Source Search Testing at Fort Indiantown Gap, Pennsylvania . 63

5.2.1 Model Verification 65

6 System Characterization **72**

6.1 Receiver Operating Characteristic 72

6.2 Algorithm Localization Performance 81

6.3 k-sigma Algorithm 91

6.4 Fuzzy Logic Uncertainty 93

7 Future Work **97**

7.1 Fuzzy Rule Transitions 97

7.2 Detection Algorithm Development 97

8 Conclusions **99**

Bibliography **102**

Appendix **108**

A Elevation Angle Results **109**

B Simulated Parking Lot Directional Results **130**

Vita **138**

List of Tables

3.1 Residual Comparison for 100 keV and Varying Lead Thicknesses . . . 17

3.2 Residual Comparison for 350 keV and Varying Lead Thicknesses . . . 18

3.3 Residual Comparison for 1200 keV and Varying Lead Thicknesses . . 18

3.4 Residual Comparison for 2700 keV and Varying Lead Thicknesses . . 18

3.5 Rule Comparison for Positions 0-2 23

3.6 F1 Tally Results for a ^{137}Cs Source Placed at Distances Between 25-500 cm 31

3.7 Residual Comparison for a 360° Azimuthal Space at Different Elevation Angles Expressed in Degrees Difference from Known Angle 35

4.1 Background Gamma Sources and Associated Energies 51

6.1 Probabilities of Detection for Various Source Strengths and Distances for Simulated ^{137}Cs in Hotel 80

6.2 Localization Results with Uncertainties for Various Source Distances from Roadway 88

6.3 Probabilities of Detection for Various Source Strengths and Distances for Simulated ^{137}Cs 5m off the Roadway 89

6.4 Probabilities of Detection for Various Source Strengths and Distances for Simulated ^{137}Cs 10m off the Roadway 89

6.5 Probabilities of Detection for Various Source Strengths and Distances for Simulated ^{137}Cs 15m off the Roadway 90

6.6 Probabilities of Detection for Various Source Strengths and Distances for Simulated ^{137}Cs 20m off the Roadway 90
6.7 Minimum Source Activity Required at Various Distances for a 1 Second Detection Live Time 91

List of Figures

1.1 2x2 Detector Array Setup for Laboratory Testing 2
1.2 Detector Setup Showing Occlusion Principle 3
1.3 100 keV MCNP Response Curves for First 180° of Test Track 4
1.4 2700 keV MCNP Response Curves for First 180° of Test Track 5

2.1 Non-Fuzzy vs Fuzzy Logic Evaluation of Water Temperature 7
2.2 Fuzzification Process for Fuzzy Logic Rules 9
2.3 Creating a Fuzzy Conclusion for Each Rule 10
2.4 Aggregation of Fuzzy Logic Conclusions 11
2.5 Fuzzy Rule Centroid Deffuzification 12
2.6 Illustration Showing Possible Levels of Response Heights 13

3.1 Large NaI(Tl) Box 3D Layout 20
3.2 NaI(Tl) Box Fuzzy Inputs 20
3.3 Large NaI(Tl) Box 3D Layout with Lead Cruciform 21
3.4 NaI(Tl) Box with Lead Cruciform Fuzzy Inputs 21
3.5 NaI(Tl) Square Detector Layout 22
3.6 NaI(Tl) Square Fuzzy Inputs 22
3.7 “X” System Detector Layout 23
3.8 ”X” System Fuzzy Inputs 24
3.9 ”X” System Detector Layout with Lead Block in Center 25
3.10 X-Cross Layout with Long Lead Cruciform 25

3.11 X-Cross Layout with Long Lead Cruciform Fuzzy Results 26
3.12 X-Cross Layout with Small Lead Cruciform 27
3.13 X-Cross Layout with Small Lead Cruciform Fuzzy Results 27
3.14 Standoff Distance Setup for First 90° 28
3.15 Comparison of Modeled Results to $1/r^2$ for First 90° 29
3.16 Distance Portraying Field-of-View for Various Distances 30
3.17 Illustration of Surfaces Used for F1 Tally Simulations for Near-Field/Far-Field Comparison 31
3.18 Response Curve Comparison for 5, 10, 15, and 20 Meters 32
3.19 Response Curve Comparison of 1m and 15m for First 90° 33
3.20 Comparison of Directional Bearing Results Using 1m and 15m Rule Sets 34

4.1 Four-Quadrant Detector Setup with Stainless Trough 38
4.2 Base and Pedestal Setup for Flatbed Detector System 38
4.3 Mobile System Prototype Setup 39
4.4 Screenshot of GUI Showing Multiple Channel Histogram Plotting . . 41
4.5 Screenshot of GUI Showing User Feedback Directional Arrow Controlled by Fuzzy Results 42
4.6 System Setup on Mobile Cart 43
4.7 X-Cross Setup on Mobile Cart 44
4.8 Naturally Occurring ^{40}K Concentration Across the United States as mapped by the United States Geological Survey (USGS) [17] 45
4.9 Naturally Occurring ^{232}Th Concentration Across the United States as mapped by the United States Geological Survey (USGS) [17] 45
4.10 Naturally Occurring ^{238}U Concentration Across the United States as mapped by the United States Geological Survey (USGS) [17] 46
4.11 Decision Level L_C Assuming a Normal Distribution 48
4.12 Detection Limit L_D and Associated False Positives/False Negatives . 49
4.13 Detector Setup for Elevation Angle Measurements 50

4.14 Background Measurement Points at Fort Indiantown Gap, Pennsylvania 50
4.15 Average Gross Count Rate from Background at FIG Measurements Points 51
4.16 Elevation Angle Results for Measurement Point 16 at Fort Indiantown Gap, Pennsylvania 52
4.17 Elevation Angle Results for Measurement Point 9 at Fort Indiantown Gap, Pennsylvania 53
4.18 Elevation Angle Results for Measurement Point 8 at Fort Indiantown Gap, Pennsylvania 54
4.19 Average Gross Count Comparison for Different Times of the Day (Error Bars Not Visible) 55

5.1 3D Model of Vehicle Used in MCNP 58
5.2 MCNP Model of Parking Lot 58
5.3 Possible Locations of Source (S) and Detector Car (C) 59
5.4 Algorithm Response with Source at Location S0 60
5.5 Counts per Second Response with Source at Location S0 61
5.6 MCNP Mesh Tally of Source at S0 and Detector Car at C0 62
5.7 Line-of-Sight Comparison for Various Distances 63
5.8 Satellite Image of Fort Indiantown Gap, Pennsylvania 64
5.9 Comparison of Actual and Model of Hotel at Fort Indiantown Gap, Pennsylvania 65
5.10 Sum of 4 - EJ200 Detector Gross Counts at Measurement Points Along Hotel Road 66
5.11 Comparison of Measured and Modeled DPHS from EJ200 Detectors at Centerline of Hotel 67
5.12 Comparison of EJ200 Sum of Gross Counts per Second for Measurement Points Along Roadway 67

5.13 Sum of 4 - NaI(Tl) Detector Gross Counts at Measurement Points Along Hotel Road 68
5.14 Comparison of of Measured and Modeled DPHS from NaI(Tl) Detectors at Centerline of Hotel 69
5.15 Comparison of the Sum of Gross Counts from NaI(Tl) Modeled and Measured Roadway Measurements 69
5.16 Comparison of the Counts Under 662 keV Peak from NaI(Tl) Modeled and Measured Roadway Measurements 70

6.1 Probability Distributions for Background (N_B) and Total Counts (N_T) 73
6.2 Probabilities of Observing Counts Greater than N 73
6.3 ROC Curve for Probability Distributions 74
6.4 ROC Curve from Centerline Hotel Measurement with X-Cross System (All Data Points Are near Either 1 or 0 and Lie on Axes) 75
6.5 Histograms of Background and Total Counts 75
6.6 Integrals of Probabilities of Observing Counts Greater than "N" . . . 76
6.7 Histograms of Background and Total Counts from Currie Equation Results 77
6.8 Integrals of Probabilities of Observing Counts Greater than "N" with Currie Equation Results (200 μCi ^{137}Cs) 77
6.9 ROC Curve from Currie Equation Estimation 78
6.10 ROC Curves for Various Activities of ^{137}Cs at Centerline of Simulated Hotel 79
6.11 Radial Distances from Hotel Centerline in Meters 80
6.12 Depiction of Ray Tracing Using Directional Bearings 83
6.13 Localization Determination of a 36 mCi ^{137}Cs Source Laid over a Satellite Image 84
6.14 Localization Determination of a Simulated 1 mCi ^{137}Cs with Fine Bins 85
6.15 Localization Determination of a Simulated 1 mCi ^{137}Cs with Coarse Bins 86

6.16 The average and standard deviation of critical parameters 87
6.17 Probability of Detection and Probability of False Alarm vs k-sigma Values at Simulated Hotel Centerline 92
6.18 Probability of Detection vs Source Activity for Different k-sigma Values at Simulated Hotel Centerline 93
6.19 Fuzzy Number Result and Uncertainty for Various Positions and Energies 95

Chapter 1

Introduction

1.1 Problem Statement

Current radiation detection approaches include a variety of methods and equipment to detect and quantify the presence of a radioactive source. These techniques utilize a variety of equipment including gas-filled, scintillator, and semiconductor detectors in both portal monitors [1, 2] and mobile detection systems [3, 4]. Each one of these detectors has unique benefits as well as shortcomings. Most of these, however, share the inability to determine a directional bearing of the radiation source being detected. The purpose of this research was to develop a novel system capable of detecting and resolving a directional bearing of the radioactive source in a real-world environment. This capability would provide for faster localization of an illicit radiation source in urban environments, where the dense surroundings make detection more difficult. This includes having a system that responded in real-time rather than post-processing results. As with many radiation detection techniques, various scenarios were modeled using MCNP6. The models were designed to simulate realistic environments to determine the system's response to shielding and varying distances from the source. After modeling the system and establishing benchmarks for comparison, field trials were performed to verify the response of the system and algorithm. The results of

these models and tests allowed for a quantification and characterization of the system to be performed.

1.2 Background

The development of this detection system is a continuation of the work performed by Michael J. Willis for his Master of Science in Nuclear Engineering [5]. The previous research included the creation of the fuzzy logic algorithm and validation studies in laboratory-scale testing. The principle behind the algorithm is that the system receives the counts from each detector as its inputs and applies a set of fuzzy logic rules to the input set. The output of the algorithm produces a number relative to a position number around a circle which is converted to 0-360°. During the laboratory testing, an 1:48 scale model train was used on a circular track with a radius of 18 inches. The detectors tested were four 2"x2"x4" NaI(Tl) detectors placed in aluminum housings and coupled to photomultiplier tubes. A 2x2 quadrature array, as shown in Figure 1.1, was created by placing the detectors next to each other; this array was placed in the center of the track.

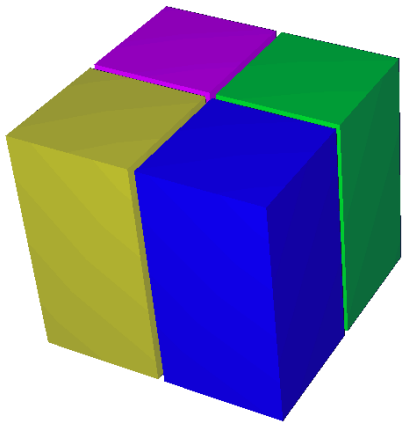


Figure 1.1: 2x2 Detector Array Setup for Laboratory Testing

A variety of low activity button sources, including ^{137}Cs and ^{60}Co, were placed on the model train to evaluate the system. As the train advanced around the

track, the four stationary detectors' responses were compared to each other for each measurement point. The arrangement of detectors utilized an occlusion principle to shield the detectors further away from the source as shown in Figure 1.2.

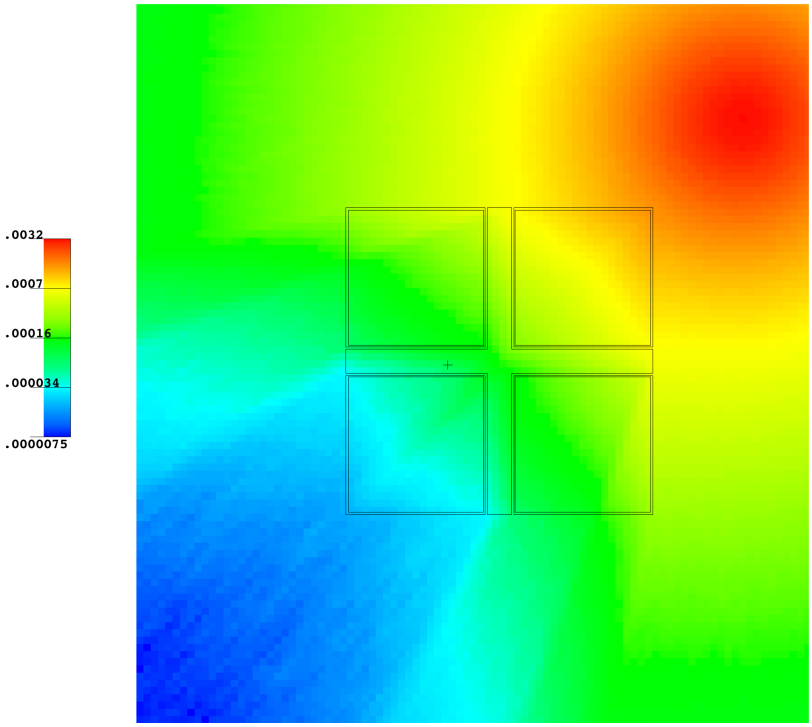


Figure 1.2: Detector Setup Showing Occlusion Principle

Each location around the detectors had a distinct comparative response that could be observed using results from MCNP simulations for each location along the 360° azimuth plane. MCNP simulations were completed with various energies from 100 keV to 2700 keV to verify the validity of the algorithm for all photon energies of concern. The positions along the track were evaluated every 22.5° and labeled Points 0-8, with Point 0 being 0° and Point 8 corresponding to 180°. An example response from the system for the first 180° is shown in Figure 1.3.

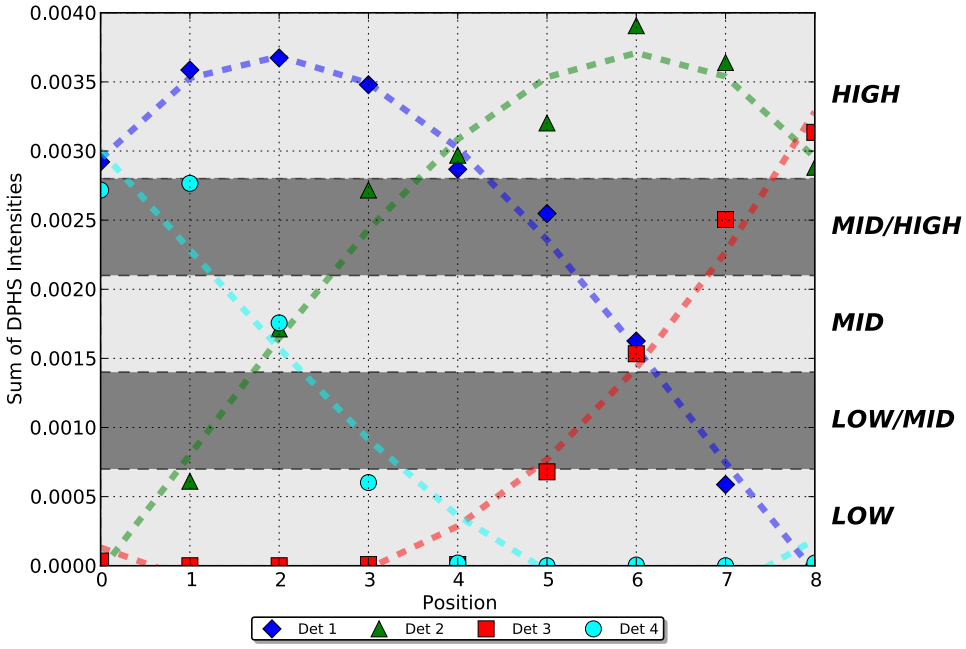


Figure 1.3: 100 keV MCNP Response Curves for First 180° of Test Track

The ranking of the response values shown in Figure 1.3 were "LOW" through "HIGH" and were assigned by visual estimation of where each detector response was located. The general shape of the response curves remained the same for energies up to 2700 keV, but the separation of the individual detector responses at each location became less, as shown in Figure 1.4.

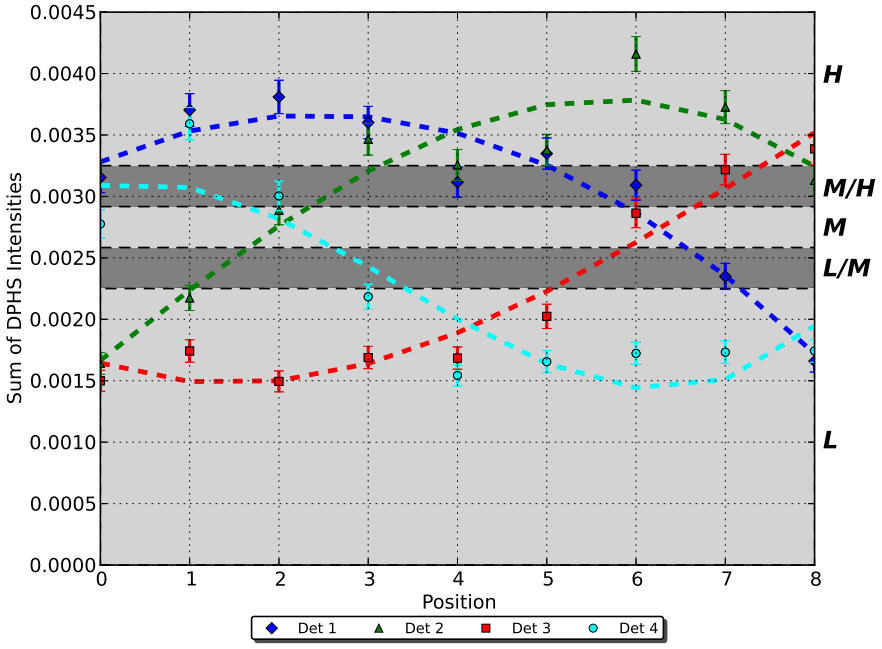


Figure 1.4: 2700 keV MCNP Response Curves for First 180° of Test Track

The modeling and testing results proved that the algorithm was capable of working with all ranges of photon energies. However, these tests revealed that the higher energy photons were less attenuated by the closer detectors, indicating that a high density cruciform should be used between the detectors for increased occlusion. Results from the laboratory testing showed the system to be capable of determining the directional bearing of a ^{137}Cs on the azimuthal plane to within 3.8-13.5° of the known angle. Although this setup and algorithm testing yielded fairly accurate results for the directional bearing, more extensive studies needed to be performed to determine how well the system would perform in real-world scenarios. These studies were mainly focused on developing a field-scale version of the system and characterizing its performance in a variety of real-world scenarios.

Chapter 2

Fuzzy Logic

The term *fuzzy logic* stems from "Fuzzy Sets", first introduced in 1965 by Lotfi A. Zadeh of the University of California at Berkeley [6]. Zadeh had observed that computer logic was unable to process subjective ideas. Therefore, he created fuzzy sets to determine the distinctions among data with ambiguity, similar to human reasoning. These fuzzy sets were classes having a variety of grades of memberships. Zadeh used the example of animal classes to portray why fuzzy sets might be applicable. An animal class would include dogs, cats, birds, etc. as its members, but would exclude objects such as rocks and plants. Equivocal objects, such as starfish and algae, would have an ambiguous status with respect to the class of animals. These objects could fall into certain "classes", but only if they were on the continuum of membership requirements for each class [6]. The use of fuzzy sets (or fuzzy logic) allows classes or sets to be managed by membership functions with "unsharp boundaries" [7].

Problem solving using fuzzy logic is similar to other methods of problem solving in that it receives an input, evaluates the input against pre-assigned rules, and creates an output that fits the data accordingly. Typical analytical methods have sharp boundaries of whether an input lies within a certain class or not, and therefore are limited on the output possibilities. For example, if temperature is used to determine whether water is hot or cold, a non-fuzzy system may have 70°F as a sharp boundary

between the two. If the water was 69.9 °F, the system may determine the water to be cold. A fuzzy system with unsharp boundaries could determine the 69.9 °F to be "nearly hot" rather than cold. A example of this type of logic is shown in Figure 2.1

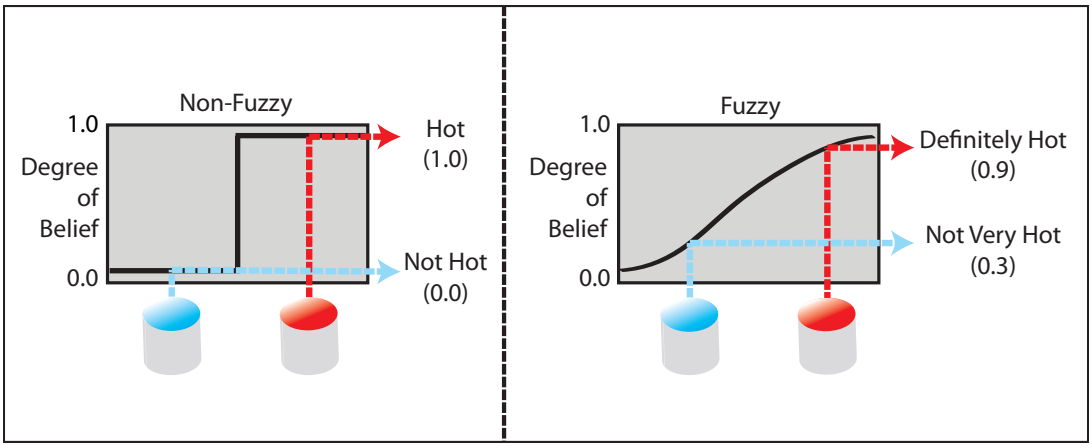


Figure 2.1: Non-Fuzzy vs Fuzzy Logic Evaluation of Water Temperature

To utilize the unsharp boundary capabilities, a fuzzy system against which inputs can be tested must be created. The first step in a fuzzy system is to create rules for the system to follow. Depending on how defined one wants the system to be, the number of rules varies. The more rules the system has to compare against the input, the more exact the output will be. To create these rules, a fuzzy system uses what is known as IF-THEN rules [8]. By creating simple *IF* policies that produce *THEN* results, a set of simple rules can be created that have definitive answers for set policies. An example set of rules can easily be demonstrated in Equations 2.1 and 2.2 [9].

$$IF\ X_1\ is\ small\ and\ X_2\ is\ small,\ THEN\ Y\ is\ small \tag{2.1}$$

$$IF\ X_1\ is\ large\ or\ X_2\ is\ small,\ THEN\ Y\ is\ large \tag{2.2}$$

Using a set of rules similar to the format above, a variable numeric value is assigned to the words *small* and *large*. If a scale of zero for small to one for large is used as possible values, one can achieve a numeric results from the inputs. Sometimes, an input may be neither exactly zero nor one. In cases like this, fuzzy systems can use the input data to achieve results that are similar to those expected with definitive inputs of zero or one.

2.1 Mamdani-Type Fuzzy Logic

Typically, fuzzy sets have multiple rules that are combined and compared to create a complete set for evaluating a system's inputs. To evaluate multiple results from different rules, a system must have a logical methodology in estimating a combined result. A common type of fuzzy system that is capable of doing this is one that uses the Mamdani-type fuzzy logic approach. In this type of method, the following steps are used.

2.1.1 Evaluate the Antecedent for Each Rule

This is the first step in any fuzzy logic system. It is during this step that the input values become *fuzzy*. Based off a scale chosen by the operator (e.g. 1-10), the value of each rule is input as a number on the x-axis. Using similar rules previously discussed for example, small would be denoted as 0 and large as 10. A benefit to this system is if there were values between small and large that were added to different rules, they could take on numerical values such as five for medium. Each rule is then evaluated and is assigned a membership function on the y-axis. Rules can be created with either an *AND* or an *OR* operation. If the *AND* operation is used within a rule, all input values are examined and the minimum input membership function value is used to define the output membership function. Whereas, if the *OR* operation is

used, the maximum input value is used to determine the output value. An example fuzzy process can be seen in Figure 2.2.

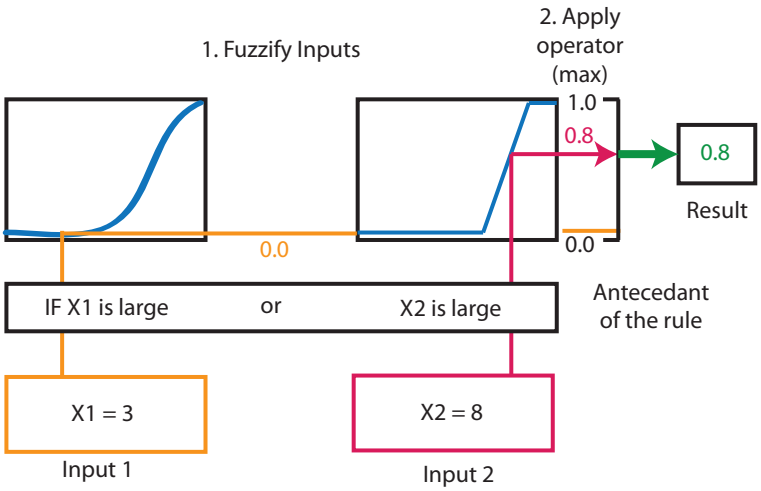


Figure 2.2: Fuzzification Process for Fuzzy Logic Rules

2.1.2 Obtain Each Rule's Conclusion

After the fuzzification of each rule, the next step is to use the resulting membership function to create a new fuzzy set. To accomplish this, the numerical results from a rule are used, and a result is created that can be used as a fuzzy operator. Using the example in the first rule, the two inputs were small and large with the corresponding values of 3 and 8, respectively. Since the rule used an *OR* operator, the maximum of the two functions (8) was used and the output result was 0.8. If this number is applied to a Y-result function, a result for Y can be resolved. This is shown below in Figure 2.3.

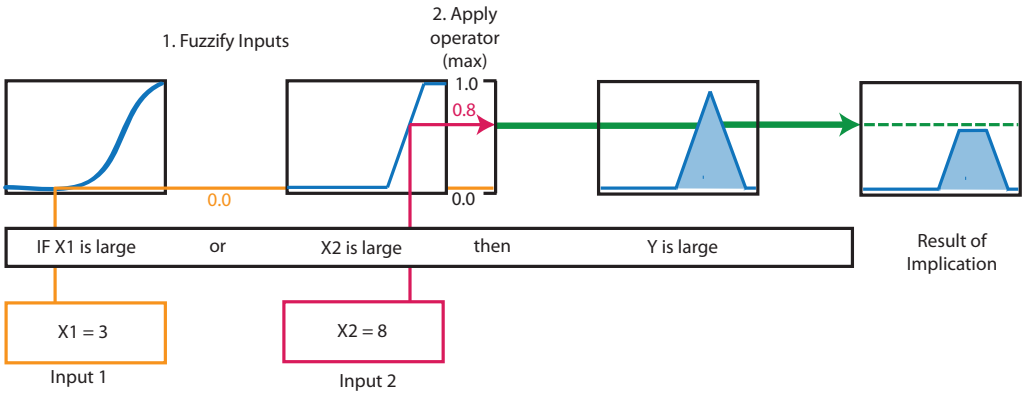


Figure 2.3: Creating a Fuzzy Conclusion for Each Rule

2.1.3 Aggregate Conclusions

The next step in the fuzzy process is to aggregate the conclusions resolved from each rule. During this step, the result of each rule is combined to form one single fuzzy set. To accomplish the summation of rule results, a variety of fuzzy aggregation operators can be used. Some examples include mean operators, generalized mean, and ordered weighted aggregation [10]. For this example, a maximum aggregation method is utilized. This method takes the maximum possible result from each rule and combines them to form a single result. This process is shown in Figure 2.4.

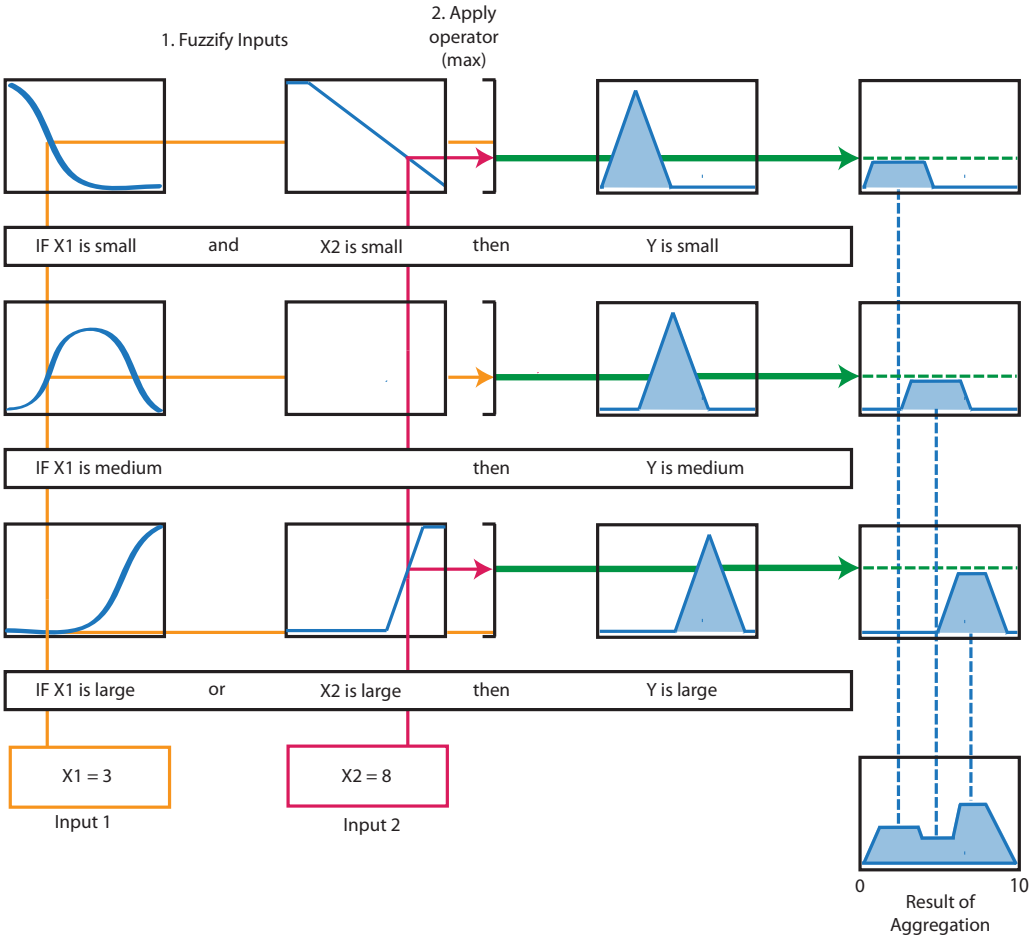


Figure 2.4: Aggregation of Fuzzy Logic Conclusions

2.1.4 Defuzzification

The final step in the fuzzy logic process is the defuzzification of the data and results. Simply put, this process turns a fuzzy output into a numerical output that can be interpreted more easily. There are many different defuzzification procedures such as mean of maxima (MOM) and the center of gravity (COG) methods that are utilized in practice [11]. One of the most common defuzzification methods is centroid defuzzification, which is utilized here. This method is rather simplistic in that it takes the centroid of each fuzzy set formed from individual rules and combines them to form a single result. This process is shown in Figure 2.5.

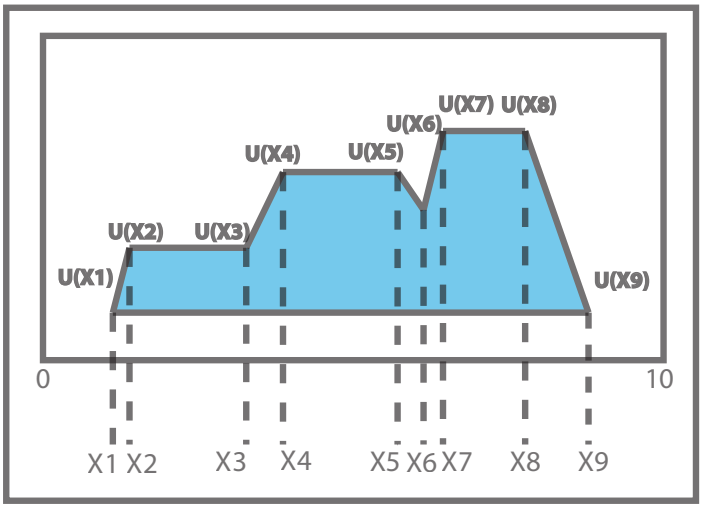


Figure 2.5: Fuzzy Rule Centroid Deffuzification

Using each X_i location and the corresponding U(X_i) values, the following equation is used to form a single numerical solution.

$$Defuzzification\ Result\ = \frac{\sum_{i=1}^{9} X_i * U(X_i)}{\sum_{i=1}^{9} U(X_i)} = 6.67\ (for\ this\ example) \qquad (2.3)$$

From the Equation 2.3 above, the results show that Y would equal 6.67. Using the scale from 0 (small) to 10 (large), one can conclude that from the rules as well as the input X_1 and X_2 values the resulting Y would be slightly large.

2.2 Membership Functions

The first step in the fuzzy logic process was to evaluate the antecedent for each rule. In this system, this was accomplished by examining the gross counts under the radiation energy peak of interest relative to each other for each position. To simplify the system, five choices were initially used for possible levels of intensity. They were high, mid/high, mid, low/mid, and low and are shown in Figure 2.6.

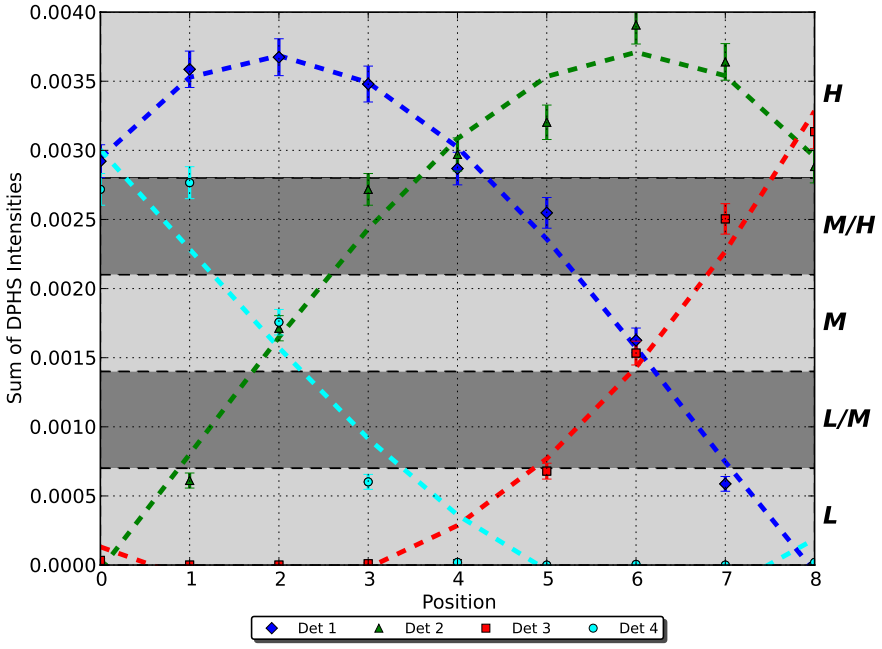


Figure 2.6: Illustration Showing Possible Levels of Response Heights

With each position having a distinct set of response heights, the next step was to obtain the conclusion for each rule. For example, the first position had detector 1 and 4 as high and detector 2 and 3 as low. With this being the only position that had this configuration, the conclusion was that the source location was position 1. In reality, the intensities may not be exactly as entered into the system. For instance, at the initial position, one of the three detectors may produce an erred result not expected for that position. Instances like this are controlled by the third step of this fuzzy logic approach, aggregation of conclusions. This step combined the outputs for each rule into a single fuzzy set using a fuzzy aggregation operator. For this step, the aggregation operator used is "maximum." The final step in this process was defuzzification. During this step, the system turns the fuzzy set's output into a numerical value. Centroid deffuzification returned the center of the areas under the resulting fuzzy sets and combined them to return one numerical result or position.

2.3 Rule Sets

To produce an accurate result of the source position, each detector needed to have an input to the fuzzy system. Using the inputs for each quadrature, they can be compared to the rule set in the fuzzy logic system. These rules are set up in a format similar to what is shown in Equation 2.4.

$$\begin{gathered} If\ Quad\ 1\ is\ high,\ And\ Quad\ 2\ is\ low, \\ And\ Quad\ 3\ is\ low,\ And\ Quad\ 4\ is\ high, \\ Then\ the\ result\ is\ Position\ 1 \end{gathered} \tag{2.4}$$

A benefit of this system is that each position was distinct from the others as to how the detectors responded according to each other. In other words, if all *AND* statements were satisfied, the results were capable of producing one distinct position along the semicircular axis. Due to this, each position had to have its own set of rules, where there was at least one rule per position. With this method, as many rules as desired could be created. Typically, the more rules there are that can be evaluated, the more precise the results. In the case of this system, more rules correspond to a more accurate determination of the source position. A problem with the system could occur if the rules contradict themselves, but not complicating the rules or having multiple rules for each position prevented this from occurring. As the rules for each quadrant are manipulated based off the relative intensity of each quadrant relative to the other three, the resulting position can be determined. This system was set up so that the intensities correspond to the following values on a scale of 0-100.

$$High : 100$$

$$Mid/High : 75$$

$$Mid : 50$$

$$Low/Mid : 25$$

$$Low : 0$$

In order to accommodate this input scale, the measured counts from each of the detector needed to be normalized for all of the detectors' responses to lie within this scale. The normalization process made the largest value equal to 100 and the lowest equal to 0. The remaining values were determined using Equation 2.5

$$X_{i,\ 0\ to\ 100} = \frac{X_i - X_{Min}}{X_{Max} - X_{Min}} \tag{2.5}$$

An advantage of this system is that it can take into account the fact that real world results are not always ideal. This means that if one detector resulted in an intensity that looked more like 85 (between High and Mid/High), the system would use the rules and take that into account to give an accurate result even though the discrepancy exists.

Chapter 3

Modeling of Systems

3.1 System Variation

As discussed in the previous chapter, a benefit to this system is that the algorithm only requires individual inputs from a plurality of detectors, regardless of the layout of the system and produces a singular output representing a relative bearing. As long as there is some sort of occlusion between the detectors, rule sets can be created for each layout using results from MCNP6 model results. The original system layout involved symmetrical 2"x2"x4" NaI(Tl) detectors that could be placed together to form a larger square with each detector placed in a "quadrant." The next iteration of the system involved similarly-shaped 5"x5"x6" EJ200 plastic scintillator detectors placed in the same configuration as the smaller NaI(Tl). A benefit to to using plastic scintillators in this application was the ability to increase the size of the detector (and therefore the geometric efficiency) at a relatively lower cost. A drawback to organic scintillators, however, is that they are made of materials of low atomic number (low Z) and have a lower density. This material also has a lower photon absorption coefficient than NaI(Tl) due to its proportionality to Z. These properties, combined with a lower energy resolution cause the fraction of photons that deposit their full energy to be lower, making Compton scattering the main interaction within the scintillator

[12]. Although this forgoes the ability for isotopic identification due to poor energy resolution, the larger detector size affords an overall greater sensitivity to detecting the presence of radioactive sources.

3.1.1 Lead Cruciform

From the initial algorithm development work, it became evident that higher energy gamma rays caused more scattering into the adjacent detectors, causing the results to be less accurate. This occurred in aluminum-cased NaI(Tl) detectors with a density of 3.67 $^{g}/_{cm^3}$. This phenomenon intensified when the EJ200 detectors with a density of 1.023 $^{g}/_{cm^3}$ were used. The less dense material did not occlude the other detectors as well for the entire energy range of concern. To overcome this, a model was created that added a proposed shielding material between each of the detectors. This would create additional occlusion of the detectors further from the source. Lead, because of its high density and shielding capabilities, was used to create a cruciform-shaped shield between the detectors. Various thicknesses of lead were added to see if there was an optimal thickness that could prevent Compton-scattered photons from higher-energy photons from crossing into the detectors furthest from the source. These thicknesses ranged from 1mm to 2cm between each detector with particle energies ranging from 100 keV to 2700 keV. The residuals from the known bearing and the calculated bearing results from these models are shown in Tables 3.1 to 3.4.

Table 3.1: Residual Comparison for 100 keV and Varying Lead Thicknesses

	100 keV								
	Residual of Calculated and Known Bearing (Degree)								
Bare	1.13	2.48	0.22	4.05	0.00	3.83	0.00	0.22	0.90
1 mm Cruciform	1.13	2.48	0.22	4.05	0.00	3.83	0.00	0.22	0.90
5 mm Cruciform	1.13	0.00	0.00	0.45	0.00	0.90	0.00	0.22	0.90
1 cm Cruciform	1.13	0.00	0.00	0.67	0.00	0.68	0.00	0.00	0.90
2 cm Cruciform	1.13	0.45	0.22	0.45	0.00	2.03	0.22	0.00	0.90
Known Bearing	0.00	22.50	45.00	67.50	90.00	112.50	135.00	157.50	180.00

Table 3.2: Residual Comparison for 350 keV and Varying Lead Thicknesses

	350 keV								
	Residual of Calculated and Known Bearing (Degree)								
Bare	1.58	2.70	0.00	3.15	0.22	2.93	0.68	0.45	1.13
1 mm Cruciform	1.13	1.35	0.00	2.48	0.00	2.03	0.45	0.00	0.90
5 mm Cruciform	1.35	0.00	0.00	0.67	0.00	1.35	0.00	0.00	0.90
1 cm Cruciform	1.13	0.00	0.00	0.90	0.00	1.13	0.22	0.00	0.90
2 cm Cruciform	1.13	0.00	0.00	0.67	0.00	0.90	0.22	0.00	1.13
Known Bearing	0.00	22.50	45.00	67.50	90.00	112.50	135.00	157.50	180.00

Table 3.3: Residual Comparison for 1200 keV and Varying Lead Thicknesses

	1200 keV								
	Residual of Calculated and Known Bearing (Degree)								
Bare	2.70	9.90	0.68	8.78	0.00	6.07	0.45	0.00	1.13
1 mm Cruciform	4.28	1.58	0.00	1.13	1.13	3.83	0.45	0.90	1.13
5 mm Cruciform	1.58	0.68	0.00	1.80	0.00	1.58	0.45	0.45	1.13
1 cm Cruciform	2.03	0.45	0.22	2.03	0.00	2.03	0.22	0.45	1.13
2 cm Cruciform	1.58	0.23	0.00	1.58	0.00	1.80	0.00	0.00	0.90
Known Bearing	0.00	22.50	45.00	67.50	90.00	112.50	135.00	157.50	180.00

Table 3.4: Residual Comparison for 2700 keV and Varying Lead Thicknesses

	2700 keV								
	Residual of Calculated and Known Bearing (Degree)								
Bare	17.78	10.80	0.00	11.70	1.80	22.50	0.68	0.68	2.03
1 mm Cruciform	2.25	2.05	0.01	3.40	0.00	3.97	0.26	0.02	1.19
5 mm Cruciform	4.77	0.30	0.23	3.69	0.05	2.59	0.60	0.12	1.58
1 cm Cruciform	5.11	0.75	0.29	1.77	0.00	2.53	0.69	0.45	1.05
2 cm Cruciform	2.79	0.65	0.23	1.52	0.07	2.24	0.35	0.37	1.05
Known Bearing	0.00	22.50	45.00	67.50	90.00	112.50	135.00	157.50	180.00

From Tables 3.1 to 3.4, one can see that the accuracy of the results increases as the thickness of the lead cruciform is increased to 2 cm. The largest gain in accuracy for the inferred source position occurs with the addition of a 5 mm cruciform, however a 2 cm cruciform provides the most precise results (within 5% of the known position).

3.1.2 Ideal Detector Response

When designing the layout for a fuzzy logic system, there were a few criteria the detector responses needed to meet. The ideal scenario would create a 360° rule set that would include three criteria. The first component of an ideal rule set would involve having good separation between detector responses for each channel at every position. By having large separations between all channels, the normalization of the inputs do not cluster or obscure the normalization of the inputs between 0 and 100. The next specification of a good rule set is monotonicity in the detector response between the membership function's minimum and maximum. This standard would require the response curve of each channel to move only up or down with increasing position until it hits the maximum or minimum value. Ideally, there would be no plateaus along the response curve, as this would cause multiple rules to have similar input values between the minimum and maximum. The final criteria would be that the rule set would be symmetrical every 90°. This allows a continuous transit over the response intensity as a function of position for each of the inputs.

3.1.3 Modified Detector Layout

With the idea that the system would be a mobile, vehicle-mounted system, one would ideally want larger detectors with a correspondingly higher geometric efficiency to increase the effective system standoff detection distance. The next iteration of the detection system involved the use of 2"x4"x16" NaI(Tl) detectors. Although these detectors provided a much larger surface area for detection, the drawback of these detectors was that they were not symmetric in shape and therefore could not be used in the previous four-quadrant layout. Various layouts were modeled using these detectors and the results of the models were plotted to see if a useful fuzzy rule set could be created. The first layout was to place the detectors end-to-end in a "box" formation and shown in Figure 3.1.

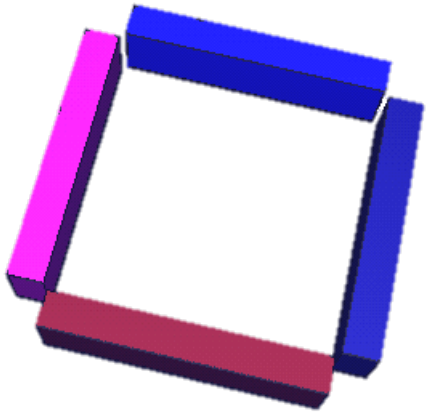


Figure 3.1: Large NaI(Tl) Box 3D Layout

The resulting fuzzy membership function input for each detector at the various positions were plotted and are shown in Figure 3.2.

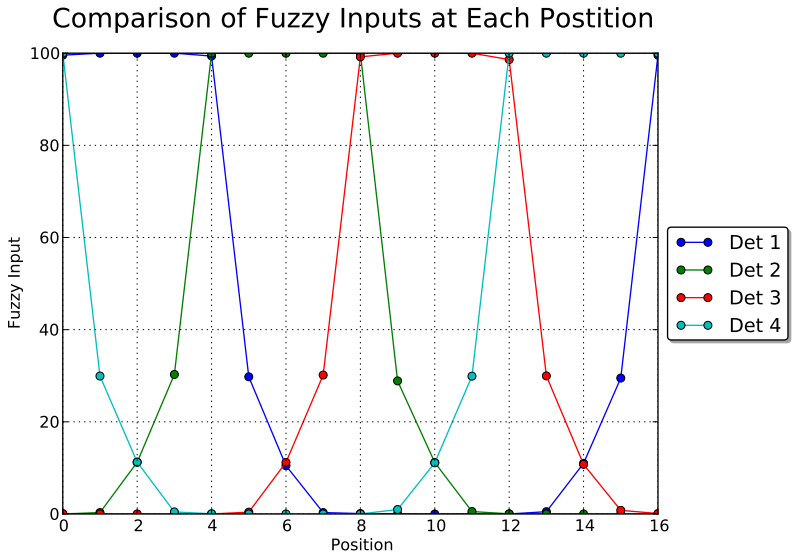


Figure 3.2: NaI(Tl) Box Fuzzy Inputs

From Figure 3.2, it is evident that there is not a large separation between the resulting values when comparing the detector results at each location. Although the results seem symmetrical for the 360°, the clustering of resulting detector inputs causes a rule set to produce inaccurate results at many of the locations. Ideally, there would be a symmetrical system response over the angular range and there would be

a separation of the values within each of the four detectors. A lead cruciform was added between the detectors to try and promote further occlusion and achieve better results. The layout of this design and results are shown in Figures 3.3 and 3.4.

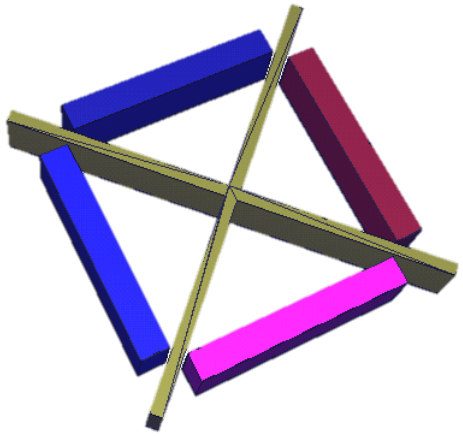


Figure 3.3: Large NaI(Tl) Box 3D Layout with Lead Cruciform

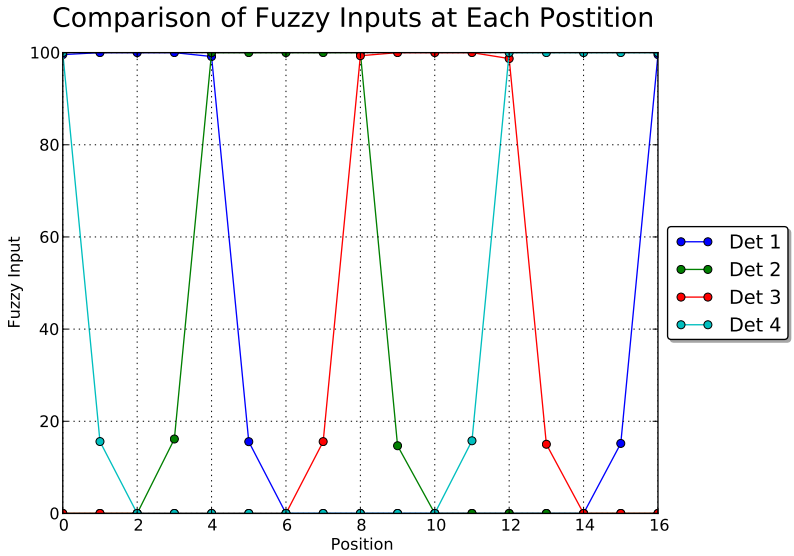


Figure 3.4: NaI(Tl) Box with Lead Cruciform Fuzzy Inputs

The addition of the lead cruciform to this detector configuration added unnecessary occlusion to the system and caused the fuzzy input results to be more clustered than without the lead cruciform. The configuration with the lead cruciform caused

there to only be one input to have a value besides the limits of 0 or 100, compared to the configuration without lead having two input parameters not equal to the limits. With only one input value being varied, the system's boundaries become more sharp and therefore cause the system performance to be poorer.

The next design modeled was also a box, but placed the detectors' sides end to end. This layout and fuzzy results are shown in Figures 3.5 and 3.6.

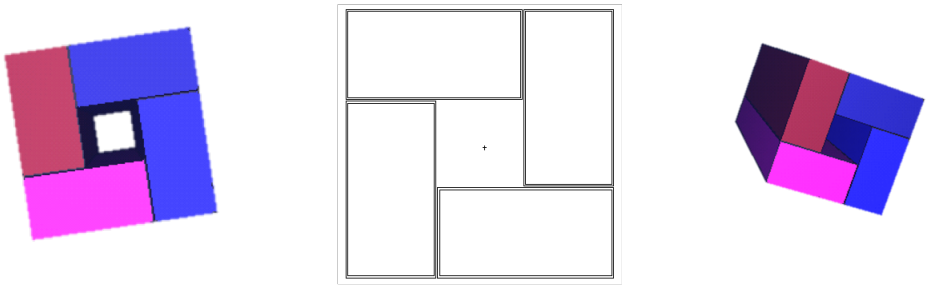


Figure 3.5: NaI(Tl) Square Detector Layout

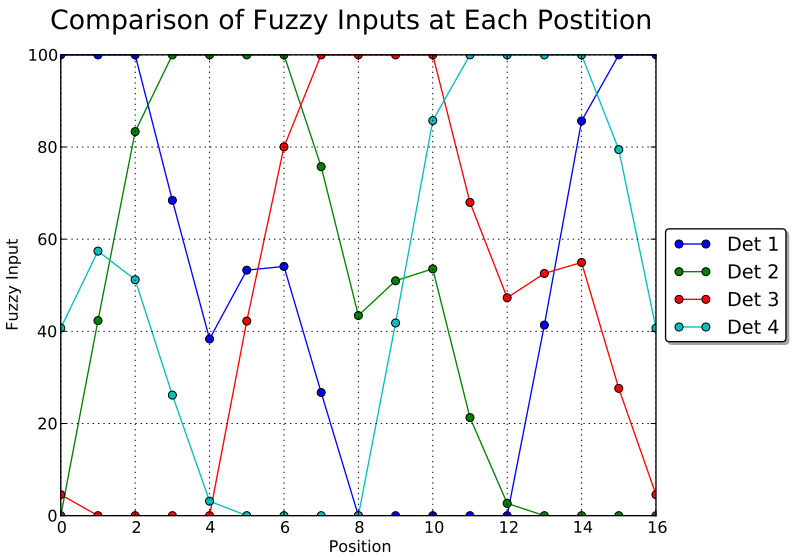


Figure 3.6: NaI(Tl) Square Fuzzy Inputs

The results shown in Figure 3.6 provide a larger separation of the detectors' fuzzy input values at each location, but this layout produces a few erroneous results within the 360°. The problem occurs at the corners of the box (i.e. Positions 0-2, 4-6, 8-10,

Table 3.5: Rule Comparison for Positions 0-2

Position	Det 1	Det 2	Det 3	Det 4
0	*High*	*Low*	*Low*	*Med*
1	*High*	*Med*	*Low*	*Med*
2	*High*	*Med/ High*	*Low*	*Med*

and 12-14) where the response curve is not monotonic. The rules at these corner positions have only one input that varies for each of the three positions around the four corners, as illustrated in Table 3.5.

The problem with this type of rule set is that it is dependent upon only one input changing between the different positions. Ideally each rule would be dependent upon multiple variables and be distinctly different for each position. Although the separation is good through most of the 360°, this layout proved not much better than the previous box layout due to the positions around each corner.

The next design placed the detectors in an "X" format with the ends of each detector meeting at the center origin. This layout and fuzzy results are shown in Figures 3.7 and 3.8.

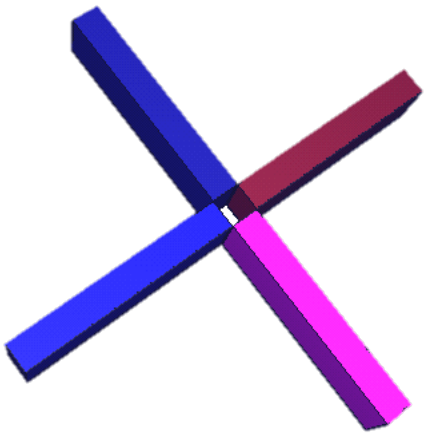


Figure 3.7: "X" System Detector Layout

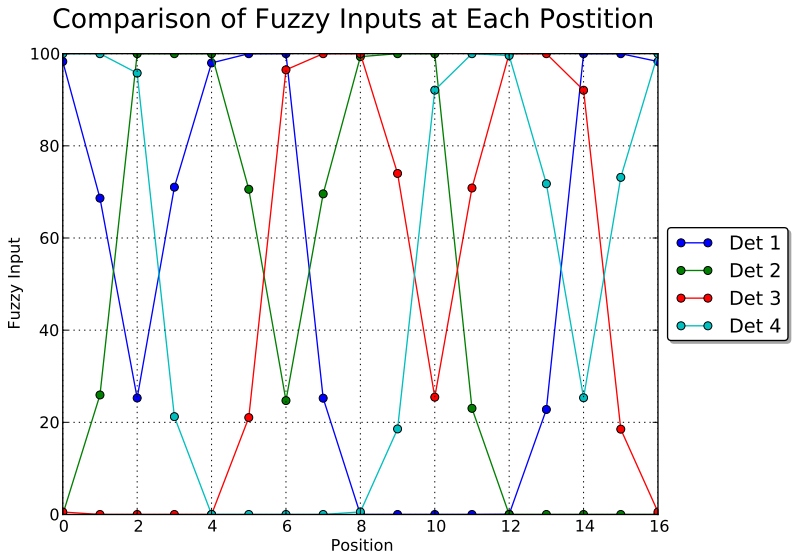


Figure 3.8: "X" System Fuzzy Inputs

This layout produced results similar to the original 4-quadrant layout with separation at each of the positions around the 360°. This layout also allowed for a rule set creation that had most rules being dependent upon multiple variables and different for each position. Utilizing the same principle addressed with the original system, lead was added within the model to promote further occlusion between the detectors. As addressed before, this addition would be beneficial for higher energy photons interacting with the system. The first variation of the X format was to add a small square of lead in the center of where all detectors touched, as shown in Figure 3.9.

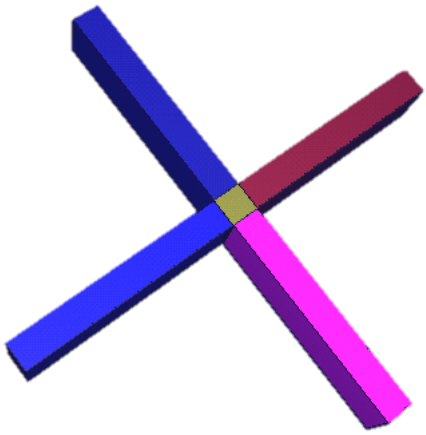


Figure 3.9: "X" System Detector Layout with Lead Block in Center

This configuration did not provide any change in the fuzzy inputs from the bare configuration as the lead only occluded the detectors lying crosswise. The next configuration had a lead cruciform placed between the detectors that extended the same length of the detectors in both the X and Y direction. This layout was called the "X-Cross" layout and results are shown in Figures 3.10 and 3.11.

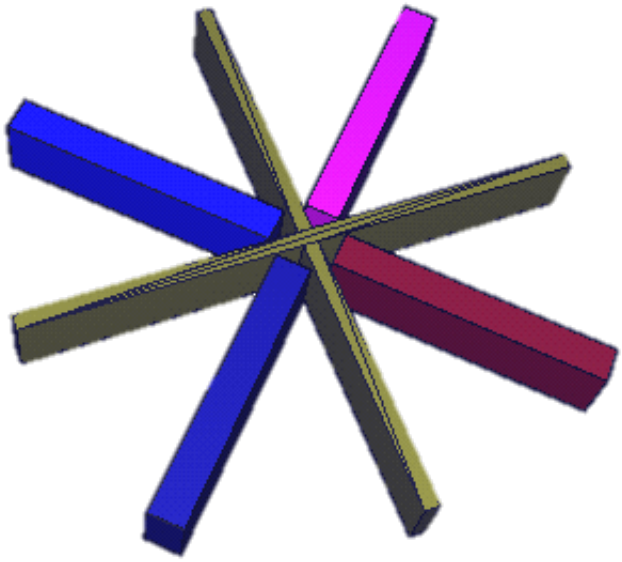


Figure 3.10: X-Cross Layout with Long Lead Cruciform

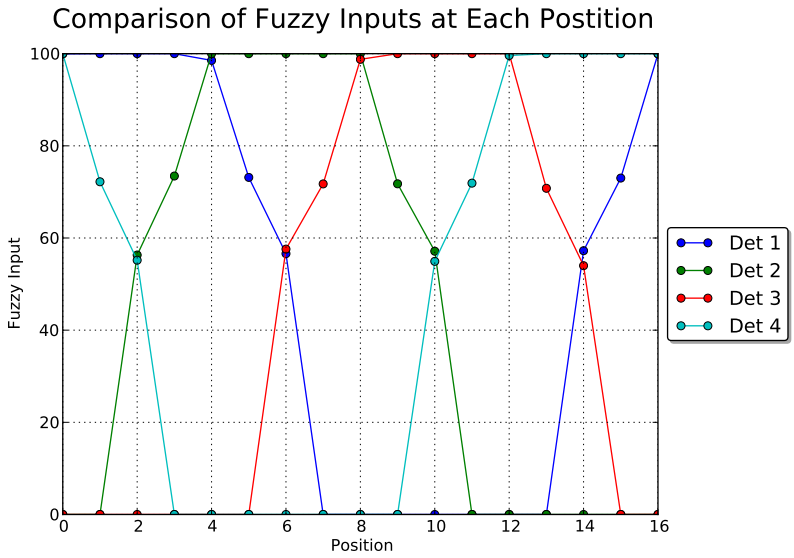


Figure 3.11: X-Cross Layout with Long Lead Cruciform Fuzzy Results

From Figure 3.11, it is evident that too much occlusion with lead can cause the normalized input values to change drastically. This is undesirable in that if the input value lies within the extreme variation area, there will be a large amount of uncertainty in the output from the fuzzy system. To maintain some occlusion for higher energy particles, the lead was shortened to half the length of the detectors and the simulation was rerun. This layout and results are shown in Figures 3.12 and 3.13.

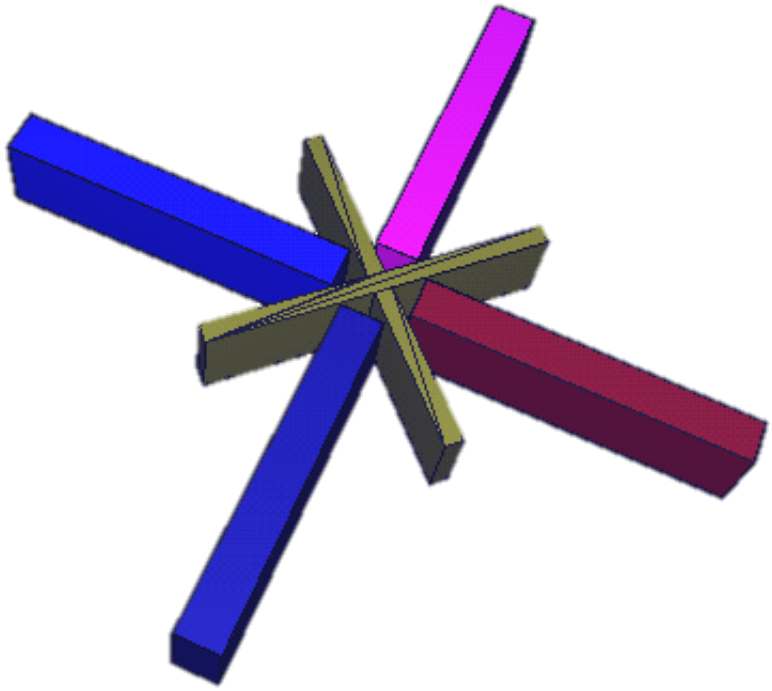


Figure 3.12: X-Cross Layout with Small Lead Cruciform

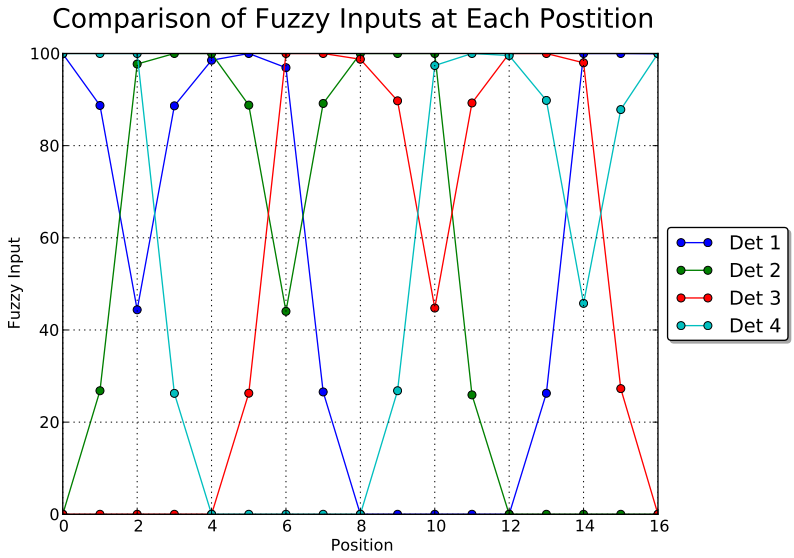


Figure 3.13: X-Cross Layout with Small Lead Cruciform Fuzzy Results

Although this configuration also has some drastic changes in input values between position, there was a simultaneous change in another detector that allowed for more accurate rule creation. This configuration provided results that were both

symmetrical every 90° and had spacing between detector input values that allowed for a rule set creation with distinct results at each point. Due to the possible drastic changes of inputs from position to position, new membership functions were created to accommodate the rapid rise and fall of values. Rather than ranking the membership values from 0-100 in increments of 25, the new membership functions were created in increments of 10. This allowed for more precise rules to be created and more accurate inputs from field trials to be used.

3.2 Standoff Distance Variation

As with any type of radiation detection equipment, there are limitations in the equipment's ability to detect the radiation. A few of these limitations include the minimum source strength the system is capable of detecting and the maximum distance the system can detect particles emitted from a radiation source. These two limitations are coupled to each other in that if a source has a higher activity, it will typically be detectable at a larger distance. To verify this postulation, various trials were conducted in MCNP6 with the system placed at the origin and a 100 μCi ^{137}Cs point source was placed at assorted distances ranging from 1 meter to 35 meters. The first 90° was the only portion of the 360° field-of-view that was examined due to symmetry. This setup is shown in Figure 3.14

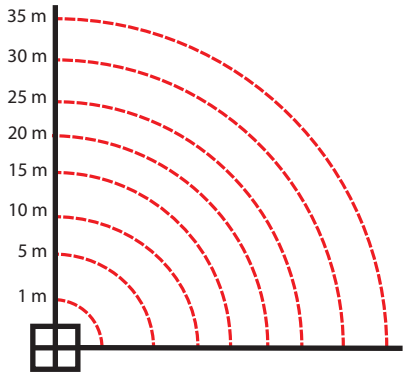


Figure 3.14: Standoff Distance Setup for First 90°

The results for the various MCNP6 simulations were examined at each distance and the gross counts from all four detectors were summed together. The sum of the gross counts for each distance was examined from 0° to 90° in increments of 22.5° and the results are shown in Figure 3.15.

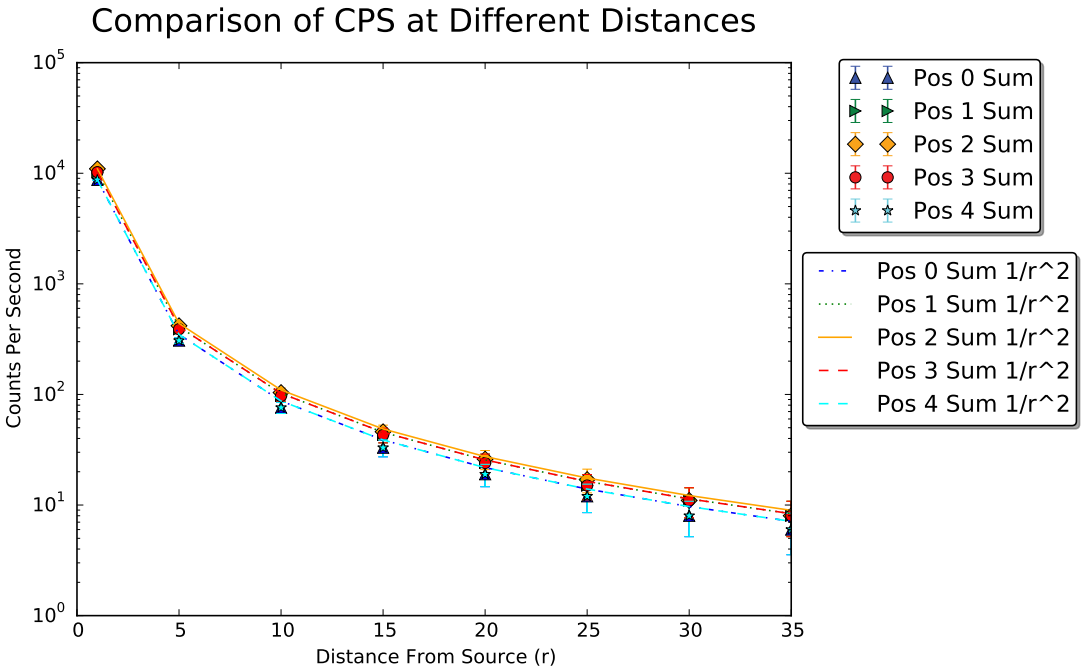


Figure 3.15: Comparison of Modeled Results to $1/r^2$ for First 90°

From Figure 3.15, one can see that the detected particles decrease at a rate of $1/r^2$. The maximum and mean of the four detectors' registered counts were also examined and also showed to follow the $1/r^2$ trend expected in radiation detection [13].

3.3 Rule Set Sensitivity Study

During initial testing of the algorithm, the fuzzy logic rule sets were created using MCNP6 modeling with a source placed at small distances less than 1 meter. After real-world tests were performed, it became evident that the rule sets designed for smaller distances would not be completely accurate if the sources were placed at larger distances. This is due to the area of view from the emitting source becoming

larger and making the occlusion principle of the detectors not quite as effective as with shorter distances. An illustration of this phenomenon is shown in Figure 3.16.

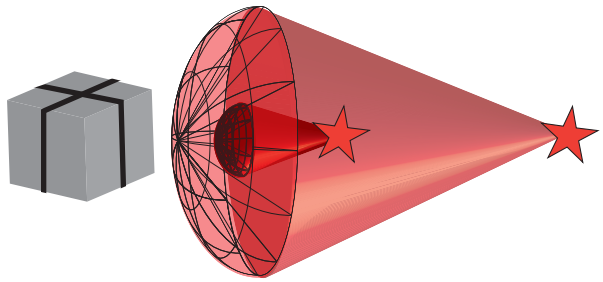


Figure 3.16: Distance Portraying Field-of-View for Various Distances

The cones in Figure 3.16 show the relative surface subtended by the solid angle. The solid angle, in steradians, is equal to the area of the segment of a unit sphere the object would cover. The solid angles of the cones pictured are the areas of the spherical caps calculated by

$$\Omega = 2\pi(1 - cos\theta) \tag{3.1}$$

where Ω is the solid angle in steradians and θ is the angle of a cone with apex angle 2θ. The position closer to the detectors is known as the *near-field* and the position further away is known as the *far-field* [14]. MCNP6 was used to show how the separation of the source and the detector array affected how many particles were incident on the face of the detectors. A ^{137}Cs source was placed at varying distances between 25 and 500 cm. An F1 surface current tally was evaluated at each location for the detector surfaces directly facing the source. This tally provides a simple count of the number of particles, represented by the Monte Carlo weight, crossing a surface through these surfaces. All of the detectors were modeled, but only the surfaces visible to a source at 45° were tallied. The two surfaces of detector 1 facing towards the source (green lines) were compared to the outer surfaces of detectors 2 and 4 (orange lines) in the field-of-view of the source as shown in Figure 3.17.

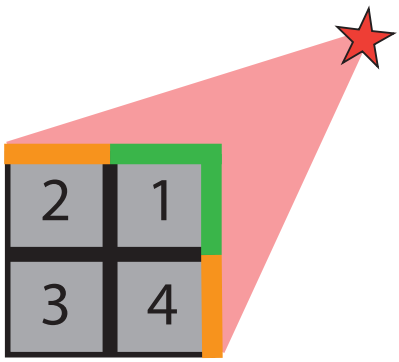


Figure 3.17: Illustration of Surfaces Used for F1 Tally Simulations for Near-Field/Far-Field Comparison

Using the calculated weights, a ^{137}Cs source was simulated at 45° for the various distances. The results for each position are shown in Table 3.6.

Table 3.6: F1 Tally Results for a ^{137}Cs Source Placed at Distances Between 25-500 cm

Distance (cm)	**Fraction of Particles Crossing Detector 1 (D_1) Surfaces**	**Fraction of Particles Crossing Detectors 2 & 4 (D_2+D_4) Surfaces**	$\frac{D_1}{(D_2+D_4)}$
25	4.09E-02	1.42E-02	2.88
50	7.31E-03	5.09E-03	1.44
100	1.54E-03	1.40E-03	1.10
200	3.54E-04	3.61E-04	0.98
500	5.40E-05	5.85E-05	0.92

From Table 3.6, it is evident that when the source is very near the array of detectors, detector 1 occludes the other detectors greatly. The F1 tally results show the number of particles crossing the surfaces of detector 1 to be 288% times those crossing both 2 and 4 at 25 cm. Between 100 cm and 200 cm, the field-of-view becomes such that the surfaces of detectors 2 and 4 begin to see a greater number

of particles. This showed the need for a rule set sensitivity study for near-field and far-field scenarios. The sensitivity study was performed testing the system response for a variety of rule sets created with different distances in MCNP6. The different distances used in this study were 1, 5, 10, 15, and 20 meters. All of the distances besides the 1m simulation had similar detector response curves as shown in Figure 3.18

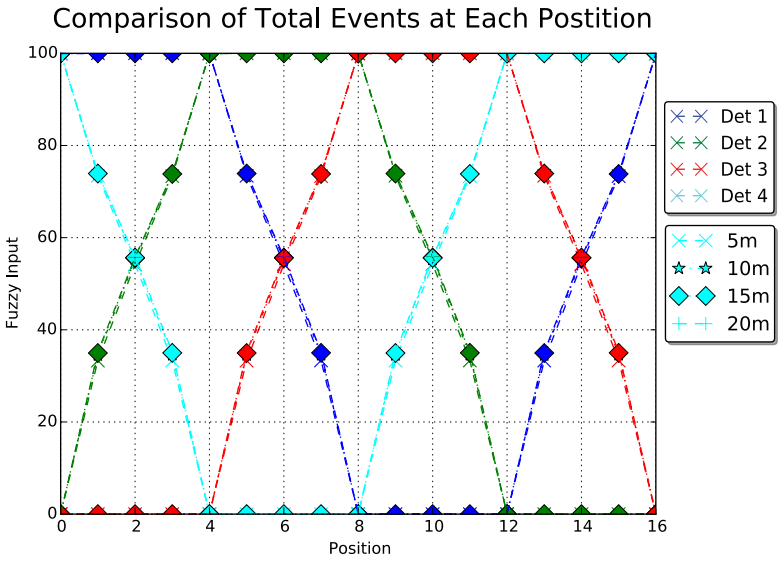


Figure 3.18: Response Curve Comparison for 5, 10, 15, and 20 Meters

Since the rule sets for distances between 5m and 20m were all the same, only one was chosen to compare to the 1m rule set. Figure 3.19 shows the difference between the response curves for 1m and 15m for the first four positions (90°).

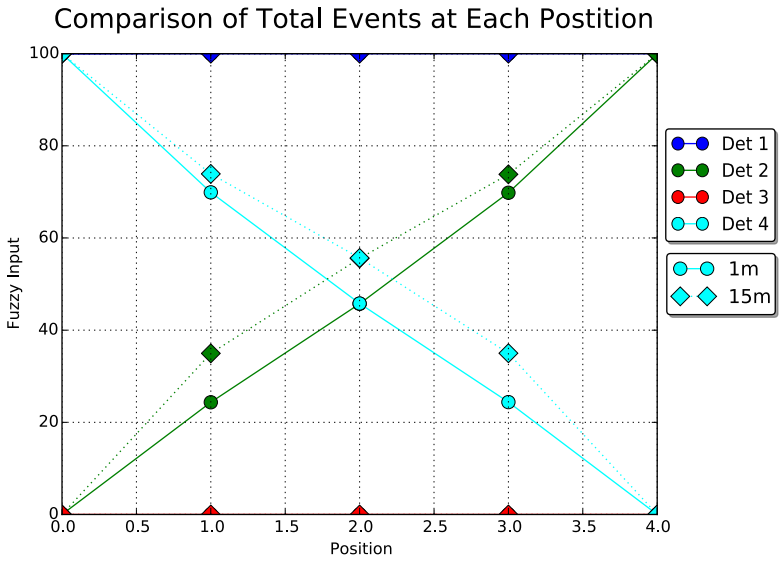
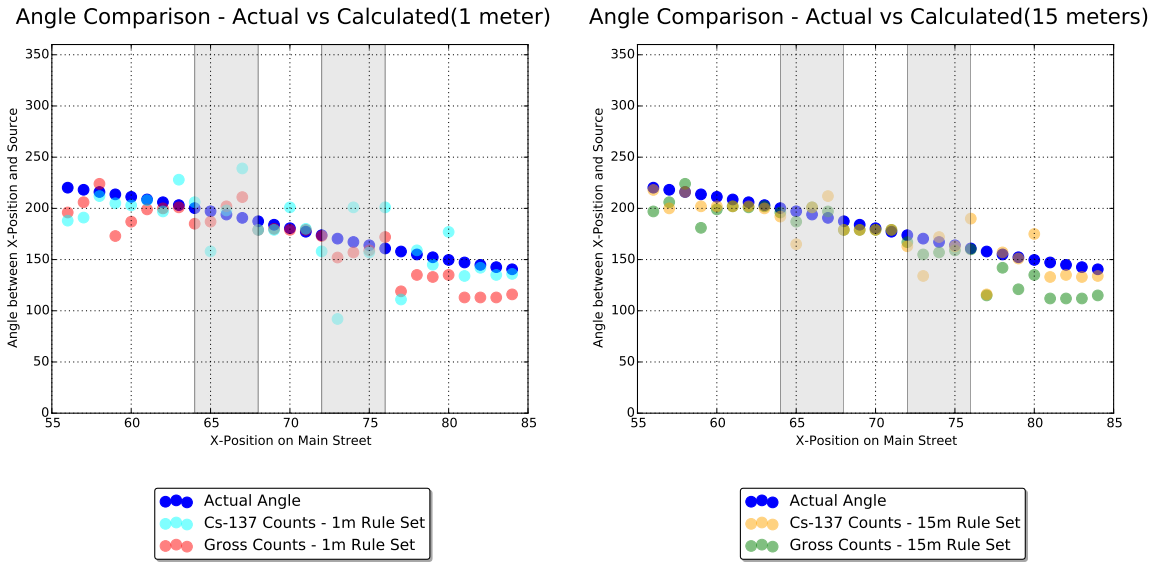


Figure 3.19: Response Curve Comparison of 1m and 15m for First 90°

Although most of the 360° positions are nearly the same, the slight variation between the rule sets produces erroneous results when used with actual data sets. Ideally, one would use the exact distance rule set for each case, but standoff distances are not typically known in real-world scenarios. The various rule sets were evaluated against each other using a data set collected at Fort Indiantown Gap, Pennsylvania. The distance from the source ranged between 16.5 and 25 meters with resulting angles ranging from 130° to 230°. The calculated angles using the various rule sets are compared in Figure 3.20.

Using the 1m distance model and gross counts from the X-cross NaI(Tl) system, the average variance from the known bearing was ± 18.5°. When using the 15m rule set, the calculated bearing was an average of ± 11.5° from the known angle. Since NaI(Tl) has the ability to provide energy resolution data on incident gamma radiation, the rule sets were compared for the energy peak from ^{137}Cs. The 1m rule set produced results with an average of ± 15.7° from the known bearing versus the 15m rule set that produced results within ± 14.1°.



(a) Results Using 1m Rule Set

(b) Results Using 15m Rule Set

Figure 3.20: Comparison of Directional Bearing Results Using 1m and 15m Rule Sets

3.4 Source Elevation Sensitivity Study

In an ideal search scenario, the elevation of the detector system and the source would be equal to optimize the occlusion of the detectors further away from the source. Unfortunately, this is typically not the case in real-world scenarios. A source may be at an elevation above or below the centerline of the system, and the response of the system is affected by the angle of elevation. To determine the sensitivity of the fuzzy logic algorithm and system setup to the angle of elevation, simulations were run at a distance of 1 meter for angles of 0°, 15°, 30°, and 45°. The fuzzy position results for the 360° azimuthal space were determined every 22.5° and the residuals from the known bearing are shown in Table 3.7.

Table 3.7: Residual Comparison for a 360° Azimuthal Space at Different Elevation Angles Expressed in Degrees Difference from Known Angle

Known Angle	**0° Elevation**	**15° Elevation**	**30° Elevation**	**45° Elevation**
0	4.48	4.49	4.48	4.48
22.5	3.57	3.74	3.68	3.57
45	0.85	0.43	0.58	0.85
67.5	0.20	0.18	0.19	0.20
90	0.01	0.01	0.01	0.01
112.5	0.12	0.10	0.11	0.12
135	0.46	0.10	0.23	0.46
157.5	0.10	0.09	0.09	0.10
180	0.03	0.03	0.03	0.03
202.5	0.11	0.08	0.09	0.11
225	0.51	0.16	0.29	0.51
247.5	0.08	0.06	0.07	0.08
270	0.06	0.06	0.06	0.06
292.5	0.14	0.11	0.12	0.14
315	0.52	0.27	0.34	0.52
337.5	1.58	3.17	2.61	1.58
360	4.48	4.49	4.48	4.48

From Table 3.7 it is evident that the elevation angle of the source affects the fuzzy systems capability to determine fuzzy bearing of the source. However, the effect is negligible for most of the positions along the 360° azimuthal space. The largest discrepancies from the known beings occur from $0° \pm 22.5°$. This can be attributed to the transition from 360° to 0°. The rule sets use the membership functions from both 22.5° and 337.5° when the source is between these positions. Although it does not produce a very large error in the results (<4.5°), this transition correction needs to be addressed in future endeavors. Nonetheless, the average deviation from the known angle was near 1° for all angles evaluated. The residual of the calculated angle

only increased less than 1° from the elevation of 0° to 45°, showing that the algorithm will provide results within 4.5°, regardless of the elevation of the source.

Chapter 4

System Development

4.1 System Design

The initial modeling of the detectors designated how the system design and layout would be organized. The system needed to be mobile in some fashion. The first iteration of the mobile system was designed to be placed on the bed of a flatbed truck. The system design was created to accommodate a four-detector system placed in a "Four-Quadrant" setup. Two stainless steel troughs were made to house the detectors and the lead cruciform. The detectors and lead were placed between the two pieces with the photomultiplier tubes being accessible to connect the necessary wiring as shown in Figure 4.1.



Figure 4.1: Four-Quadrant Detector Setup with Stainless Trough

The detectors needed to be placed high enough above the truck bed and cab to increase the line-of-sight to the detectors. To achieve this, a base and pedestal were created to house the detectors, as shown in Figure 4.2.

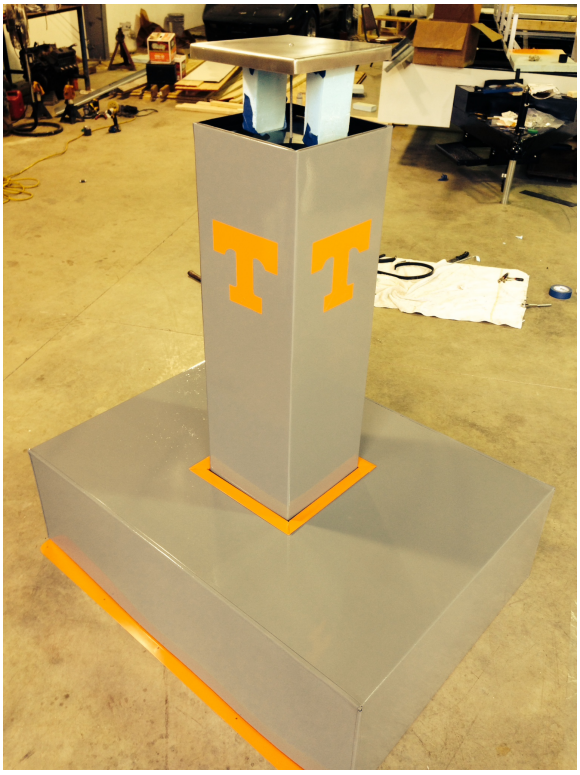


Figure 4.2: Base and Pedestal Setup for Flatbed Detector System

The equipment in this system included:

- 4 - 5”x5”x6” EJ200 Plastic Scintillator Detectors
- 1 - Pixie-4 DAQ in National Instruments Crate
- 1 - Dell Optiplex PC
- 1 - Canberra Model 1000 Portable NIM
- 2 - ISEG Dual Channel HV
- 1 - Marine Battery and Inverter

Due to the large amount of space required for these components, they were placed in a crate separate from the detector housing. The detectors were placed upside down on top of the pedestal and wiring was run to the crate containing all associated electronics and power supplies as shown in Figure 4.3.



Figure 4.3: Mobile System Prototype Setup

This initial design was used to validate the feasibility of the system in a mobile setting. A 2 mCi ^{137}Cs source was placed within the trunk of a car located in the

University of Tennessee's Motor Pool parking lot. The search truck with the detector system was then driven around the lot to attempt to determine the directional bearing of the source. Although this system was capable of locating the radiation source, the system lacked the ability to provide user feedback in a speed that would be useful at higher search vehicle speeds. This system was also designed to be placed on a utility cart; however, this setup did not require the detectors to be housed between the two troughs as they were placed with the photomultiplier tubes facing upward.

Although the initial design provided results showing the system was in fact capable of determining the bearing in a realistic setting, the size of the system and user feedback response needed further development. The second iteration of the system design included more compact and upgraded system components including:

- 4 - 2"x4"x16" NaI(Tl) Detectors
- 1 - CAEN DT5781 MCA/DAQ
- 1 - CAEN DT1470ET 4ch HV Supply
- 1 - Dell Micro PC
- 1 - Marine Battery and Inverter

A benefit to this new equipment was the updated digital acquisition system had the capability to be communicated with directly. The initial system design was designed such that the data acquisition system would receive the signals from the detectors and write the output to a new file on the disk as fast as every 0.1 seconds. Although this speed would be a sufficient refresh rate, the output needed to be read by a separate program to provide a directional bearing. This process only had the capability to refresh every few seconds due to the on-disk reading and writing of new files. This latency in updating was inefficient in a "live" feedback scenario. The CAEN DT5781 allowed for registered counts in the detectors to be read directly off

of the MCA and therefore provided a more effective feedback without the delay of unnecessary reading and writing to the disk. With the assistance of Dr. Ondrej Chavala, an updated graphical user interface (GUI) was designed which utilized the direct communication with the DT5781 (via the device firmware). The GUI also applied the fuzzy logic algorithm to the detector inputs and provided a near-instantaneous feedback by eliminating unneeded hard disk write and read functions, thereby eliminating I/O latency. Figures 4.4 and 4.5 show an example of a histogram plotting and directional arrow feedback features of the GUI.

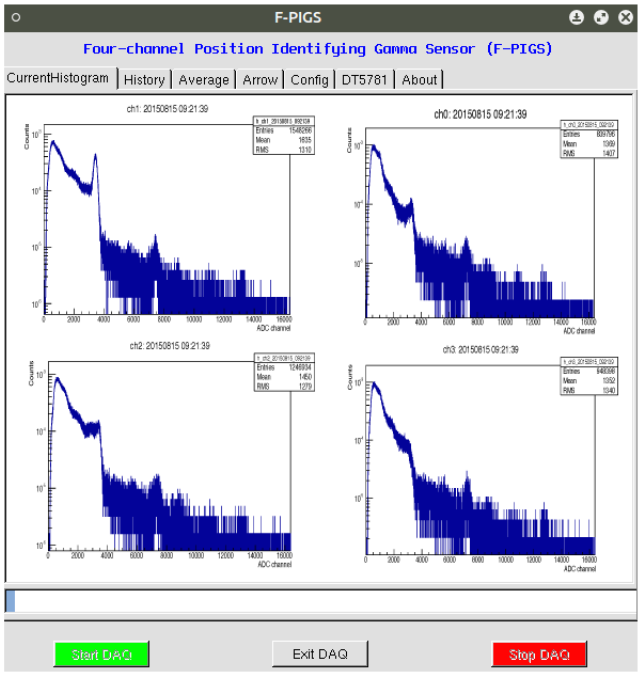


Figure 4.4: Screenshot of GUI Showing Multiple Channel Histogram Plotting

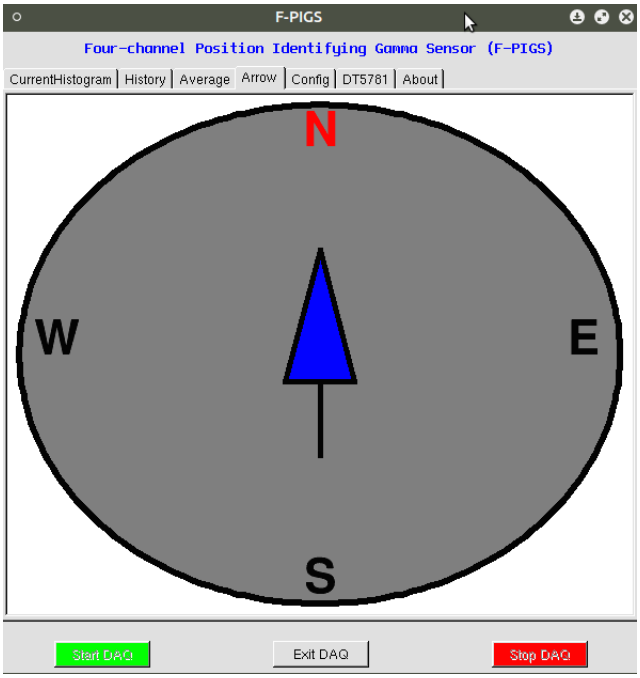


Figure 4.5: Screenshot of GUI Showing User Feedback Directional Arrow Controlled by Fuzzy Results

With the decrease in system size, the entire system could then be housed within a universal car-top carrier capable of being affixed to most vehicles equipped with roof racks. The small size also allowed the system to be placed on a utility cart for easier handling and testing of the system's performance. This setup is shown in Figure 4.6



Figure 4.6: System Setup on Mobile Cart

To accommodate the non-symmetrical 2"x4"x16" NaI(Tl), the "X-Cross" configuration was designed. The initial design had the detectors facing 45° from the center point, however this was modified to fit the dimensions of a car top carrier. The detectors were mounted to a removable shelf that was able to be placed within the carrier or on the cart. The angle of the detectors on this shelf were angled 60° from the x-axis in their respective quadrant as shown in Figure 4.7 with a 2 cm lead cruciform placed in the center.



Figure 4.7: X-Cross Setup on Mobile Cart

4.2 Background Radiation Studies

Natural gamma-ray background radiation is present nearly everywhere and can make detection of illicit sources more difficult. When considering a mobile detection system, this becomes an even greater issue due to variable amounts of background radiation within a search area [15]. Naturally occurring gamma background radiation can cause a detection system to be less sensitive to sources because of the difficulty of distinguishing between background and source counts [16]. Figures Figs. 4.8 to 4.10 show how concentrations change throughout the United States for ^{40}K, ^{232}Th, and ^{238}U, respectively [17].

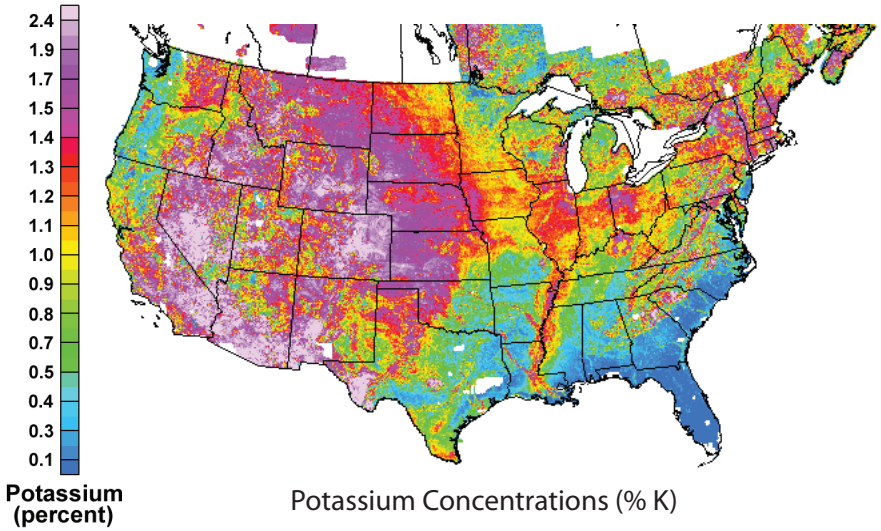


Figure 4.8: Naturally Occurring ^{40}K Concentration Across the United States as mapped by the United States Geological Survey (USGS) [17]

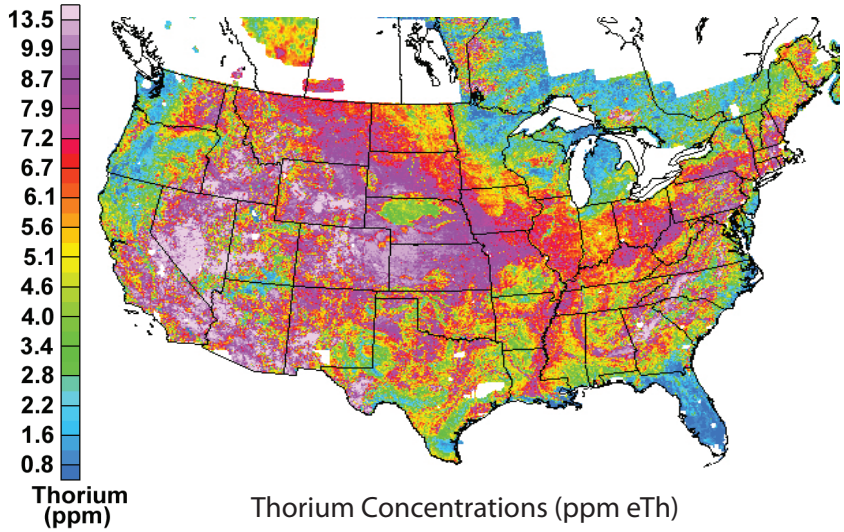


Figure 4.9: Naturally Occurring ^{232}Th Concentration Across the United States as mapped by the United States Geological Survey (USGS) [17]

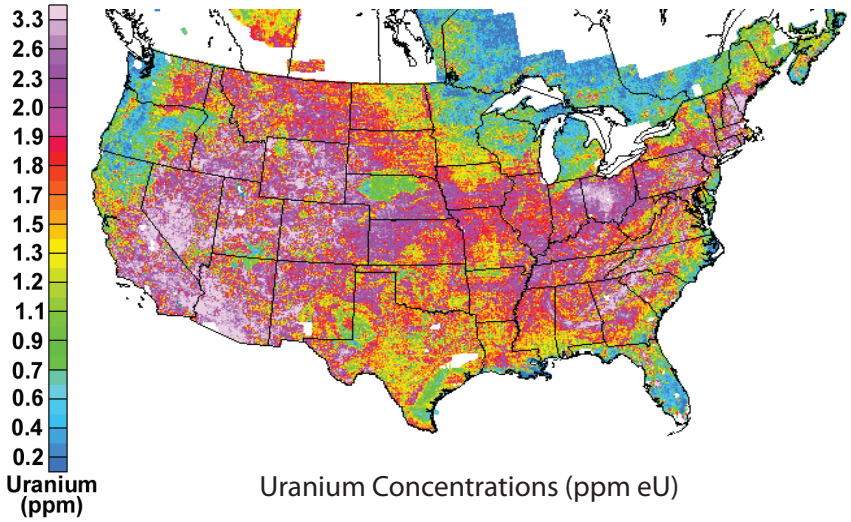


Figure 4.10: Naturally Occurring ^{238}U Concentration Across the United States as mapped by the United States Geological Survey (USGS) [17]

Figures Figs. 4.8 to 4.10 show the importance of understanding the relative background near the areas of interest when trying to detect sources that have relatively low activities compared to background. To determine how many counts detected are coming from the source, the net counts are calculated using Equation 4.1. In this equation, N_S is the net counts from the source, N_T is the total counts detected, and N_B is the counts from background [18].

$$N_S = N_T - N_B \tag{4.1}$$

In radiation counting measurements, the Poisson distribution is used since the probability of occurrence of radioactive decays is constant and small, and the resulting outcome from counting experiments is an integer number describing how many counts have been recorded [19]. The Poisson distribution applies to radiation counting measurements by meeting the four requirements of the distribution[20].

1. All nuclei have the same probability of decay for a given time period.

2. The decay process of one nucleus is not affected by the decay of another nucleus.

3. The total number of nuclei and measurement times are sufficiently large.

4. The nuclei half-life is long compared to the detection pulse.

Radioactive decay is therefore a random process in which a discontinuous random variable is the number of times the decay event takes place in a timeframe [20]. The Poisson distribution takes the form

$$P(x) = \frac{(\bar{x})^{\mathrm{x}} e^{-\bar{x}}}{x!} \tag{4.2}$$

Where $\bar{x}$=pn, with the number of trials being n and the individual success probability denoted by p [18]. For a counting system where Poisson variations are used, the standard deviation for the net counts is shown by Equation 4.3.

$$\sigma_{N_S} = \sqrt{\sigma^2{}_{N_T} + \sigma^2{}_{N_B}} \tag{4.3}$$

The net counts in Equation 4.1 is compared to a critical level of detectability, $\mathrm{L_C}$, to determine if there is a source present. Assuming a Normal distribution as shown in Figure 4.11, if $\mathrm{N_D}$ is the minimum value $\mathrm{N_S}$ needs to be to ensure a 5% false-negative probability,

$$N_D = L_C + 1.645\sigma_{N_D} \tag{4.4}$$

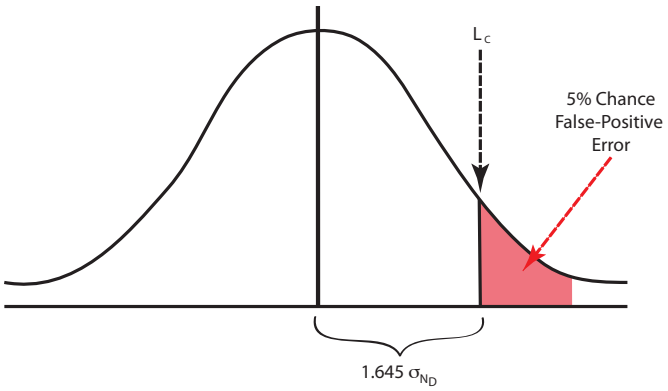


Figure 4.11: Decision Level L_C Assuming a Normal Distribution

Where

$$\sigma_{N_D} = \sqrt{N_D + 2N_B} \tag{4.5}$$

N_D can be then be derived to equal

$$N_D = 4.65\sqrt{2N_B} + 2.71 \tag{4.6}$$

Equation 4.6, known as the the "Currie equation" [21], provides the minimum number of counts needed from a source to ensure a false-positive rate of less than 5%. A false positive occurs when a detection system indicates there is a source present when in reality there is not. On the other hand, a false negative is when the system fails to detect a source that is actually present. The relationship between false positives and false negatives to L_C and L_D is shown in Figure 4.12 [22].

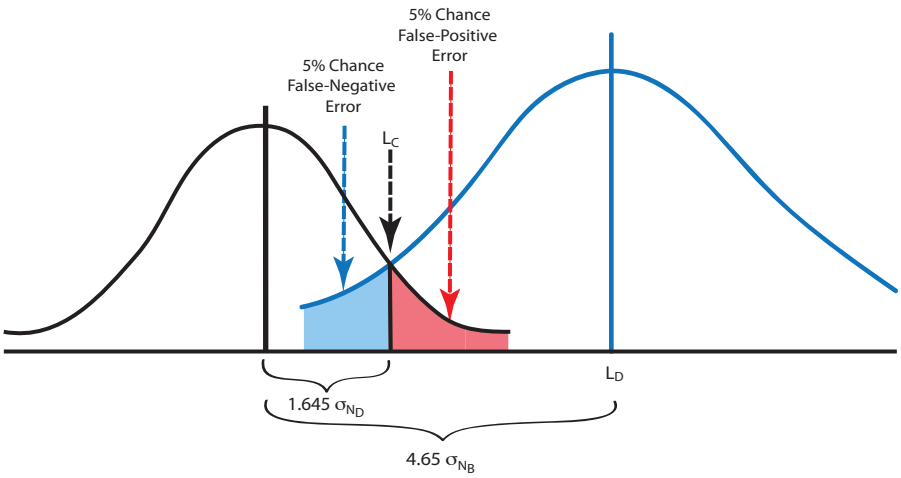


Figure 4.12: Detection Limit L_D and Associated False Positives/False Negatives

An important test of the system was to determine how well it could detect a radioactive source with the presence of background radiation not accounted for in the model. This involved surveying the testing area of Fort Indiantown Gap. The background studies were performed to provide a detailed radiation map of the facility and allow source injection studies to be performed.

4.2.1 Background Radiation Sources

The original design of the system was to determine the azimuthal angle of a radiation point source. If the system was modified to determine the elevation angle instead, it could determine the bearing of the largest contributor to the background radiation at that location. The system was modified to use the large NaI(Tl) detectors stacked in a horizontal four quadrant layout with a lead cruciform as shown in Figure 4.13.



Figure 4.13: Detector Setup for Elevation Angle Measurements

Using this setup placed on the mobile cart, static measurements were made at thirty-seven various points throughout the urban town in Fort Indiantown Gap, Pennsylvania. A map of the location and points measured is shown in Figure 4.14.



Figure 4.14: Background Measurement Points at Fort Indiantown Gap, Pennsylvania

Measurements were performed at each of these locations to determine what natural sources contributed to the background radiation. Analysis of these measurement results allowed the bearing of the largest contributor of background radiation to be determined. There are many contributors to a background radiation spectrum, each with varying concentrations depending on the surroundings. The background sources

and associated energies typically seen in a gamma background spectrum are listed in Table 4.1.

Table 4.1: Background Gamma Sources and Associated Energies

Source	Energy
^{214}Pb	352 keV
^{208}Tl	583 keV
^{214}Bi	609 keV
^{228}Ac	911 keV
^{228}Ac	969 keV
^{214}Bi	1120 keV
^{40}K	1460 keV
^{214}Bi	1765 keV
^{208}Tl	2614 keV

This measurement campaign was performed with the NaI(Tl) detectors, therefore individual energy peaks can be assessed as well as the gross spectrum. The average gross count rate for each of these locations is shown in Figure 4.15.

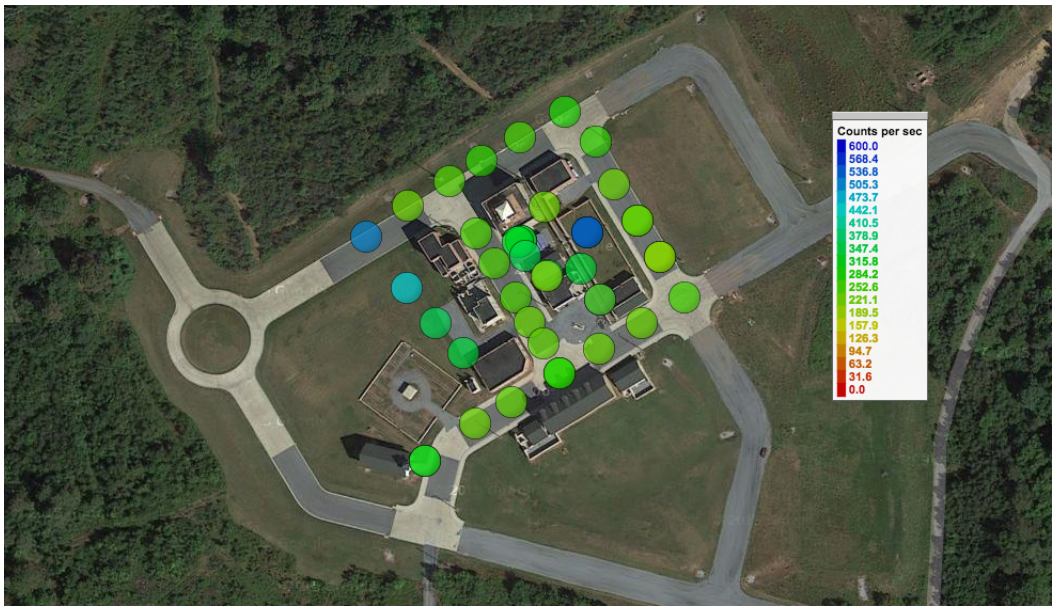


Figure 4.15: Average Gross Count Rate from Background at FIG Measurements Points

For each of these locations, the algorithm was applied to each energy peak and the gross counts. Results for point 16 on the map in Figure 4.14 are shown in Figure 4.16.

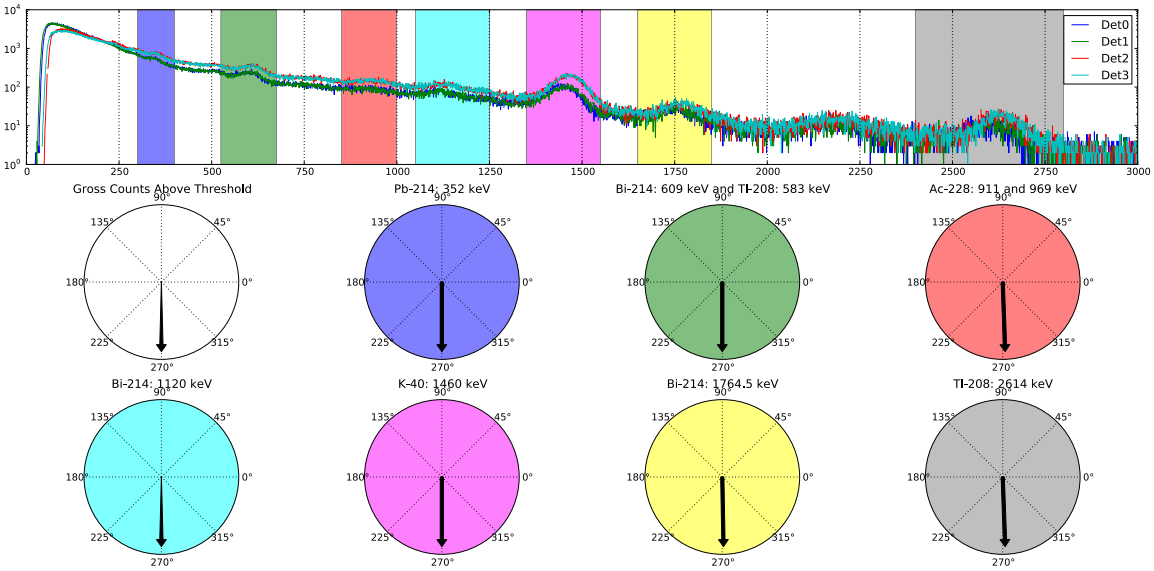


Figure 4.16: Elevation Angle Results for Measurement Point 16 at Fort Indiantown Gap, Pennsylvania

Point 16 was in the center of a concrete pad that was located a few meters away from any other potential background contributors. At many of the locations, including point 16, the largest background contributor was the ground beneath the detector system. This caused the compass arrow to point nearly straight down toward the ground. However, at locations where the surrounding ground was not homogeneous, the bearing results varied. At locations where there was grass near the concrete or asphalt on which the system was placed, the results showed that the ground with grass on it was the largest contributor to the background radiation at that point. The measurement at point 9 was taken with the system placed on asphalt, but was within 1 to 2 meters from the grass. The results from this measurement are shown in Figure 4.17.

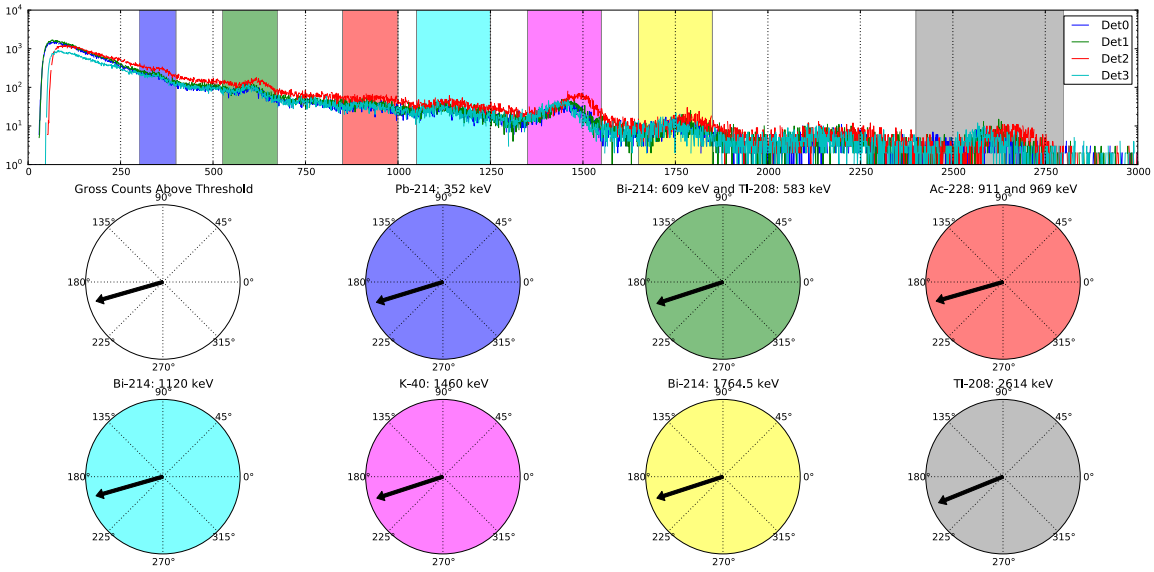


Figure 4.17: Elevation Angle Results for Measurement Point 9 at Fort Indiantown Gap, Pennsylvania

The results from Figure 4.17 show the location of the of the largest background contributor to be located near 220°. Using a height of 1 meter for the system, the largest background source would be calculated to be 2.75 meters away. Although this does not point to the edge of the grass and asphalt, it does show the direction of the grass to be the largest contributor. Due to the low number of counts detectable from background, the counting time to acquire background measurements was ideally 30 minutes or greater. However, due to the large number of measurement points, that time had to be shortened to 15 minutes at some locations to ensure all points were measured. The drawback to these shortened times was that the counting statistics for some of the photopeaks were less than ideal, showing the importance of larger count times when measuring background to ensure there is a sufficient amount of counts under each photopeak. This influenced the results of the ^{208}Tl location to sometimes have a variation in the bearing determination from the other uranium decay series products. An example of this observation at measurement point 8 can be seen in Figure 4.18.

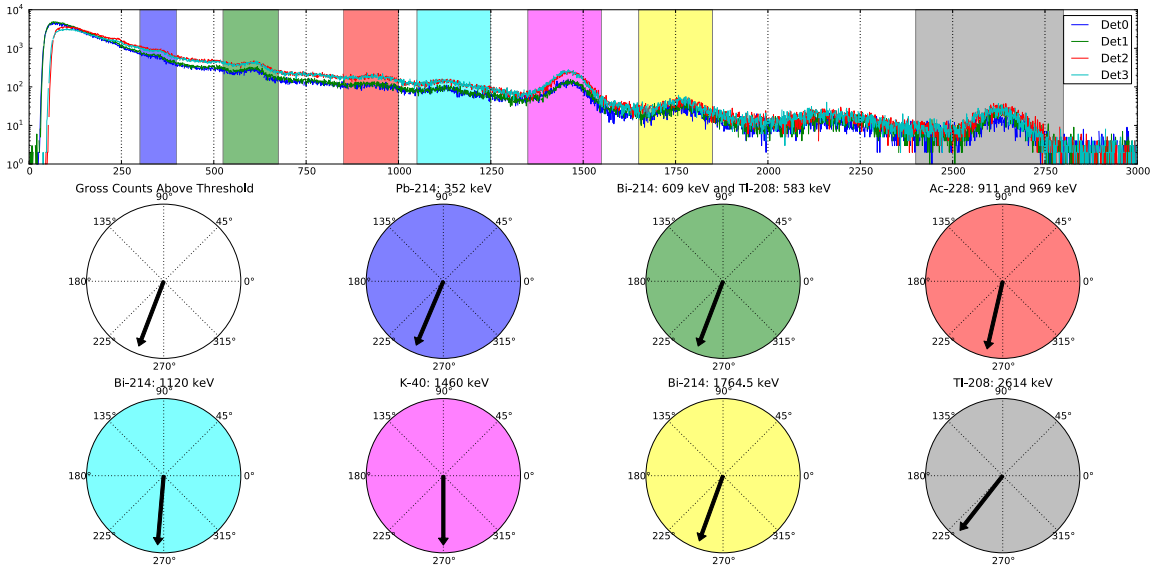


Figure 4.18: Elevation Angle Results for Measurement Point 8 at Fort Indiantown Gap, Pennsylvania

This position was roughly 3 meters from asphalt to the right, front, and rear. The grass to the left of the system was nearly 2 meters from the system. Rather than pointing directly down (270°) for every photopeak, many of them showed a bearing between 240° and 255°. This result would suggest that the concrete is the major contributor at the location (an ideal bearing straight downward), but is influenced by the grass as well (the bearing is skewed slightly to the left towards the grass). See Appendix A for results from other elevation angle results at additional measurement points at Fort Indiantown Gap, Pennsylvania.

This setup was also used to measure how background might change over a short period of time. Measurements were performed at four different locations in the morning and then measured again later in the day after the temperature increased. The comparison of the average count rate at each of these locations and times is shown in Figure 4.19

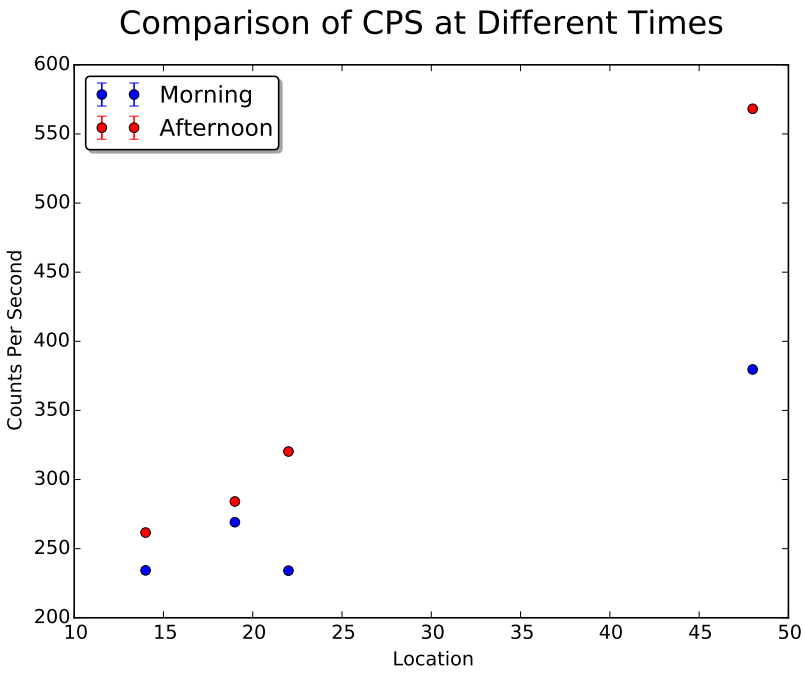


Figure 4.19: Average Gross Count Comparison for Different Times of the Day (Error Bars Not Visible)

From Figure 4.19, it is evident that there is an increase in the background rate as the temperature increased throughout the day. Positions 14 and 19 were on the centerline of an asphalt road and showed only an increase of 27 and 15 counts per second, respectively. Point 22 was located on the sidewalk less than 1m from grass and showed an increase of 86 counts per second. The largest increase occurred at point 48, which was in a grass courtyard completely surrounded by grass. This location had an increase of 189 counts per second from the morning to the afternoon. These large increases near the grass can be attributed to the release of radon gas as the temperature increased throughout the day.

From the background measurement campaign, a few conclusions can be drawn. The first would be that the bearing of the material with the highest background radiation contribution at each location can be determined with the system set up to measure elevation angles. The results also showed that the location of the system relative to its surroundings influences the results of the bearing determination. For

example, if the system was placed on the center of a homogeneous surface with no other surroundings, the bearing would be directly downward (as shown at point 16). However, if the system is placed near a mixture of surfaces, as at point 9, the surface with the greatest influence will control the bearing determination. Grass, concrete, and asphalt are all known to contain various amounts of uranium, thorium, and potassium [23]. The concrete surfaces had an overall higher number of counts from background than the asphalt measurements, as was expected due to the greater density and composition of concrete. The results showing grass being the greatest contributor at locations on or near grass suggest that the most influential material to background radiation was the grass and soil. The gross count comparison relative to time agreed with this statement, showing the soil measurements to have the greatest number of gross counts. As the day progressed and the temperatures increased, the count rates increased as well, suggesting a release of radon gas from the soil as a potential cause for the increase. The time comparison measurements showed that background count rates are dependent on when measurements are taken and warrant the tracking of environmental variables that might influence the background measurements.

Chapter 5

Urban Environment Modeling

The end goal of this system was to provide a functional device for detecting radiation in real-world settings with the capability to determine directional bearings of sources in those settings. The two setups that would be applicable to real-world scenarios were a generic parking lot and an urban training facility.

5.1 Parking Lot

Since vehicles are typically part of a realistic urban environment, a model was created of a parking lot to assess the performance of a vehicle-based search system. The first step in modeling the parking lot was to create the vehicles that would be placed within the model. A generic car was created with a 1 cm thick steel frame filled with various air pockets for the cab and trunk placed on four rubber tires. The engine of the vehicle was left as a solid steel block, which was a very conservative approach in that actual engines would be less attenuating than a solid block. The car's dimensions were 1.83 x 4.6 x 1.6 meters. A three-dimensional model of this vehicle is shown in Figure 5.1.

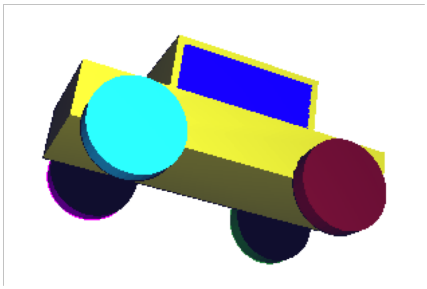


Figure 5.1: 3D Model of Vehicle Used in MCNP

As in actual parking lots, cars are oriented in a variety of ways. They can be in horizontal or vertical rows and face either toward or away from the rows' centers. The model includes two vertical rows located next to three horizontal rows with various orientations of cars placed 3.17 meters apart from each other and row spacings of 5.4 meters. All of the cars in the vertical rows face west. The horizontal rows are laid out such that the first row's vehicles are all facing north with the trunks near the middle row. The middle row has every other vehicle facing opposite directions and the bottom row is oriented the same as the top. This provides two rows capable of providing different response profiles. This model is shown in Figure 5.2

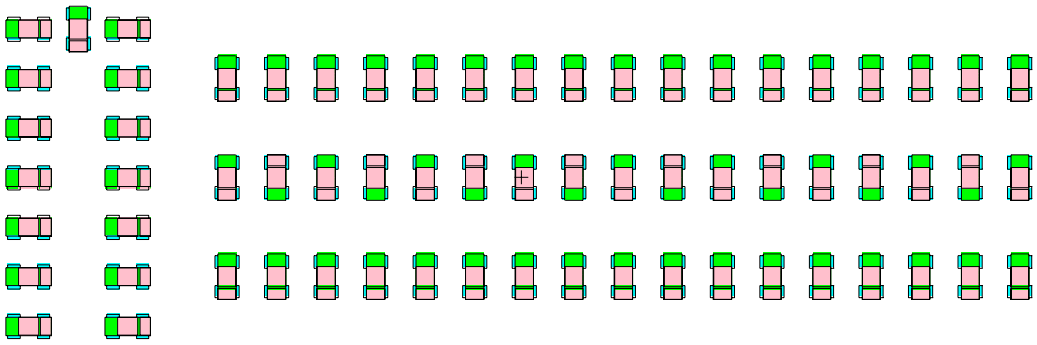


Figure 5.2: MCNP Model of Parking Lot

This configuration allowed for a variety of scenarios to be modeled to determine how the system might perform in a parking lot. The two main concerns for this environment were distance and shielding from the vehicles in the rows that affect

the performance of the system. The distance between the source and the detector system is one factor that determines how many particles could possibly interact with the detectors based off of the inverse-square law. The inverse-square law states that the detectable intensity from the source decreases at a rate of $1/r^2$, where r equals the distance to the source [24]. The other factor within this model that affected the amount of detectable events from the source was the shielding from the vehicles between the source and the detectors. The spacing between the cars allowed for particles to travel between the cars, but this attenuated most all of the particles traveling through the vehicle.

With the base parking lot model created, a variety of scenarios was created placing a vehicle with detector assembly on the roof and a ^{137}Cs source placed within different trunks among the rows. These scenarios were modeled with the source being placed in 15 different positions and the detector assembly car placed at 25 different positions for a total of 375 different scenarios. The various points at which the source and detector car were placed are shown in Figure 5.3

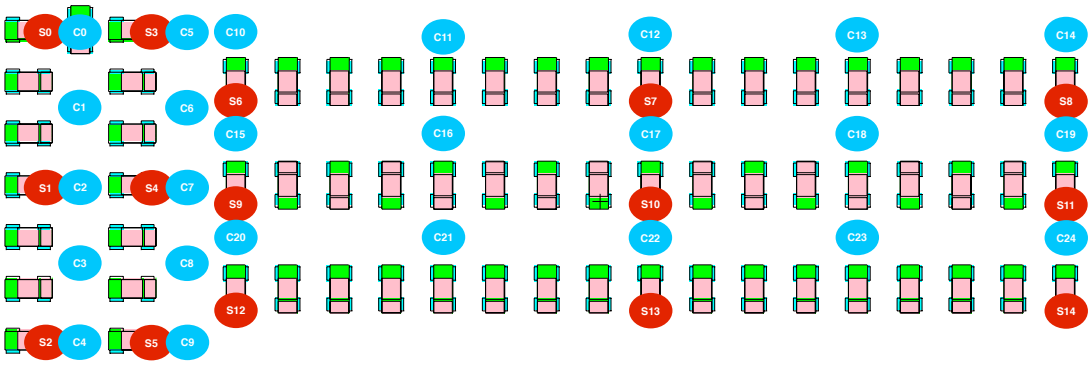


Figure 5.3: Possible Locations of Source (S) and Detector Car (C)

This model is useful in determining how well the algorithm is capable of determining the correct directional bearing at a variety of distances and shielding between the detector system and the source. For each of the possible scenarios, ^{137}Cs source was simulated to determine the algorithm's response at the various detector

locations. The results for when the source was placed at location S0 and detector car at each possible location are shown in Figure 5.4

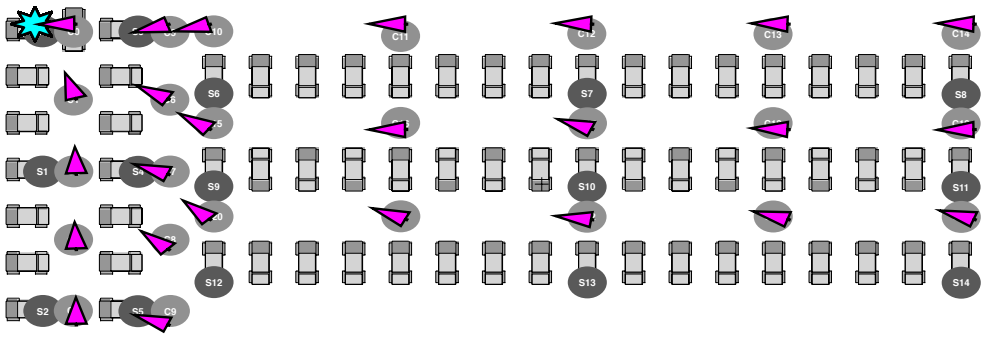


Figure 5.4: Algorithm Response with Source at Location S0

From Figure 5.4, it is evident that the algorithm was capable of determining the general direction of the source location. The directional arrows pictured are equally weighted, however these results are not an accurate representation of how well the system could perform based off the number of counts deposited in each detector. The fuzzy logic inputs for the directional results shown were the MCNP F8 tally responses for each of the detectors. This tally performs a balance of energy deposited into and lost from the tally volume which corresponds to a pulse. When an incoming particle crosses a surface, the energy times the weight is subtracted from the account of the cell it is leaving and is added to the account of the cell it is entering. At the end of the history, the pulse account in each tally cell is divided by the source weight. These pulses are then binned by energy and tabulated as a relative contribution from the number of source particles. Gaussian Energy Broadening was also used to account for changes in the full width half-maximum characteristics of the NaI(Tl) detector.

The results of the F8 tally provided a fractional response for the detector response for each energy bin. This did not directly provide the number of counts per second seen by the detectors, but allowed that to be estimated. By multiplying the tally results for each bin by the desired activity of the injected source, the detector response in counts per second could be determined. Since the source was placed in a shielded

steel trunk, a 10 mCi source was used to test the algorithm and the results are shown in Figure 5.5

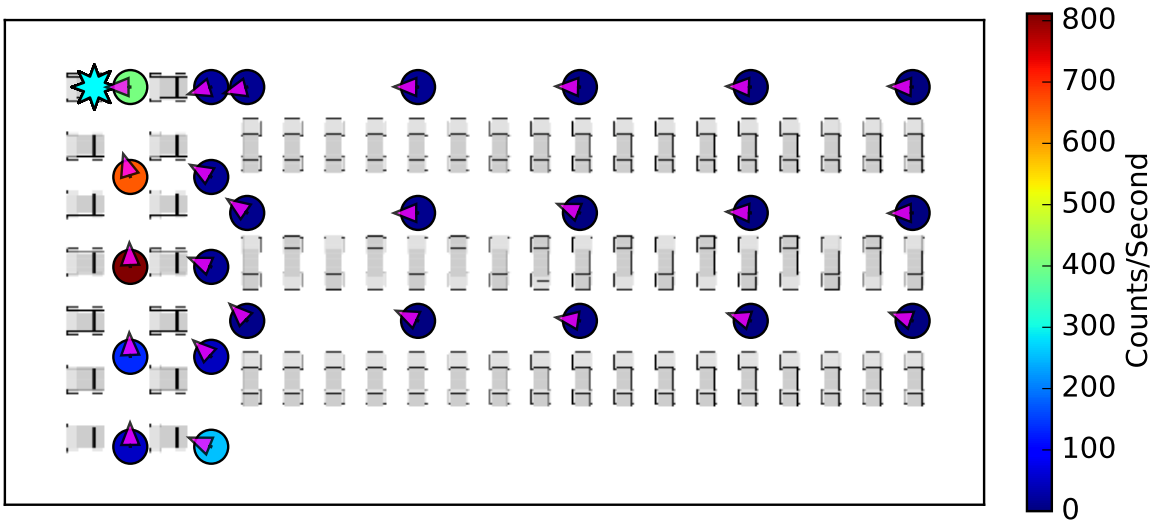
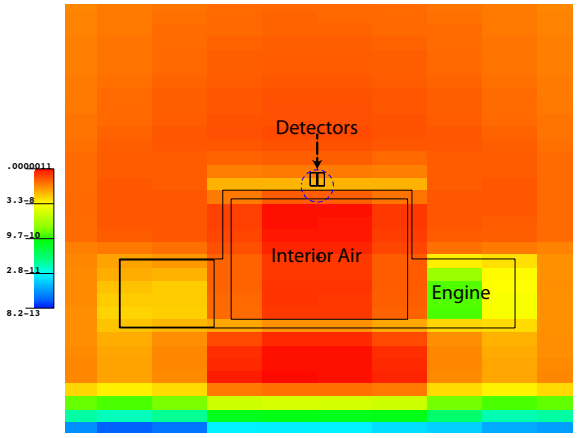


Figure 5.5: Counts per Second Response with Source at Location S0

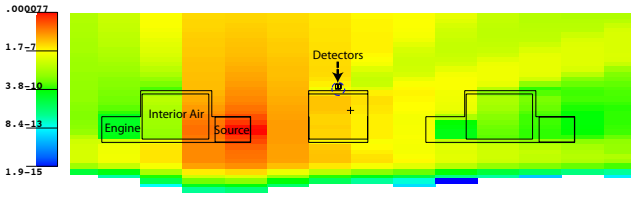
The results in Figure 5.5 show that when the detector system is placed further than two rows away from the source, the counts deposited are less than 100 counts per second with many locations seeing only a few counts per second. When considering the minimum detectable number of counts, the associated background must also be evaluated. The average background rate from FIG measurements was rounded to equal 400 counts per second and was used as the background rate within the parking lot model. Utilizing the Currie equation [21] and the average background rate, the number of particles detected from the source needed to be greater than 96 counts per second. This shows that many of the detector locations within the model would not be able to detect the source with less than a 5% false positive rate. See Appendix B for results of directional determination data for the other parking lot scenarios.

Although the system proved to be capable of determining the directional bearing on the adjacent rows, the system registered more counts when placed at a location not directly adjacent to the source. The reason for this is due to the detectors being located at a higher elevation than the source, causing there to be more shielding

between the source and detectors. The outer shells of both the car housing the source and the car coupled to the detector shield the detectors as shown in Figure 5.6



(a) MCNP Mesh Tally in XZ Plane



(b) MCNP Mesh Tally in XZ Plane

Figure 5.6: MCNP Mesh Tally of Source at S0 and Detector Car at C0

The two major factors that affect the detection capabilities of the system are distance and shielding from the source. Although the positions that are closer to the source should be able to detect more counts, the line-of-sight from the source to the detectors is obstructed by shielding from the car. As the detectors move away from the source, the count rate decreases at a rate of $1/r^2$ where r is the distance from the source. However, the line-of-sight to the source becomes less obstructed by shielding and therefore has the ability to detect more counts. This concept is shown in Figure 5.7.

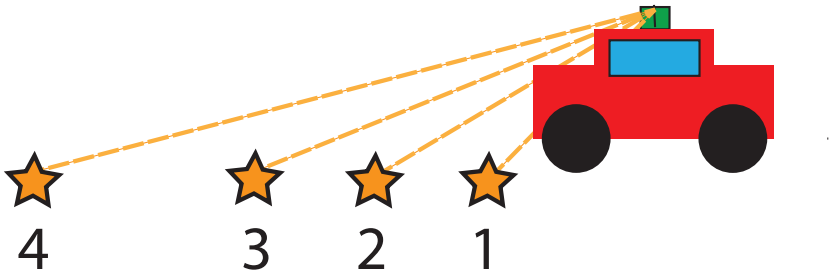


Figure 5.7: Line-of-Sight Comparison for Various Distances

It is evident from Figure 5.7 that as the source (denoted as a star) moves further from the detectors atop the car, the line-of-sight becomes less obstructed. At position 1, the line-of-sight is hindered by nearly the entire height of the car. On the other hand, position 4 has an uninhibited view to most of the detectors.

5.2 Urban Source Search Testing at Fort Indiantown Gap, Pennsylvania

Another scenario was modeled for algorithm testing and verification using part of an urban training facility in Fort Indiantown Gap, Pennsylvania, as the design basis. Located near Harrisburg, Pennsylvania, Fort Indiantown Gap serves as one of the busiest National Guard training facilities in the United States. The base is comprised of a variety of "ranges" that facilitate small/large arms training, tank training, air support training, and a variety of other training capabilities. One of the ranges on the base, Range 30, serves as the Combined Arms Collective Training Facility (CACTF). This range is a mock version of an urban environment, including streets, sidewalks, buildings, etc. A satellite image of this facility is shown in Figure 5.8.

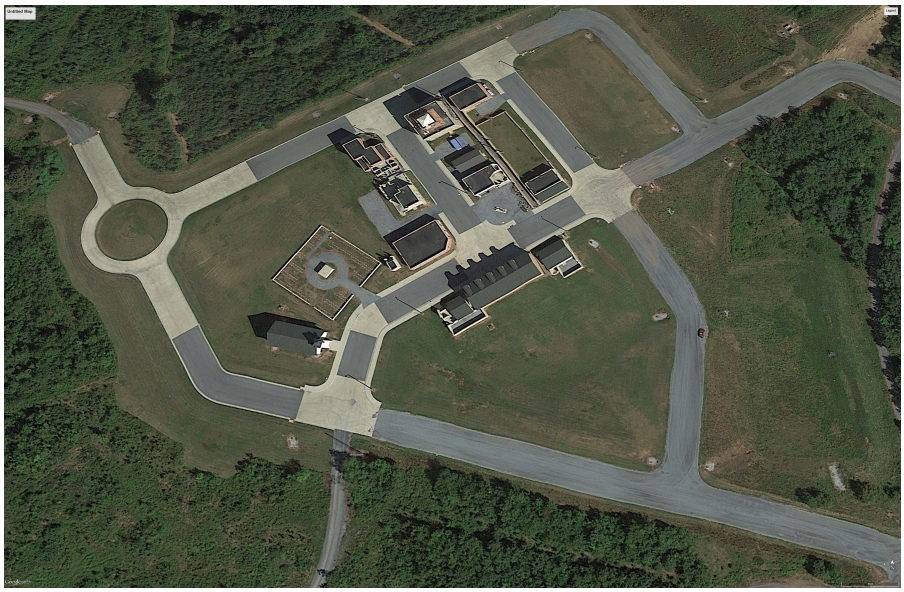


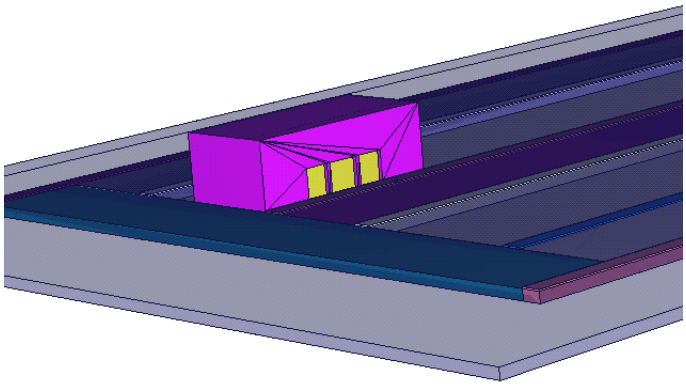
Figure 5.8: Satellite Image of Fort Indiantown Gap, Pennsylvania

One of the mock buildings within this facility is a three-story hotel with a basement. Having access to this building allowed for the construction of a simplified model of the hotel for use in simulations to test the detector algorithm. Pictures taken on the site and satellite imagery were used to estimate the dimensions of the hotel. The shell of the hotel was created using concrete that was 2.52 inches (6.35 cm) thick, which was the equivalent thickness of a standard cinderblock [25]. A door opening and two concrete pillars were added to the hotel facade followed by a concrete sidewalk and asphalt roadway.

On-site data obtained from tests made it possible for a variety of scenarios to be modeled and compared. A ^{137}Cs source was placed in the center of the hotel and the detection system was placed in the center of the roadway. With the system placed along the center axis of the hotel, it was moved in 1 meter increments 14 meters up and down the x-axis to simulate actual tests that were performed. The model and actual hotel are shown in Figure 5.9.



(a) Hotel and Street at Fort Indiantown Gap, Pennsylvania



(b) MCNP6 Model of Hotel and Street

Figure 5.9: Comparison of Actual and Model of Hotel at Fort Indiantown Gap, Pennsylvania

5.2.1 Model Verification

A series of measurements were made at Fort Indiantown Gap, Pennsylvania, with a bare 36 mCi ^{137}Cs source placed within the hotel modeled with MCNP6. The ^{137}Cs source was simulated using a 662 keV gamma source. As ^{137}Cs decays to ^{137m}Ba, it has a branching ratio of 94.6%. Then ^{137m}Ba decays via a 662 keV gamma ray with a 89.9% branching ratio, causing the total branching ratio for ^{137}Cs to be 0.851. The simulation results were scaled by this branching ratio and specified activity to

determine the amount of activity in terms of becquerels of ^{137}Cs. The source was placed in the center of the hotel with the system placed in the center of the roadway in front of the hotel. The system was operated with both the four-quadrant and x-cross setup placed on the mobile cart. Static measurements were made at points located ± 14 meters from the centerline of the hotel, as was done in the model. The four-quadrant setup was placed on the bottom of the cart and was equipped with four EJ200 detectors, which provided useful gross counting results. The sum of the gross counts were compared for each location and the results were overlaid on a satellite image shown in Figure 5.10.

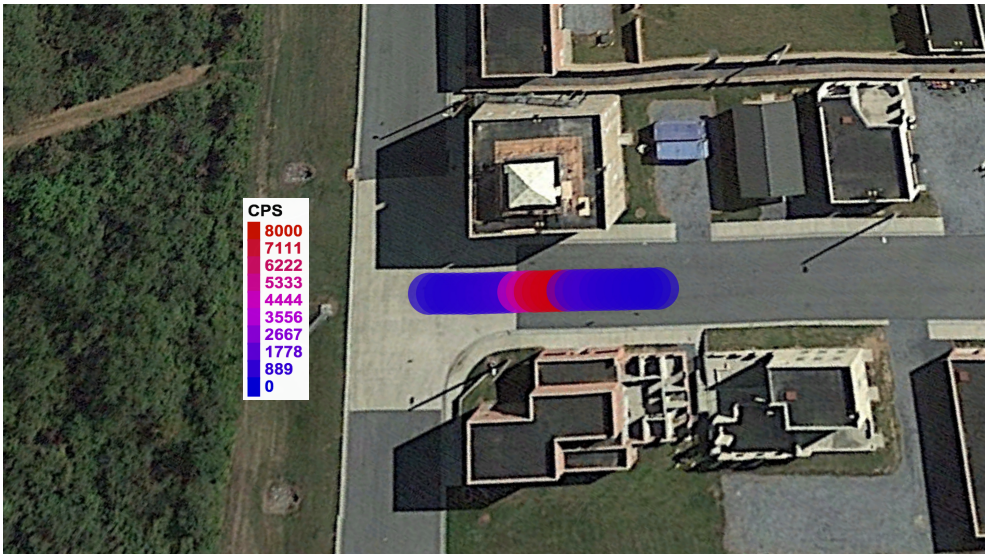
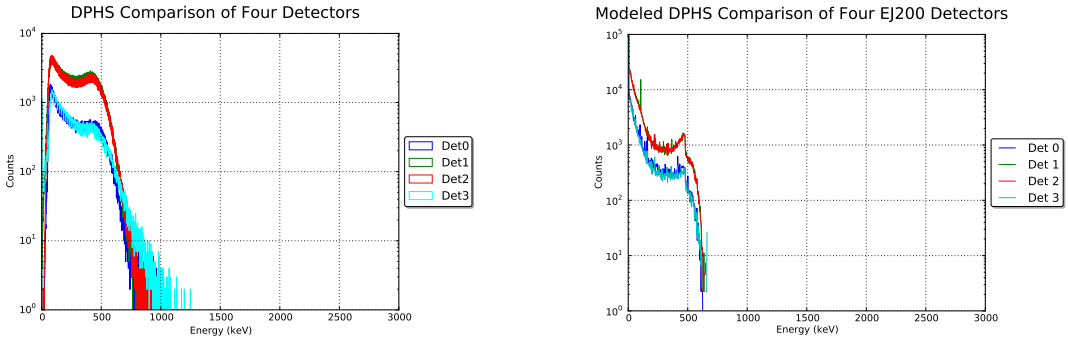


Figure 5.10: Sum of 4 - EJ200 Detector Gross Counts at Measurement Points Along Hotel Road

The goal was to create a simulation environment that provided similar results to actual measurements to perform relevant source injection studies. The results of the model and actual system at the centerline point are shown in Figure 5.11.

Comparison of the DPHS in Figure 5.11 shows that the response of the model is similar to that of reality. When comparing gross counts along the ± 28 meter area, one can see that this trend is true for nearly all points as shown in Figure 5.12.



(a) Measured DPHS from EJ200 at Centerline of Hotel

(b) Modeled DPHS from EJ200 at Centerline of Hotel

Figure 5.11: Comparison of Measured and Modeled DPHS from EJ200 Detectors at Centerline of Hotel

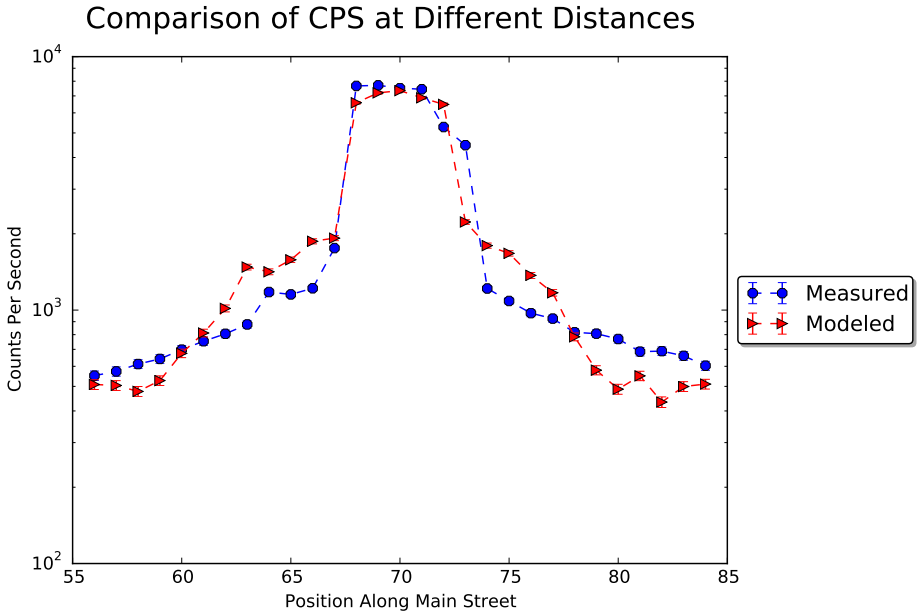


Figure 5.12: Comparison of EJ200 Sum of Gross Counts per Second for Measurement Points Along Roadway

Gross counts determined from the model were within an average of 400 counts per second from actual measurement results. Although the model did not produce the precise results from the measurements, the trend of the gross count curve was very similar.

The X-Cross system was located on the top of the cart and was comprised of four 2"x4"x16" NaI(Tl) detectors and a 2 cm lead cruciform. This system was run in parallel with the other system on the cart for the same scenario. The sum of the gross counts for this system were also compared for each location and the results were overlaid on a satellite image shown in Figure 5.13.

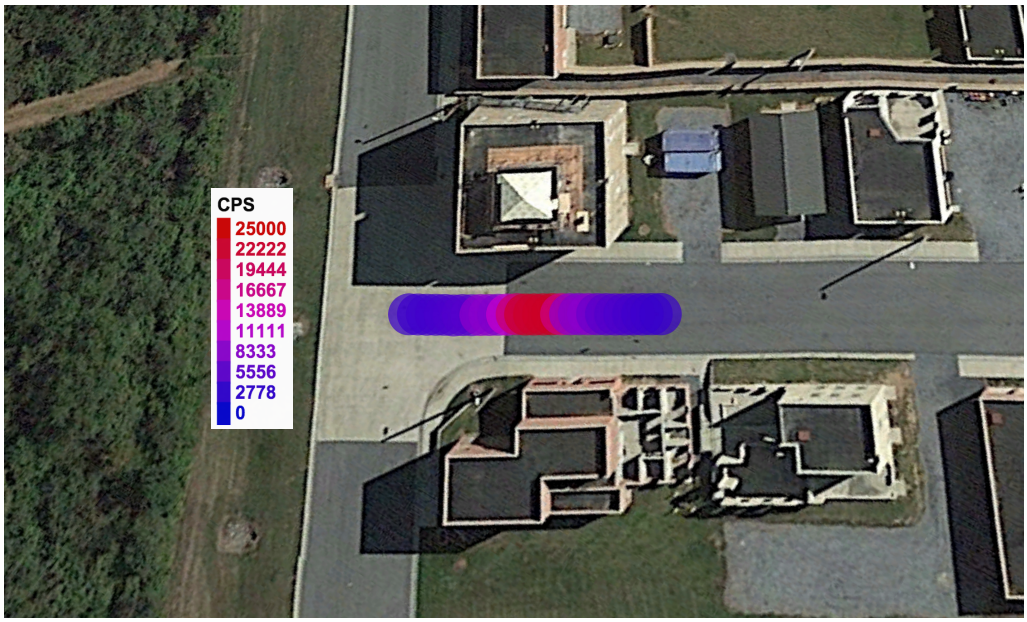
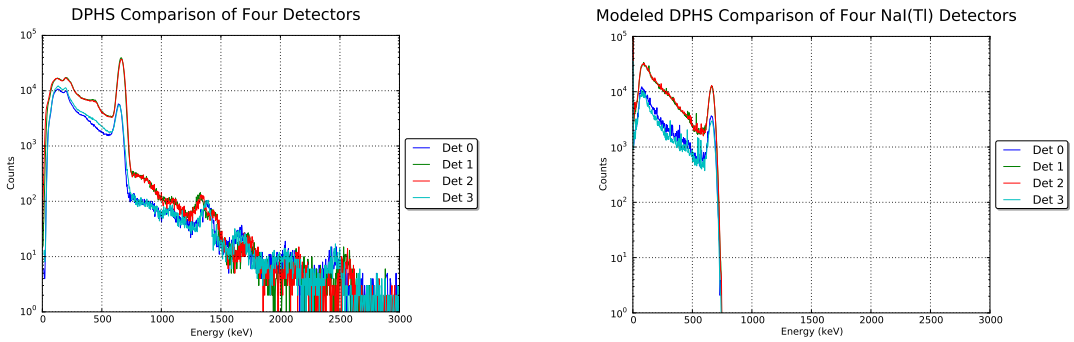


Figure 5.13: Sum of 4 - NaI(Tl) Detector Gross Counts at Measurement Points Along Hotel Road

Comparison of Figure 5.13 and Figure 5.10 shows that the number of overall counts and capability of detecting the source further from the centerline point is greater with the NaI(Tl) system than it is with the EJ200 setup. The results of the model and actual system at the centerline point are shown in Figure 5.14.

As with the EJ200 model, the NaI(Tl) model results were very similar to the measured results. The sum of gross counts from the measured and modeled results were compared in Figure 5.15.



(a) Measured DPHS from NaI(Tl) at Centerline of Hotel

(b) Modeled DPHS from NaI(Tl) at Centerline of Hotel

Figure 5.14: Comparison of of Measured and Modeled DPHS from NaI(Tl) Detectors at Centerline of Hotel

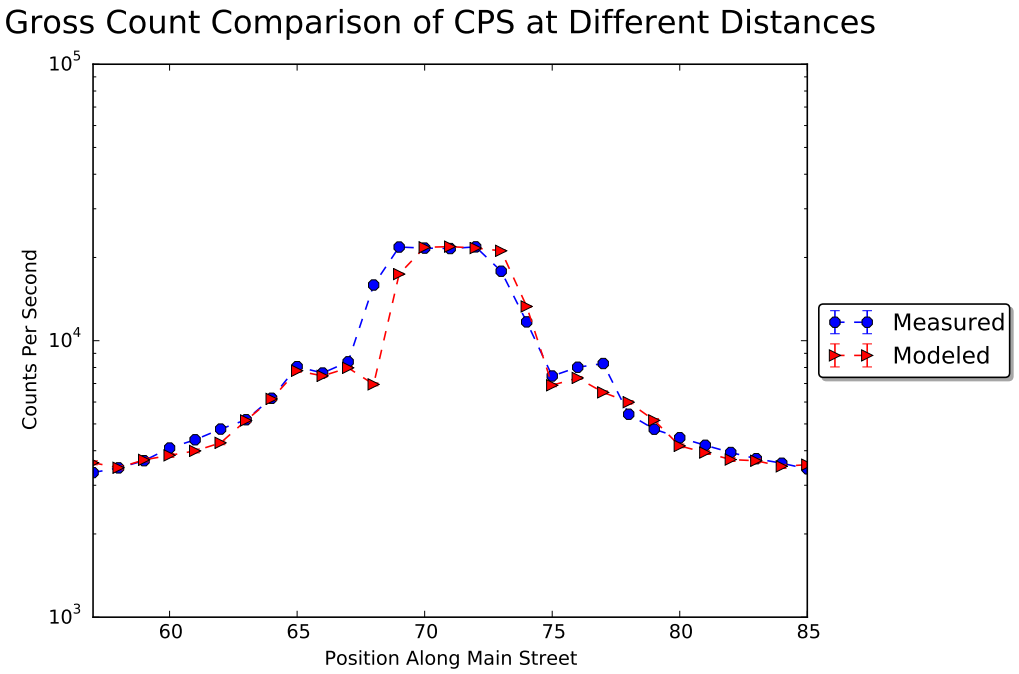


Figure 5.15: Comparison of the Sum of Gross Counts from NaI(Tl) Modeled and Measured Roadway Measurements

The comparison of the modeled and measured results for the NaI(Tl) system showed agreement slightly better than those of the EJ200. The model results were offset to the right from position 67 to 69, but aligned well for nearly every other position. Since the model was created symmetrically along the centerline of the

modeled hotel (where the source was placed), this discrepancy was attributed to aspects of the hotel not accounted for in the model such as internal walls and other attenuating objects. The centerline location of the hotel for the measured points was also an estimation, which could also skew the results ±1-2 meters.

Since NaI(Tl) has the ability to use energy resolution data on incident gamma radiation, the counts under the 662 keV energy peak associated with ^{137}Cs were compared in Figure 5.16.

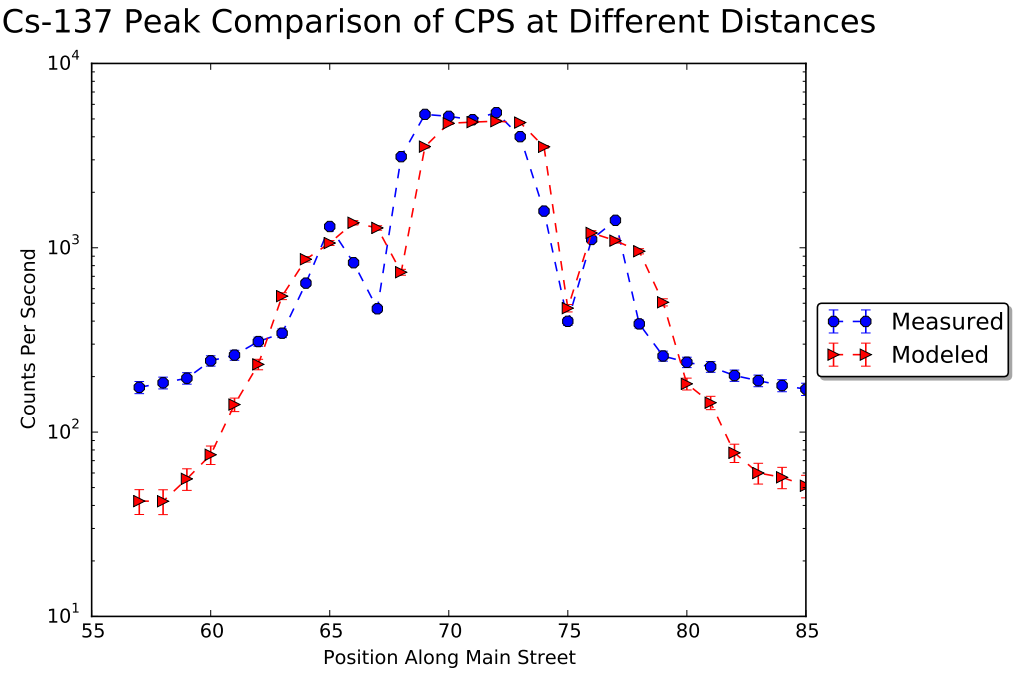


Figure 5.16: Comparison of the Counts Under 662 keV Peak from NaI(Tl) Modeled and Measured Roadway Measurements

The results from the ^{137}Cs region comparison show the two methods aligned well ±8 meters from the centerline of the hotel. Beyond this point on either side, the modeled count rate dropped below the measured values nearly an order of magnitude. This discrepancy was attributed to the influence of background sources such as ^{214}Bi (609 keV) and ^{208}Tl (583 keV) that would contribute to counts within the ^{137}Cs region. Overall, the model matches the trend of measurement count rates along the

roadway and shows the model will provide approximate results for source injection studies, especially for the centerline point ± 2 meters.

Chapter 6

System Characterization

6.1 Receiver Operating Characteristic

When searching for a radioactive source, the first thing a detection system must be capable of doing is actually detecting the presence of a source and can therefore be treated as a signal detection problem [26]. With background radiation being present nearly everywhere, a system must be capable of determining whether a source other than background is in the vicinity of the detector. There are cases, however, where the source trying to be detected is not distinguishable from background. This can cause the detection system to not detect the source above background and therefore produces a false-negative. An ideal system would be capable of detecting a source with a high probability of detection (true positive) and a false positive probability near zero. A measure of decision making performance is typically determined using a receiver operating characteristic (ROC) curve [27]. This curve compares the probability of false positives versus the probability of true positives. The curves are created using the method shown in Figures Figs. 6.1 to 6.3 [18].

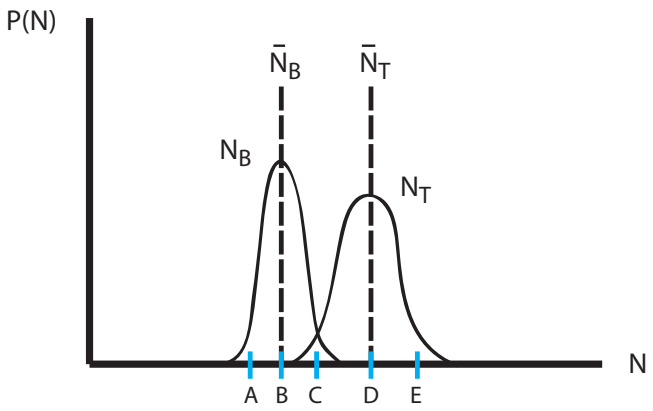


Figure 6.1: Probability Distributions for Background (N_B) and Total Counts (N_T)

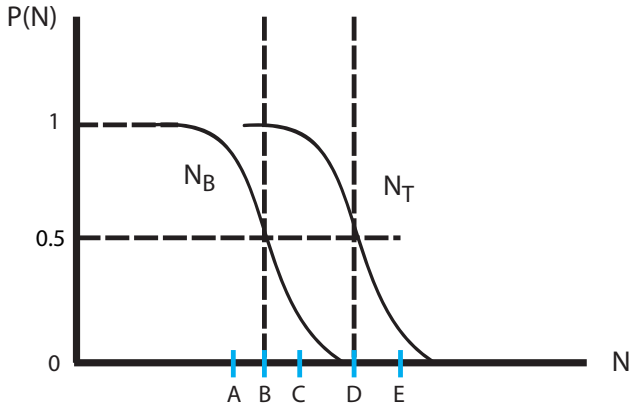


Figure 6.2: Probabilities of Observing Counts Greater than N

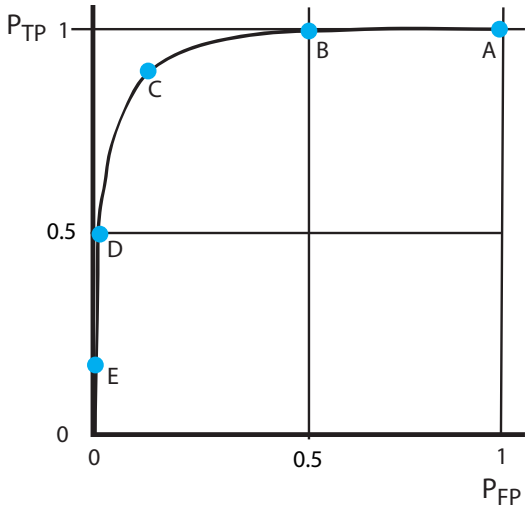


Figure 6.3: ROC Curve for Probability Distributions

A ROC curve can be used to understand the compromises between true positive and false positive probabilities [27]. This approach allows a threshold to be set above background that must be overcome in order to achieve a tolerated false positive rate that lies on the ROC curve. The area under the curve therefore corresponds to the probability of identifying whether an event is background or source plus background [28].

Utilizing background data taken from Fort Indiantown Gap measurements, ROC curves were created using source measurements from the hotel with the fuzzy logic systems. The resulting curve from the measurements at the centerline of the hotel is shown in Figure 6.4.

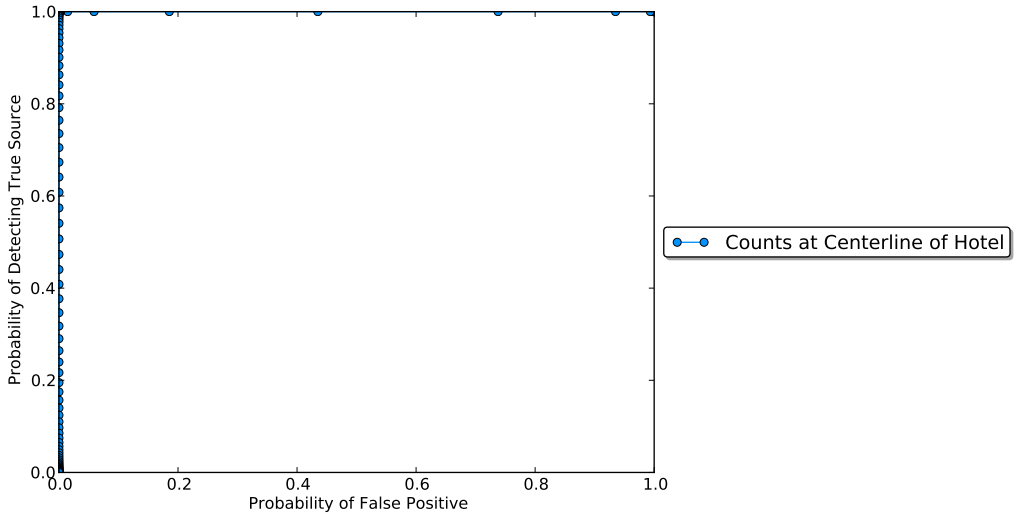


Figure 6.4: ROC Curve from Centerline Hotel Measurement with X-Cross System (All Data Points Are near Either 1 or 0 and Lie on Axes)

From Figure 6.4 it is evident that the ROC curve is an ideal scenario where the total number of counts detected was much greater than background due to the large activity of the source being used (36 mCi). Therefore the probability of a false positive would be equal to zero for the majority of the curve. This is due to the large separation of the two peaks from background and total counts detected as shown in Figure 6.5.

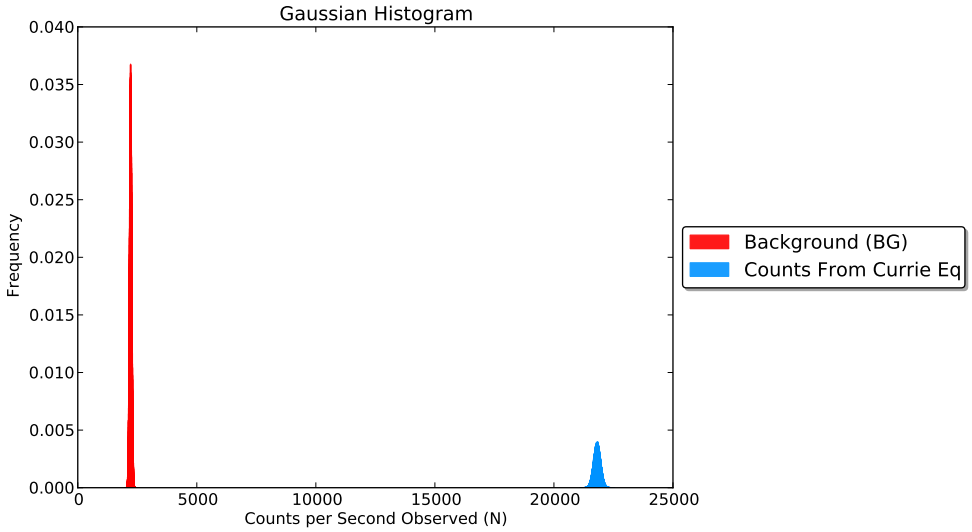


Figure 6.5: Histograms of Background and Total Counts

This large separation of the two peaks causes the integrals of probabilities of observing counts greater than "N" to also have a large separation as shown in Figure 6.6.

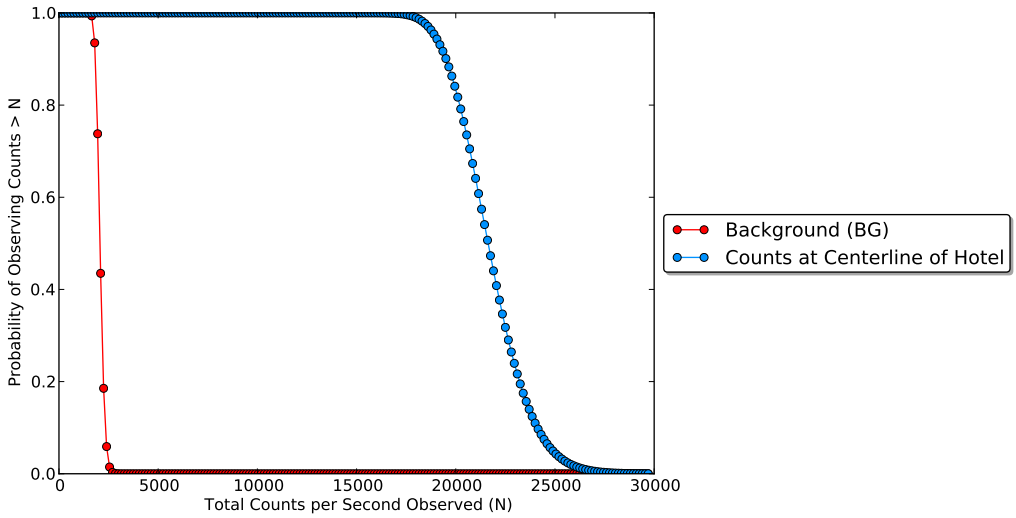


Figure 6.6: Integrals of Probabilities of Observing Counts Greater than "N"

Using the Currie equation previously discussed, another ROC curve was created to show the response of a source that would provide a false-positive rate of less than 5%. The probability histograms with the total count rate from the Currie equation and background are shown in Figure 6.7.

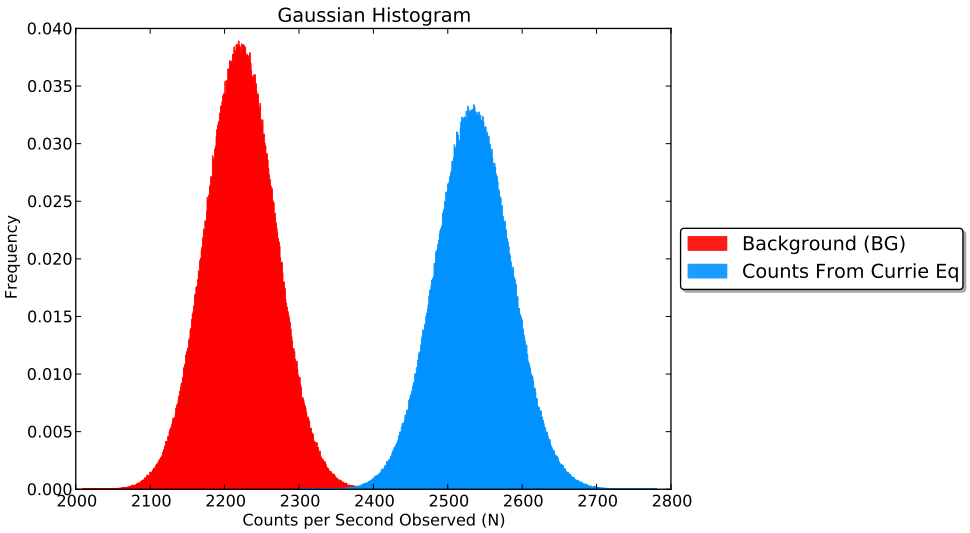


Figure 6.7: Histograms of Background and Total Counts from Currie Equation Results

Unlike the centerline measurements with the 36 mCi source, these peaks lie close to each other with a slight overlap. The integrals of probabilities of observing counts greater than "N" now have some overlap as shown in Figure 6.8.

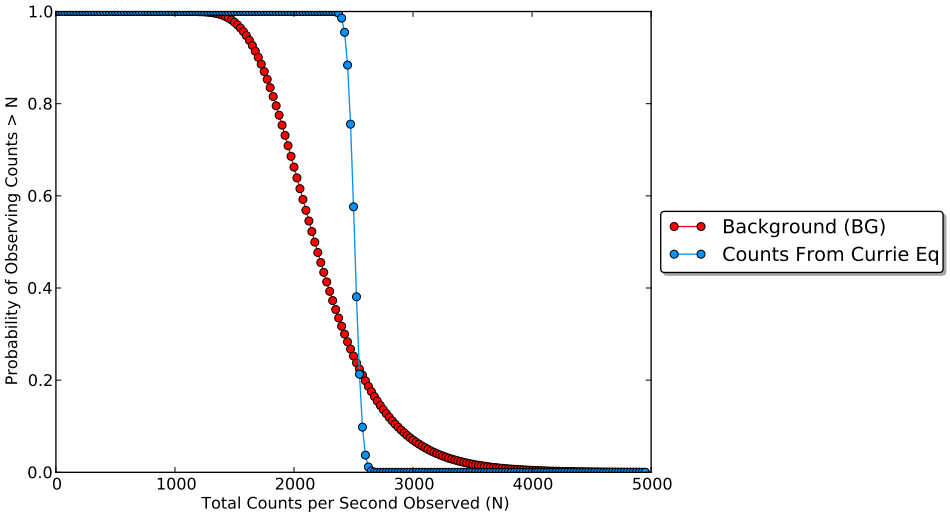


Figure 6.8: Integrals of Probabilities of Observing Counts Greater than "N" with Currie Equation Results (200 μCi ^{137}Cs)

This overlap if integrals causes the area under the ROC curve to become smaller as shown in Figure 6.9.

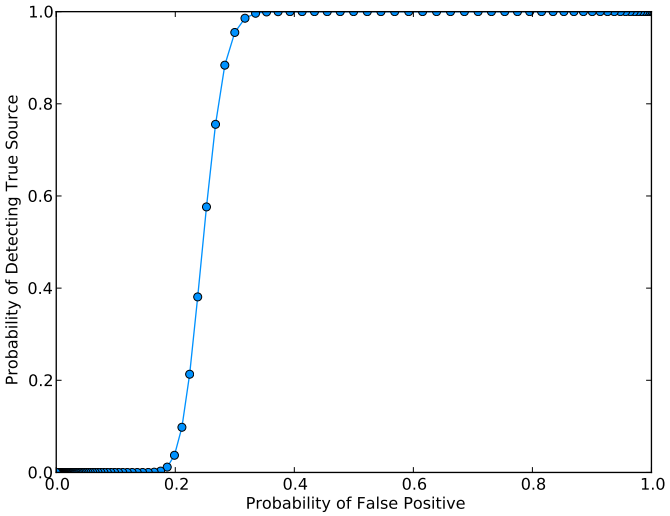


Figure 6.9: ROC Curve from Currie Equation Estimation

In comparison to the centerline measurement of the hotel, this showed that the system is capable of distinguishing between background noise and the presence of a source with much less counts than were registered in the field-measurement. To determine the system response for a range of source activities, the model of the hotel discussed previously was used to simulate a ^{137}Cs source placed at the same distance from the detector system as in the field trials. The average background of 2207 counts per second was used and ROC curves were created using source strengths ranging from 100μCi to 1000μCi at the centerline point as shown in Figure 6.10.

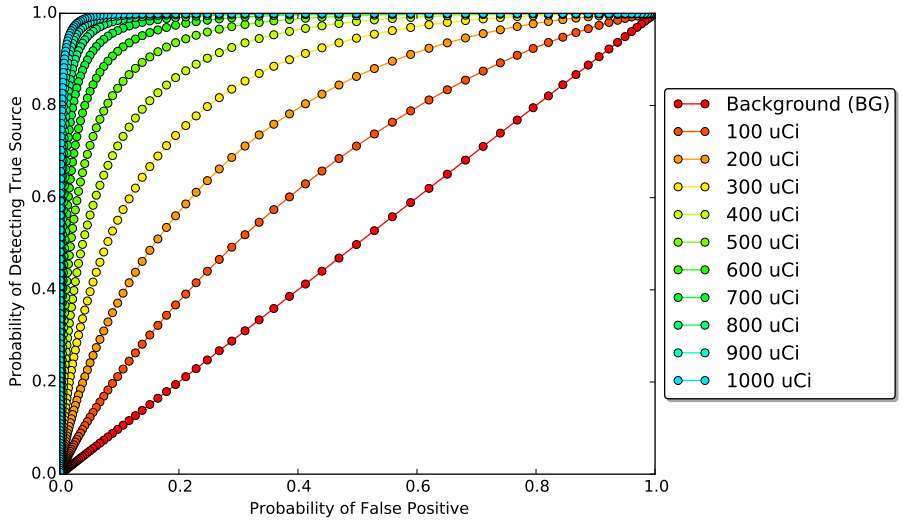


Figure 6.10: ROC Curves for Various Activities of ^{137}Cs at Centerline of Simulated Hotel

As expected, Figure 6.10 shows that as the source activity increases, the probability of detection also increases. The ROC curves also show that the probability of false alarm decreases as the source activity increases. These results show how well the system would perform with the system placed on the same centerline axis as the source. To be detectable at different locations along the road, the source strength must be increased to resolve a discernible signal above background. To determine the minimum source activity that would be detectable above background along the roadway, the Currie equation was used to determine the threshold at which the total counts must exceed (L_C). The radial distances from the source location to the measurement point along the roadway (R = 16.5-21.5 meters) were used to determine the standoff distance at which the system was placed as shown in Figure 6.11. Source activities were assessed from 100μCi to 10000μCi (10 mCi) and the calculated probabilities of detection for each distance and source activity are shown in Table 6.1

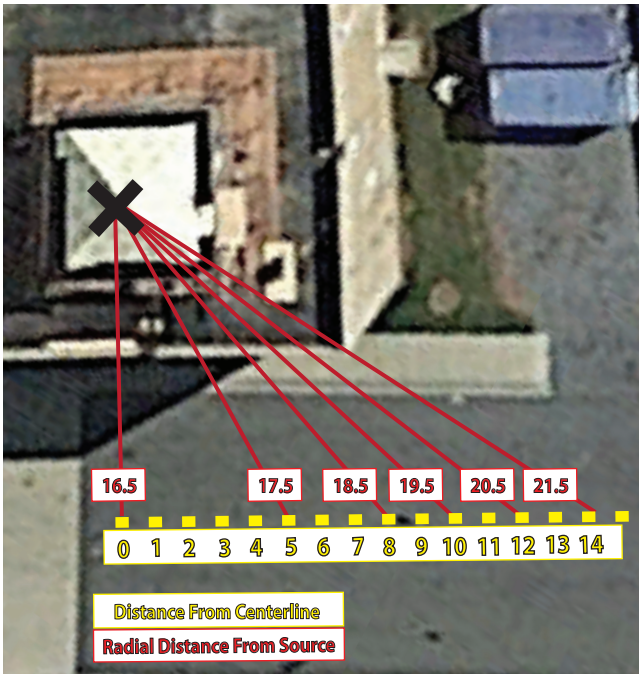


Figure 6.11: Radial Distances from Hotel Centerline in Meters

Table 6.1: Probabilities of Detection for Various Source Strengths and Distances for Simulated ^{137}Cs in Hotel

		Distance From Hotel Centerline (m)					
		0	4	7	9	11	14
Source Strength (µCi)	100	0.0611	0.0216	0	0	0	0
	200	0.999	0.9857	1E-06	0	0	0
	300	1	1	7E-06	0	0	0
	400	1	1	0.0001	0	0	0
	500	1	1	0.0015	1E-05	0	0
	1000	1	1	0.6529	0.0141	0	0
	1500	1	1	0.9999	0.4408	9E-05	1E-06
	2000	1	1	1	0.9673	0.0021	4E-05
	3000	1	1	1	1	0.1331	0.0028
	5000	1	1	1	1	0.9879	0.3392
	7500	1	1	1	1	1	0.9927
	10000	1	1	1	1	1	1

From these results, it is evident that to satisfy the Currie criteria (i.e., to resolve the signature of the source above background), there would need to be a bare 200 μCi ^{137}Cs placed in the hotel 16.5 meters away from the road. As expected, the minimum activity required to achieve a 100% probability of detection increases as the distance from the source along the roadway increases. However, there was an anomalously large increase in the required source strength between 4 and 7 meters from the centerline. This large difference was attributed to the added occlusion caused by components of the hotel geometry such as the columns and additional walls. These occluding objects affected the direct line-of-sight from the detectors to the source, causing the counts detected at the increased distances to be affected by both $1/r^2$ and the larger field-of-view at those positions. Therefore, to have a 99% probability of detection at all locations for a 1 second count, there would need to be a 7.5 mCi ^{137}Cs source present. If the source was decreased to 1.5 mCi, the probability of detection would be greater than 99% for points $\pm$7 meters from the centerline.

6.2 Algorithm Localization Performance

Once the presence of a radioactive source has been determined, the next step would be to determine the bearing of the source relative to the system and determine the location of the source. Most mobile systems that are capable of localizing a source use a coded aperture or Compton imaging techniques to localize a radiation source [29, 30, 31]. Although these techniques produce accurate results in source localization, they are also very large systems. Many of these type of systems are housed inside a box truck or trailer with the system weighing upwards of 1200 kg and 8 m^3 in size [31]. Another source localization technique uses a signal-to-noise ratio to determine the location of the source [29]. However, this technique can only determine the location of the source in one plane, meaning the system can not determine if the source lies to the left or right. The advantage of the fuzzy logic approach is the system is small enough to fit in a car-top carrier or inside a vehicle. The system also produces a

directional bearing and similarly accurate localization results as the more complex systems.

The localization capabilities of the X-cross NaI(Tl) system were analyzed using the data collected in Fort Indiantown Gap, Pennsylvania. Using the series of static measurements along the roadway in front of the hotel, a directional bearing was determined for each point. These results provide a generalized location of where the source might be, but a singular bearing alone lacks precision. In order to determine the x,y location of a source, a form of ray-tracing analysis was performed. Utilizing the directional bearings determined at each point, a vector was extended from the point for each location. The x and y locations of the ray endpoint were determined using Equations 6.1 and 6.2.

$$X' = m \cdot \cos(\theta) \tag{6.1}$$

$$Y' = m \cdot \sin(\theta) \tag{6.2}$$

Where "θ" is the directional bearing determined from the algorithm and "m" is an arbitrary value used to make the ray vectors "infinitely" large. The different vectors were then analyzed to determine where each one crossed the other as depicted in Figure 6.12.

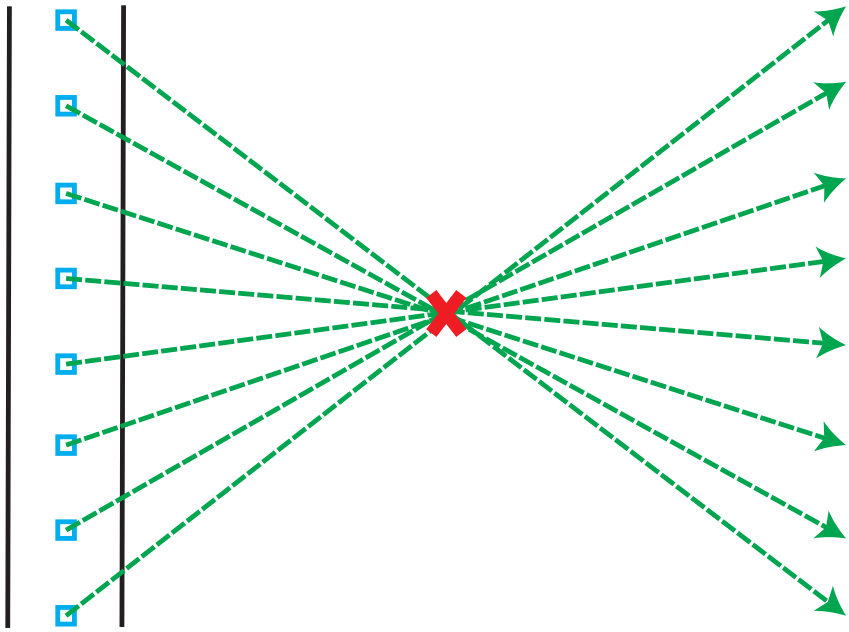


Figure 6.12: Depiction of Ray Tracing Using Directional Bearings

A two-dimensional (2D) histogram was created using the x and y values where the ray vectors intersected with one another. This histogram was laid over a satellite image of the hotel and roadway to show the location of the source in Figure 6.13.

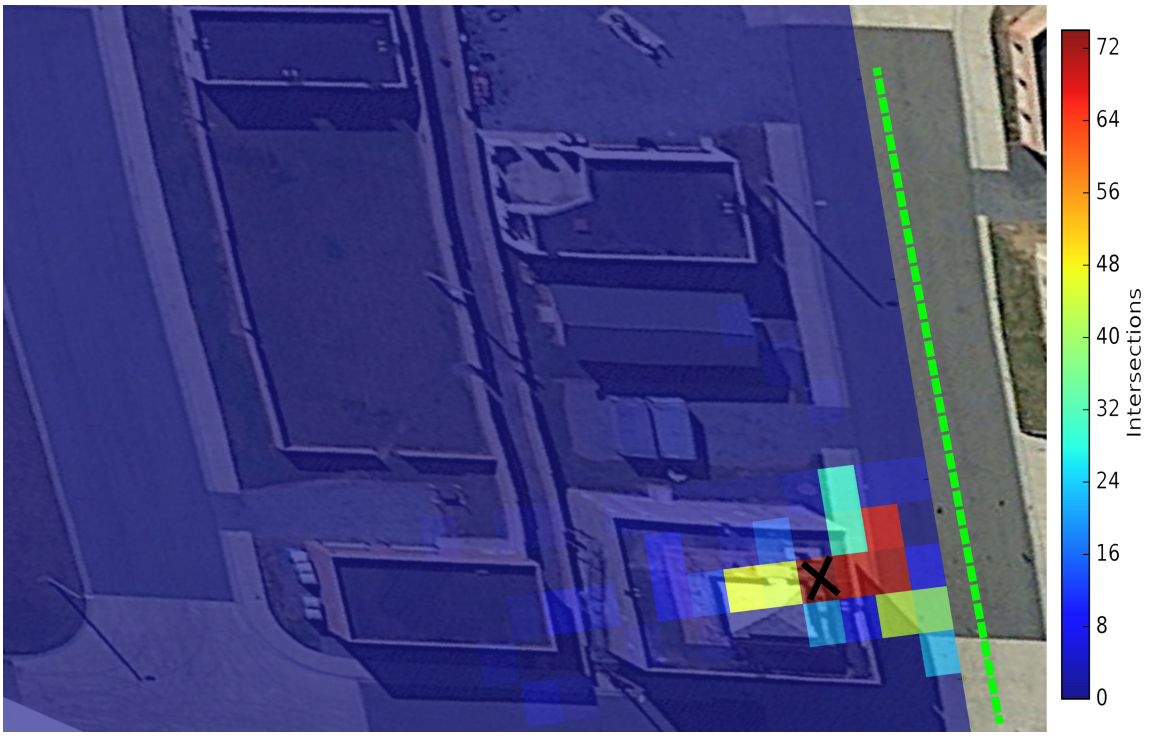


Figure 6.13: Localization Determination of a 36 mCi ^{137}Cs Source Laid over a Satellite Image

The dashed green line in Figure 6.13 shows the centerline of the where the points measurements were taken and the black "X" shows where the source was placed in the hotel. The actual location of the source was 16.5 meters from the centerline of the road. The uncertainties in the determination of the position arises from the width of the bins created in the 2D histogram. The x and y points said to equal the center of the bin and the edges of the bin determined the level of uncertainty. From the ray-tracing results, the source was determined to be located 13 meters $\pm$ 2 meters from the centerline of the roadway. If the known source location was at 0 meters on the plane parallel to the roadway, the localization determination was at 0.5 meters $\pm$ 2 meters.

To compare the performance of the fuzzy logic system's localization capabilities to other approaches, a scenario was modeled to recreate a field test performed by those systems. The simulation was created to model a 1 mCi ^{137}Cs source located

16.83 meters (10 meters from edge of modeled roadway and sidewalk) from the road. Simulations were run every 1 meter from 0 to 50 meters with the source being located at 25 meters (x-axis). The results from the simulation localization are shown in Figure 6.14.

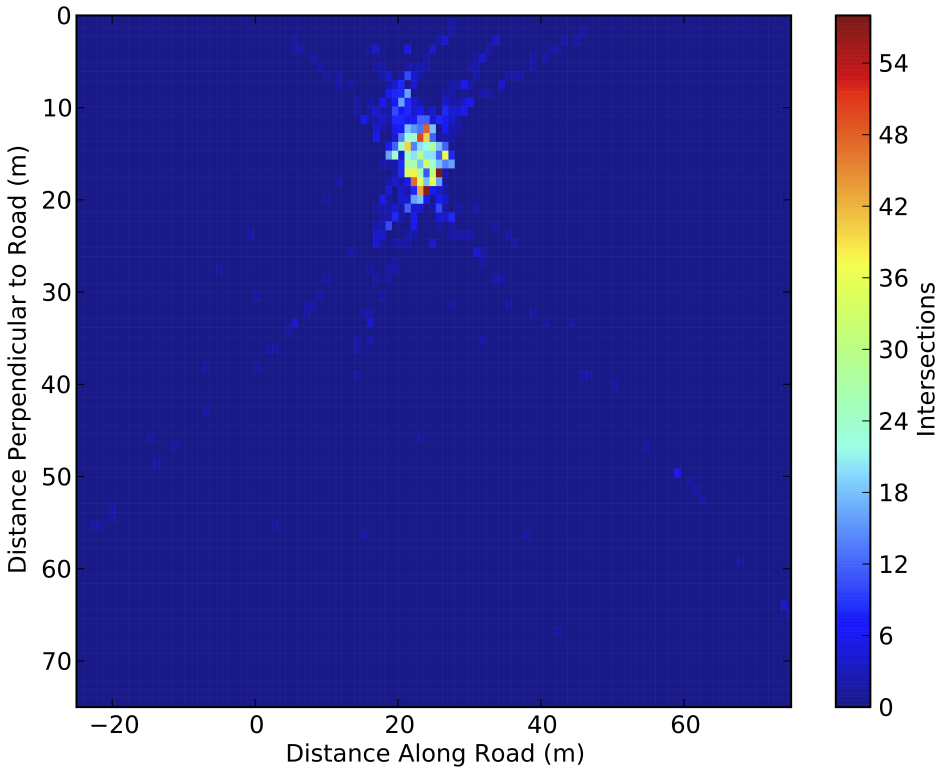


Figure 6.14: Localization Determination of a Simulated 1 mCi ^{137}Cs with Fine Bins

From Figure 6.14, it is evident that the source location can be determined, but with a large degree of uncertainty. Using this fine of a bin width, the center point of the area showing an increased number of counts was approximately 16 meters in the perpendicular direction and 23 meters in the direction of the road. Although this is close to the precise location, the area of the possible location created an uncertainty of $\pm$ 5 meters in the perpendicular direction and along the roadway. To allow more events to fall within each bin, a more coarse binning was chosen and the 2D histogram was recreated in Figure 6.15.

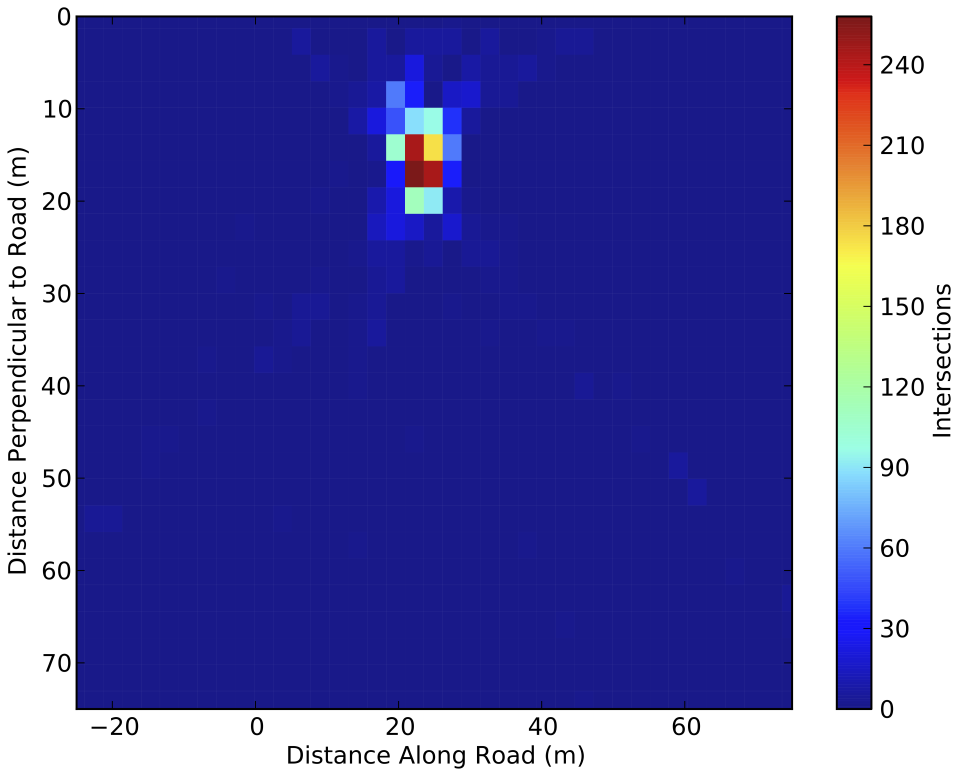
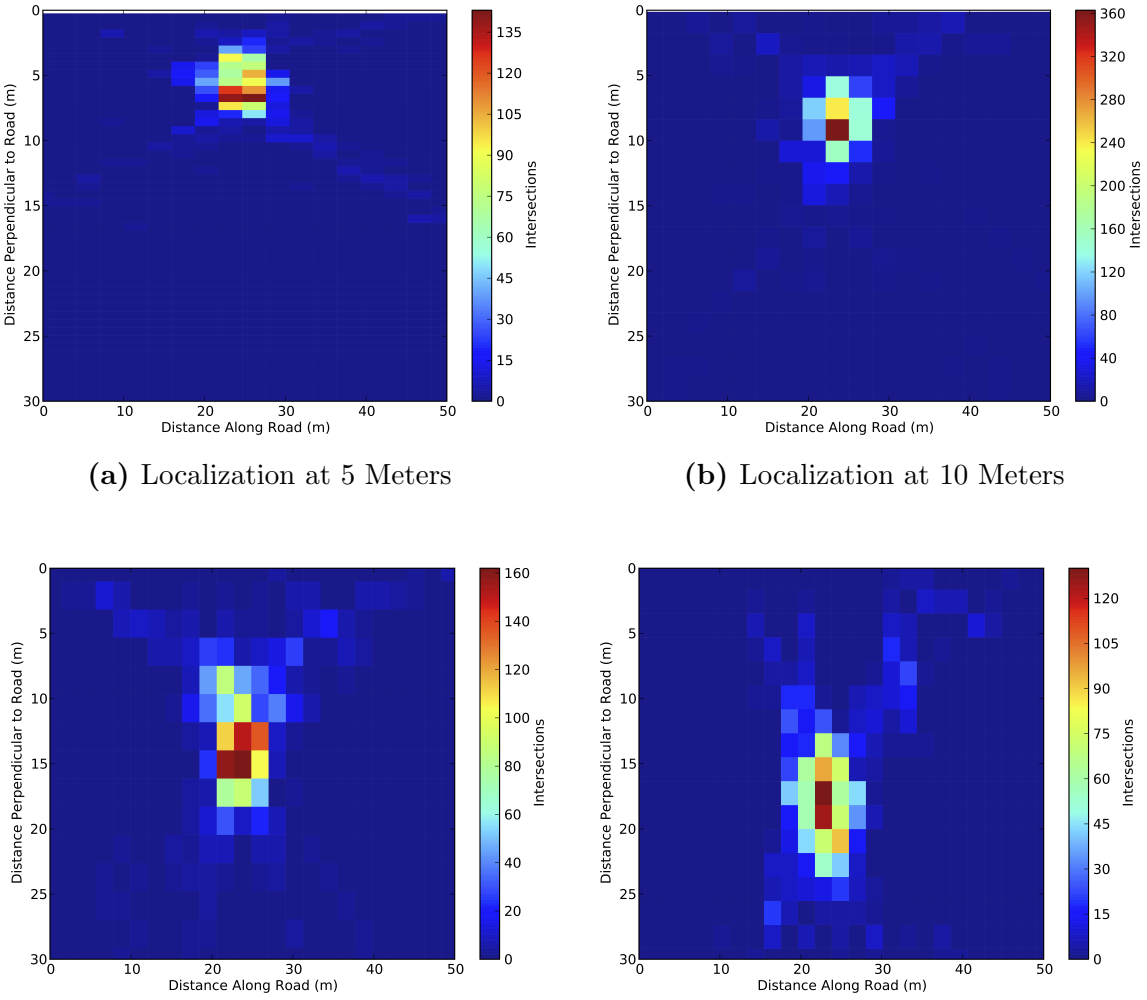


Figure 6.15: Localization Determination of a Simulated 1 mCi ^{137}Cs with Coarse Bins

This binning choice allowed for a more clear depiction of where the source location was. The source was determined to be located 15.5 ± 3 meters in the perpendicular direction and 23.5 ± 2.5 in the direction of the roadway. These results showed an offset of 1.38 meters in the perpendicular direction and 1.5 meters in the direction of the roadway. In comparison, the coded aperture system resulted in a 3 meter offset from the known in the perpendicular direction, whereas the proximity algorithm had a 5 meter offset. Both systems had an 8 meter offset in the direction of the roadway, but the operators of the systems claimed it to be caused by the GPS [29]. These systems also lacked the capability to determine which side of the roadway the source was on, whereas the fuzzy logic approach provided both the directional bearing and localization. These results show the fuzzy logic results combined with the analysis

of directional bearing vector intersections is an effective method to determine the location of a radioactive source.

Simulations were also run to characterize how well the system could localize a source placed at various distances from the roadway. The distances examined were 5, 10, 15, and 20 meters. Similar to the setup in the previous localization simulation, the source was placed 25 meters in the direction parallel to the roadway and the distance off the roadway was varied. The results from these simulations are shown in Figure 6.16



(a) Localization at 5 Meters

(b) Localization at 10 Meters

(c) Localization at 15 Meters

(d) Localization at 20 Meters

Figure 6.16: Localization Determination of a Simulated ^{137}Cs Placed at Various Distances from the Roadway

Utilizing the same approach, the localization results with associated uncertainties for each simulated location are shown in Table 6.2

Table 6.2: Localization Results with Uncertainties for Various Source Distances from Roadway

Known Source Distance (m)	**Determined Distance From Road (m)**	**Uncertainty ±(m)**	**Determined Distance Along Road (m)**	**Uncertainty ±(m)**
5	6.3	1.3	25.0	3.3
10	9.2	2.5	23.3	1.7
15	14	1.8	23.9	3.3
20	18	3.6	23.0	3.0

The probabilities for detection along the roadway were calculated for different line-of-sight distances along the roadway. The minimum distance from the source was always the centerline point and the maximum distance was ±25 m from the centerline point. Using the MCNP simulation results, the minimum and maximum Monte Carlo weights were used to simulate the various source strengths. The points for the remaining distances were chosen based on how far the source was located from the roadway. The probabilities of detection with a 1 second detection window were calculated at each position and source strength and are shown in Tables Tables 6.3 to 6.6.

Table 6.3: Probabilities of Detection for Various Source Strengths and Distances for Simulated ^{137}Cs 5m off the Roadway

		Distance From Source (m)				
		5	10	15	20	25
Source Strength (µCi)	25	0.95	0.00	0.00	0.00	0.00
	50	1.00	0.00	0.00	0.00	0.00
	100	1.00	0.00	0.00	0.00	0.00
	200	1.00	0.06	0.00	0.00	0.00
	300	1.00	0.79	0.00	0.01	0.00
	400	1.00	1.00	0.65	0.20	0.00
	500	1.00	1.00	1.00	0.70	0.04
	600	1.00	1.00	1.00	0.97	0.21
	700	1.00	1.00	1.00	1.00	0.54
	800	1.00	1.00	1.00	1.00	0.84
	900	1.00	1.00	1.00	1.00	0.97
	1000	1.00	1.00	1.00	1.00	1.00

Table 6.4: Probabilities of Detection for Various Source Strengths and Distances for Simulated ^{137}Cs 10m off the Roadway

		Distance From Source (m)				
		10	15	20	25	27
Source Strength (µCi)	25	0.00	0.00	0.00	0.00	0.00
	50	0.00	0.00	0.00	0.00	0.00
	100	0.77	0.00	0.00	0.00	0.00
	200	1.00	0.22	0.00	0.00	0.00
	300	1.00	0.97	0.00	0.00	0.00
	400	1.00	1.00	0.08	0.00	0.00
	500	1.00	1.00	0.44	0.03	0.01
	600	1.00	1.00	0.85	0.16	0.04
	700	1.00	1.00	0.99	0.44	0.17
	800	1.00	1.00	1.00	0.76	0.41
	900	1.00	1.00	1.00	0.94	0.70
	1000	1.00	1.00	1.00	0.99	0.90

Table 6.5: Probabilities of Detection for Various Source Strengths and Distances for Simulated ^{137}Cs 15m off the Roadway

		Distance From Source (m)			
		15	20	25	29
Source Strength (µCi)	25	0.00	0.00	0.00	0.00
	50	0.00	0.00	0.00	0.00
	100	0.00	0.00	0.00	0.00
	200	0.28	0.02	0.00	0.00
	300	0.99	0.55	0.01	0.00
	400	1.00	0.99	0.16	0.01
	500	1.00	1.00	0.62	0.05
	600	1.00	1.00	0.94	0.25
	700	1.00	1.00	1.00	0.60
	800	1.00	1.00	1.00	0.88
	900	1.00	1.00	1.00	0.98
	1000	1.00	1.00	1.00	1.00

Table 6.6: Probabilities of Detection for Various Source Strengths and Distances for Simulated ^{137}Cs 20m off the Roadway

		Distance From Source (m)			
		20	25	30	32
Source Strength (µCi)	25	0.00	0.00	0.00	0.00
	50	0.00	0.00	0.00	0.00
	100	0.00	0.00	0.00	0.00
	200	0.00	0.00	0.00	0.00
	300	0.11	0.02	0.00	0.00
	400	0.68	0.28	0.03	0.00
	500	0.98	0.79	0.19	0.01
	600	1.00	0.99	0.58	0.08
	700	1.00	1.00	0.90	0.28
	800	1.00	1.00	0.99	0.59
	900	1.00	1.00	1.00	0.85
	1000	1.00	1.00	1.00	0.97

The results at the centerline point were examined for each of the source distances to determine the source activity needed to achieve a 100% probability of detection

and less than 5% probability of false alarms. These results for a 1 second detection window are shown in Table 6.7.

Table 6.7: Minimum Source Activity Required at Various Distances for a 1 Second Detection Live Time

Known Source Distance (m)	**Required Source Activity μCi**
5	50
10	200
15	400
20	600

6.3 k-sigma Algorithm

As previously discussed, the Currie equation was used to determine the threshold at which the probability of a false alarm was equal to 5%. Although this is a low false alarm rate, an ideal scenario would produce less than 1 false alarm in 10,000 [32]. To set a threshold for false alarm probabilities, a different detection algorithm would need to be used. One possibility is would be the k-sigma algorithm. The k-sigma algorithm is used to compute the number of standard deviations, or k-sigma values, of the measured counts from the estimated counts from only background [33]. Equation 6.3 is used to determine the value for k.

$$k = \frac{N_{\mathrm{t}} - BG}{\sigma} \tag{6.3}$$

Where BG is the background rate, N_{t} is the total counts plus background and σ is the standard deviation of background. Using the background rate from measurements at Fort Indiantown Gap and simulation results for the hotel centerline measurements,

the probabilities of detection and false alarms were plotted against k-values in Figure 6.17.

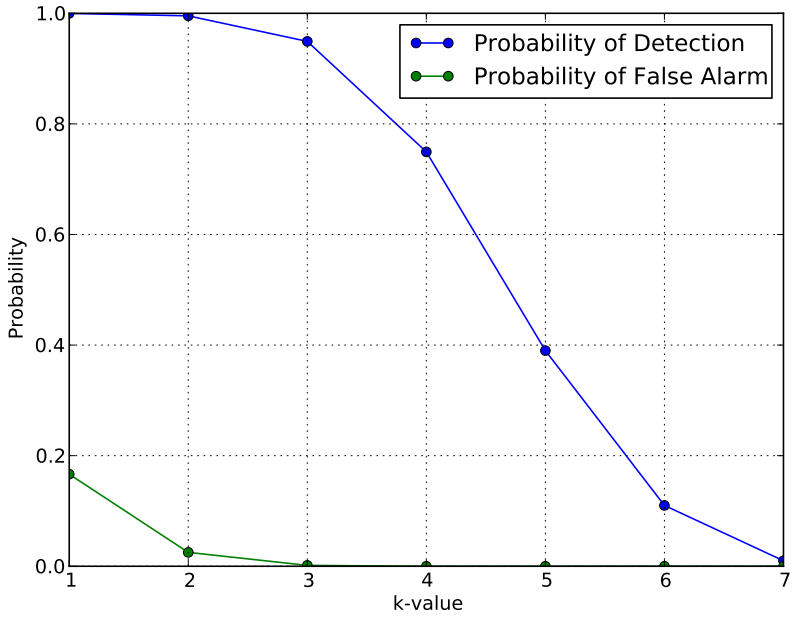


Figure 6.17: Probability of Detection and Probability of False Alarm vs k-sigma Values at Simulated Hotel Centerline

From Figure 6.17, it is evident that to achieve a probability of false alarm less than 0.0001, a k-value of 3.85 or greater needed to be chosen. Using this k-value, which provided a probability of false alarm of 0.00008, the probability of detection for various activities of a ^{137}Cs were determined. These, along with results from other k-sigma values, were plotted for the different possible activities of ^{137}Cs in Figure 6.18.

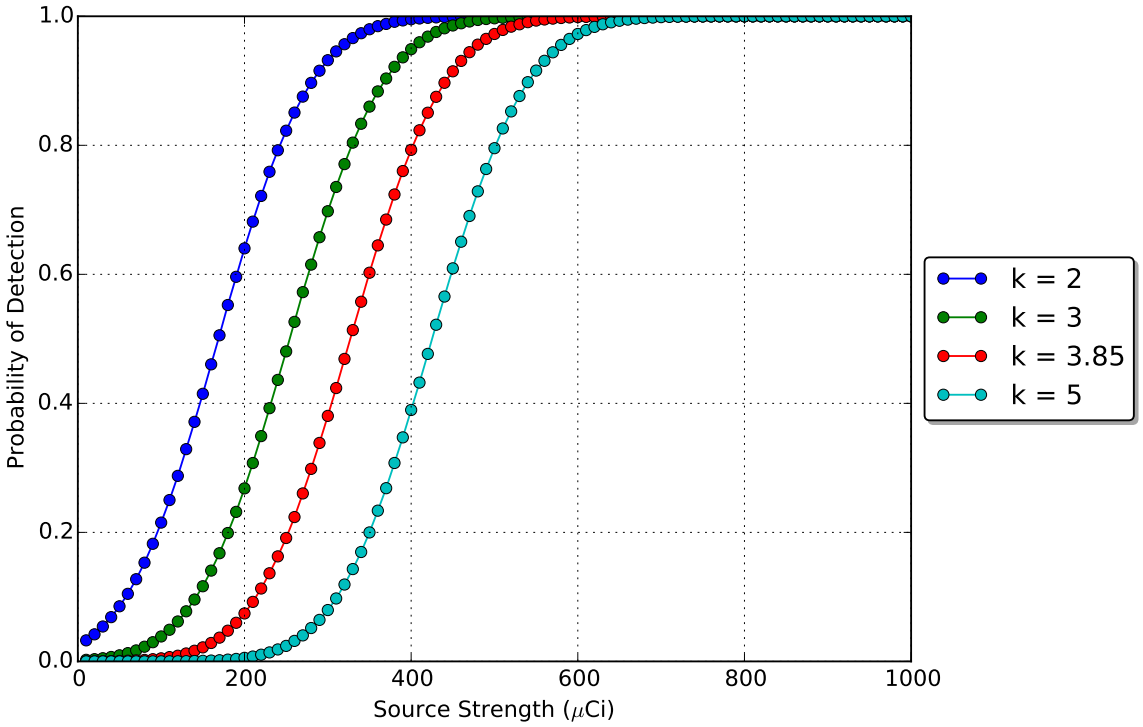


Figure 6.18: Probability of Detection vs Source Activity for Different k-sigma Values at Simulated Hotel Centerline

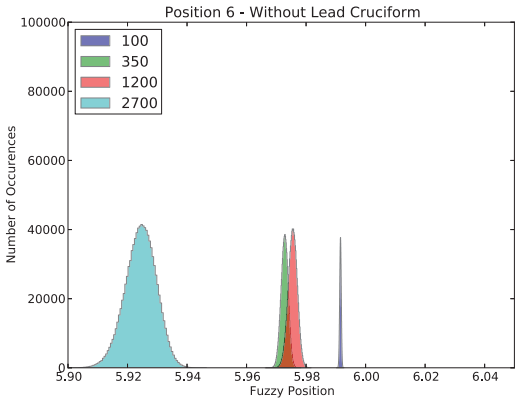
From Figure 6.18 it is evident that as the value of k-sigma increases, the probability of detection decreases if the source strength is unchanged. If the k-sigma value of 3.85 was used as the threshold level, the source activity would need to be 560 μCi in order to achieve a probability of detection greater than 99% and a false alarm probability less than 0.01%. This detection algorithm calculates a requirement for a stronger activity of source, but provides more accurate detection results. Future work should address the coupling of a detection algorithm to the real-time system with a variety of ideal k-sigma values being determined for different scenarios.

6.4 Fuzzy Logic Uncertainty

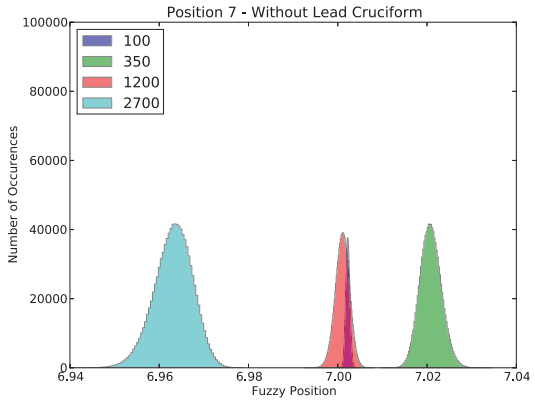
The uncertainty of the fuzzy algorithm was analyzed using MCNP data from each position along the semicircular path in the lab testing. Four energies (100, 350, 1200,

and 2700 keV) were analyzed at each position with an isotropic source emission of 200,000 particles (N), equivalent to a 5.4 μCi being detected for 1 second. This provided the detector with the highest number of counts to register between 600-900 counts. A simulated uncertainty was added to the number of counts in each detector (C_n) by generating a normally-distributed random number with mean μ=0 and variance $\sigma=\sqrt{N}$ (i.e., R$\sim$N(0,$\sqrt{N}$)). The uncertainty was added using $C_n'=C_n+R=C_n+N(0,\sigma_n)$, where C_n is the number of counts seen by detector "n" and sigma is assumed to be proportional to the number of counts observed in the detector (N). The new number C_n' calculated for each n was used to generate a new fuzzy position and thus simulate the propagated uncertainty in position by injection of random noise proportional to the expected statistical uncertainty. The uncertainty measurements for this calculations are therefore bound by (-∞, ∞), not [-σ, σ]. This process was completed 1E6 times, which allowed for normal distribution due to the large number of trials. This produced resulting fuzzy outputs for each position and an associated error around a normal distribution.

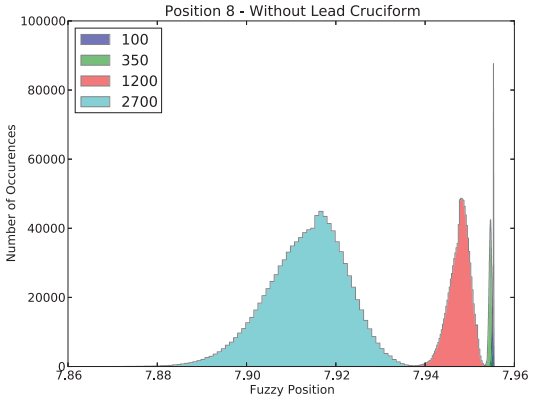
This uncertainty analysis was performed with and without the presence of the lead cruciform. The results for positions 6, 7, and 8 (135°, 157.5°, and 180°) with and without the lead cruciform are shown in Figure 6.19.



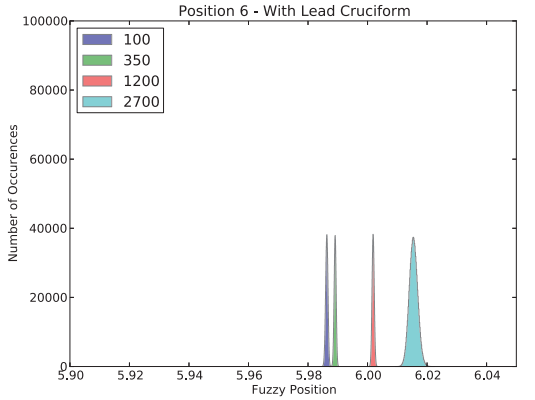
(a) Position 6 - Without Lead Cruciform



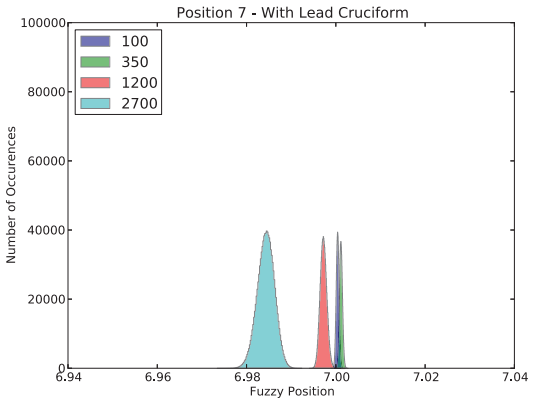
(b) Position 7 - Without Lead Cruciform



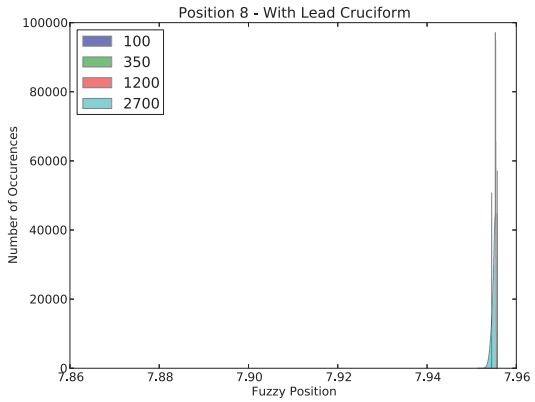
(c) Position 8 - Without Lead Cruciform



(d) Position 6 - With Lead Cruciform



(e) Position 7 - With Lead Cruciform



(f) Position 8 - With Lead Cruciform

Figure 6.19: Fuzzy Number Result and Uncertainty for Various Positions and Energies

From Figure 6.19, one can see the mean of the fuzzy position results without the lead cruciform show an uncertainty from the actual position of ≤ 0.1 (2.25°). The uncertainty of these calculations were calculated to be ≤ 0.03 from the fuzzy output mean, which is converted to $\leq 0.675°$. For each position, the uncertainty from the mean increases as the energy does, showing the largest uncertainty for the 2700 keV. The addition of the lead cruciform not only shows a more accurate calculation of the source position, but also less uncertainty in the calculated position (i.e., greater precision). The uncertainty of the calculated means from the actual positions decreased to values ≤ 0.05 (1.125°) and uncertainties of these calculations to be ≤ 0.005 (0.1125°). This shows that the addition of the lead cruciform not only helps the accuracy of the calculated position of the source, but it also decreases the uncertainty in the calculated value.

Another uncertainty analysis was performed to determine the uncertainty of the true location being anywhere within the angular region. This was accomplished by further dividing the semicircular region of the track into 32 segments, giving a possible 33 different locations located every 5.625° from 0° to 180°. Using the 2 cm lead cruciform system, MCNP trials were ran using 1E7 particles at each of the locations. The total counts rate for each detector was then input into the fuzzy logic algorithm to produce an output location. The tests demonstrated that on average, the fuzzy logic system was capable of indicating a source bearing to an accuracy of within ±3.3° of the actual source position. The minimum and maximum variations from the true values (±10.4°) occurred at positions 3.5 (78.75°) and 4.5 (101.25°).

Chapter 7

Future Work

7.1 Fuzzy Rule Transitions

As discussed in Section 3.4, there is a need for the fuzzy rule set to be modified to account for the transition between 0° and 360°. At these locations ±22.5°, the rules on either side of the transition point contribute some weight to the opposite side of the 0° origin. One possible solution to this would be to create additional rules that add more weight to the quadrant in which the position lies or create a trigonometric rule set for those positions. This solution might allow each position to be weighted as a trigonometric value that could be converted to an integer at the end. Although the error near the transition points are small, the transition still needs to be addressed.

7.2 Detection Algorithm Development

Although the fuzzy logic algorithm proved to be capable of localizing a radiation source, it needs to be coupled to a detection algorithm to limit the probability of false positives or false negatives. A detection algorithm such as the k-sigma algorithm would account for the fluctuations in background radiation as the system moves along measurement points and the counts become influenced by the presence of a radioactive source. This algorithm has the ability for the data within variable foreground and

background time integration windows to be compared to determine if a source is present. If the foreground (FG) and background (BG) time windows are too small, the probability of a false alarm is high. However, if the time windows are too large, the system becomes less sensitive to quick changes in the count rate and may decrease the probability of detection [34]. A study is required to determine the FG and BG values for optimal k-sigma values needed for the fuzzy logic system to produce a reliable probability of detection that is high and a low probability of false alarms.

Chapter 8

Conclusions

The characterization of the directional radiation detection system in this work has shown that the fuzzy logic algorithm utilized by the system is an effective tool for determining the directional bearing and position of radioactive sources. The development of the system thus far proves its capabilities as a localization technique for different detector types and geometries.

The development of the fuzzy logic rule sets showed the importance for having an accurate rule set for the different detectors and layouts. A rule set sensitivity study demonstrated the need to have rule sets that were dependent on the approximate distance from the source. However, the results showed that rule sets for ≥ 5 meters exhibited the same behavior in the detector response functions due to near-field/far-field effects. Another sensitivity study was performed to determine the effect the elevation angle of the source relative to the detectors had on the bearing determination. The study showed that at elevations up to 45°, the system was capable of determining the correct position within an average of 1° from the known angle and a maximum of $\leq 4.5^{\circ}$. Studies with the "Four-Quadrant" system showed the need for increased occlusion using a cruciform-shaped shield made of lead. This provided the occlusion needed for higher energy photons that would not be as well as occluded.

Simulation results using a 2 cm lead cruciform showed the system was capable of determining the bearing of the source within 5% of the known position.

The original "Four-Quadrant" design of the system demanded a large amount of space to house the detectors and associated electronics. An updated system was developed that not only required less space, but also had an updated interface that eliminated I/O latency and was able to provide real-time feedback. Due to non-symmetrical detector geometries, the updated system required the detector layout to be modified to accommodate 2"x4"x16" NaI(Tl) detectors. A few variations were modeled with the detectors, but the detector responses with many of the designs failed to meet the ideal detector response characteristics. The resulting layout was in the shape of an "X" and had a 2 cm cruciform placed between the detectors to further promote occlusion. Another layout was created using the NaI(Tl) detectors that allowed the determination of the elevation angle of a radioactive source. Background radiation measurements were performed at Fort Indiantown Gap, Pennsylvania, using the elevation angle setup. These measurements showed the system was capable of determining the major contributors to background radiation at a variety of measurement points. Many of the source bearings showed to be directly down (270°), but variations in the surrounding surfaces showed how some ground surfaces were more influential than others. It was determined that the largest contributor was either grass or concrete (whichever was closer) and asphalt contributed the least.

To test the system capabilities in real-world environments, a few scenarios were modeled to assess the system's directional determination performance. The first model created was a simulated parking lot. It was determined that if the detector system was placed on the top of a vehicle and a source in another vehicle's trunk, the system could determine the location of a 10 mCi ^{137}Cs source within the same row and occasionally one row over with a probability of false alarm rate less than 5%. The next scenario that was modeled was a hotel located at Fort Indiantown Gap, Pennsylvania. The simulation results were compared to the measured results along the roadway in front of the hotel and showed the model provided very similar results.

The model was therefore used to perform source injection studies to determine the minimum source activity detectable along the roadway. To achieve a $<5\%$ false positive rate, the source needed to be at least 200 μCi at the centerline and 10 mCi at a location 14 meters from the centerline. A k-sigma detection algorithm was also used to determine the minimum source required. Using a k-sigma value of 3.85, it was determined a 560 μCi source was needed to achieve a probability of detection greater than 99% and a false alarm probability less than 0.01%.

The system's capability to determine the location of the source was characterized for a few scenarios as well. The first assessment used the measured data along the roadway at Fort Indiantown Gap with a 36 mCi ^{137}Cs source. The system was able to resolve the position of the source to within 0.5 ± 2 meters along the roadway and within 3.5 ± 2 meters in the direction perpendicular to the roadway. Another scenario was modeled to simulate tests performed using other localization techniques that placed a 1 mCi ^{137}Cs source 10 meters from the roadway. These results showed an offset of 1.4 meters in the perpendicular direction and 1.5 meters in the direction of the roadway. This compared well to the other systems that were able to determine the location within 3 and 5 meters from the known location. Using a similar setup, more simulations were performed that placed the source 5, 10, 15, and 20 meters from the roadway. The fuzzy logic system was able to determine the location of the source to within <2 meters in the parallel and perpendicular directions for every distance. The minimum source activity required at each location was also determined with a 5% probability for false alarm. The results showed that for the distances of 5,10,15, and 20 meters, source strengths of 50, 200, 400, and 600 μCi were required, respectively.

Bibliography

[1] B. Geelhood, J. Ely, R. R. Hansen, R. Kouzes, J. Schweppe, and R. A. Warner, "Overview of portal monitoring at border crossings," in *Nuclear Science Symposium Conference Record, 2003 IEEE*, vol. 1, pp. 513–517 Vol.1, Oct 2003. 1

[2] D. Stromswold, J. W. Darkoch, J. Ely, R. R. Hansen, R. Kouzes, B. Milbrath, R. Runkle, W. A. Sliger, J. E. Smart, D. Stephens, L. C. Todd, and M. Woodring, "Field tests of a NaI(Tl)-based vehicle portal monitor at border crossings," in *Nuclear Science Symposium Conference Record, 2004 IEEE*, vol. 1, pp. 196–200 Vol. 1, Oct 2004. 1

[3] S.-W. Kwak, H.-S. Yoo, S. S. Jang, J. S. Kim, W.-K. Yoon, I. S. Jun, and K. H. Kim, "Plastic scintillator-based radiation detector for mobile radiation detection system against nuclear/radiological terrorism," *Nuclear Instruments and Methods in Physics Research Section A: Accelerators, Spectrometers, Detectors and Associated Equipment*, vol. 604, no. 1–2, pp. 161 – 163, 2009. {PSD8Proceedings} of the 8th International Conference on Position Sensitive Detectors. 1

[4] ORTEC, "Radiation Search Systems V2.5 NaI-SS." Available at `http://www.ortec-online.com/download/nai-ss-radiation-search-system.pdf`. 1

[5] M. J. Willis, S. E. Skutnik, and H. L. Hall, "Detection and positioning of radioactive sources using a four-detector response algorithm," *Nuclear Instruments and Methods in Physics Research A*, vol. 767, pp. 445–452, Dec. 2014. 2

[6] L. Zadeh, "Fuzzy sets," *Information and Control*, vol. 8, no. 3, pp. 338 – 353, 1965. 6

[7] B. Arfi, *Linguistic Fuzzy Logic Methods in Social Sciences*. Springer Publishing Company, Incorporated, 2014. 6

[8] L. A. Zadeh, "Fuzzy logic = computing with words," *Fuzzy Systems, IEEE Transactions on*, vol. 4, pp. 103–111, May 1996. 7

[9] H. Ishibuchi, R. Fujioka, and H. Tanaka, "Neural networks that learn from fuzzy if-then rules," *Fuzzy Systems, IEEE Transactions on*, vol. 1, pp. 85–97, May 1993. 7

[10] R. R. Yager and D. P. Filev, *Essentials of Fuzzy Modeling and Control*. New York, NY, USA: Wiley-Interscience, 1994. 10

[11] J. Saade and H. Diab, "Defuzzification techniques for fuzzy controllers," *Systems, Man, and Cybernetics, Part B: Cybernetics, IEEE Transactions on*, vol. 30, pp. 223–229, Feb 2000. 11

[12] S. Gobain, *Product Comparisons: Inorganic and Organic Scintillators*. Available at `http://www.crystals.saint-gobain.com/uploadedFiles/SG-Crystals/Documents/Technical/SGC%20Organic%20Product%20Comparisons.pdf`. 17

[13] K. M. Chandy, J. J. Bunn, and A. H. Liu, "Models and algorithms for radiation detection." 29

[14] C. L. Schrage, "Isotope identification and source directional determination using gamma radiation profiling," 2011. 30

[15] T. Aucott, M. Bandstra, V. Negut, D. Chivers, R. Cooper, and K. Vetter, "Routine Surveys for Gamma-Ray Background Characterization," *Nuclear Science, IEEE Transactions on*, vol. 60, pp. 1147–1150, April 2013. 44

[16] T. J. Aucott, M. S. Bandstra, V. Negut, J. C. Curtis, D. H. Chivers, and K. Vetter, "Effects of Background on Gamma-Ray Detection for Mobile Spectroscopy and Imaging Systems," *IEEE Transactions on Nuclear Science*, vol. 61, pp. 985–991, Apr. 2014. 44

[17] J. Duval, J. Carson, P. Holman, and A. Darnley, "Terrestrial radioactivity and gamma-ray exposure in the united states and canada: U.s. geological survey open-file report 2005-1413. available online only.," 2005. xiii, 44, 45, 46

[18] G. F. Knoll, *Radiation detection and measurement*. John Wiley & Sons, 2010. 46, 47, 72

[19] M. Bonamente, *Statistics and analysis of scientific data*. Springer, 2013. 46

[20] M. F. L'Annunziata, *Handbook of radioactivity analysis*. Academic Press, 2012. 46, 47

[21] L. A. Currie, "Limits for qualitative detection and quantitative determination. application to radiochemistry," *Analytical Chemistry*, vol. 40, no. 3, pp. 586–593, 1968. 48, 61

[22] A. Brodsky, *Accuracy and detection limits for bioassay measurements in radiation protection. Statistical considerations*. Apr 1986. 48

[23] N. C. on Radiation Protection and Measurements, "Exposure of the population in the united states and canada from natural background radiation," 1987. 56

[24] S. Fetter, V. A. Frolov, M. Miller, R. Mozley, O. F. Prilutsky, S. N. Rodionov, and R. Z. Sagdeev, "Detecting nuclear warheads," *Science & Global Security*, vol. 1, no. 3-4, pp. 225–253, 1990. 59

[25] B. USA, "Concrete Masonry Units Size and Shape Guide," 2013. 64

[26] H. Wan, T. Zhang, and Y. Zhu, "Detection and localization of hidden radioactive sources with spatial statistical method," *Annals of Operations Research*, vol. 192, no. 1, pp. 87–104, 2012. 72

[27] C. Metz, "Basic principles of roc analysis.[roc= receiver operating characteristic, a factor used in decision making regarding the optimization of diagnostic techniques]," *Semin. Nucl. Med.;(United States)*, vol. 8, no. 4, 1978. 72, 74

[28] J. A. Nevin, "Signal detection theory and operant behavior: A review of david m. green and john a. swets' signal detection theory and psychophysics. 1," *Journal of the Experimental Analysis of Behavior*, vol. 12, no. 3, pp. 475–480, 1969. 74

[29] T. J. Aucott, D. H. Chivers, and K. Vetter, "Proximity localization with the mobile imaging and spectroscopic threat identification (misti) system," in *2011 IEEE Nuclear Science Symposium Conference Record*. 81, 86

[30] S. Huh, J. Maltz, D. Gunter, L. Mihailescu, and K. Vetter, "Real-time radioactive source localization with a moving coded-aperture detector system at low count rates," in *Nuclear Science Symposium and Medical Imaging Conference (NSS/MIC), 2012 IEEE*, pp. 666–673, IEEE, 2012. 81

[31] D. Wakeford, H. Andrews, E. Clifford, L. Li, N. Bray, D. Locklin, M. V. Hynes, M. Toolin, B. Harris, J. McElroy, *et al.*, "The sords trimodal imager detector arrays," in *SPIE Defense, Security, and Sensing*, pp. 73100D–73100D, International Society for Optics and Photonics, 2009. 81

[32] I. A. E. Agency, "Detection of radioactive materials at borders," sep 2002. 91

[33] A. H. Liu, J. J. Bunn, and K. M. Chandy, "Sensor networks for the detection and tracking of radiation and other threats in cities," in *Information Processing in Sensor Networks (IPSN), 2011 10th International Conference on*, pp. 1–12, IEEE, 2011. 91

[34] D. E. Archer, D. E. Hornback, J. O. Johnson, T. M. Miller, A. D. Nicholson, B. W. Patton, D. E. Peplow, and B. Ayaz-Maierhafer, "Systematic assessment of neutron & gamma backgrounds relevant to operational modeling and detection technology implementation, ornl/ltr-2014/687," December 2014. 98

Appendix

Appendix A

Elevation Angle Results

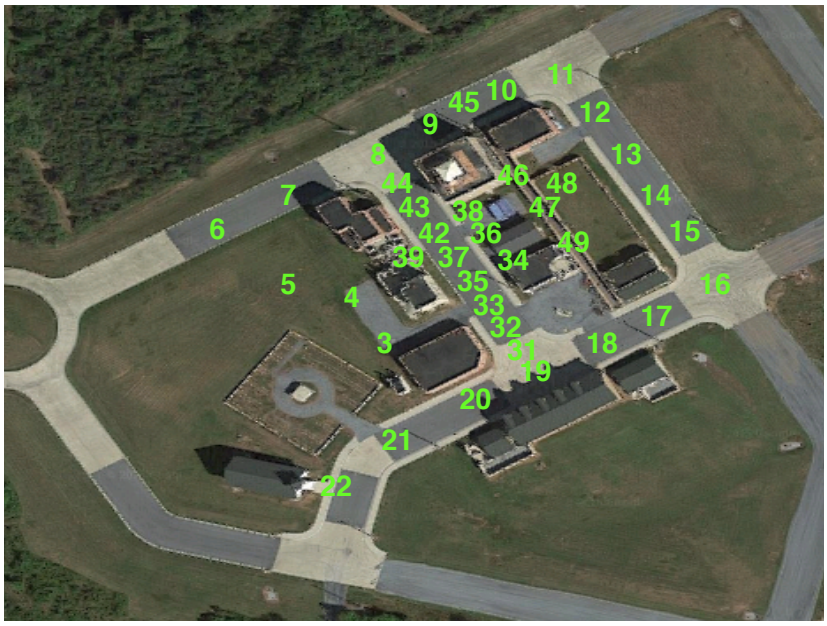


Figure A.1: Background Measurement Points at Fort Indiantown Gap, Pennsylvania

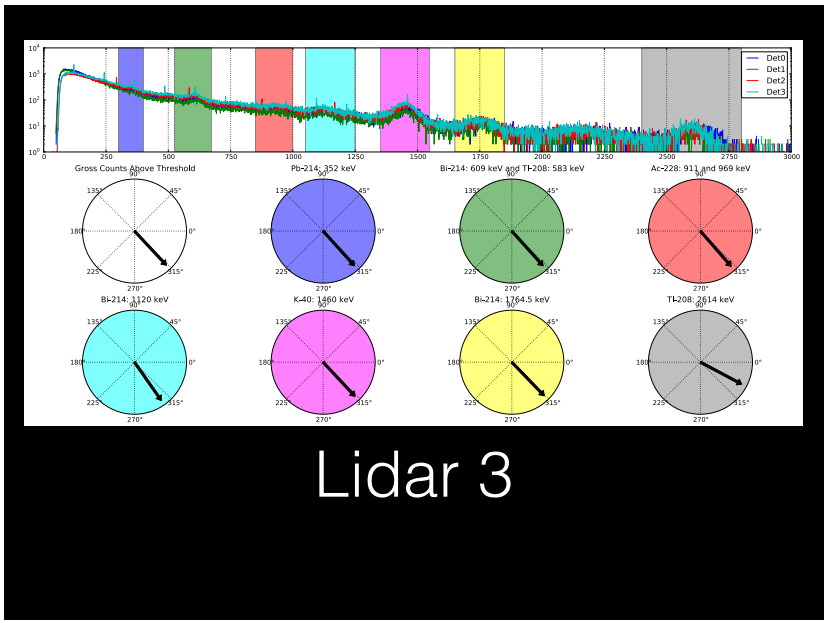


Figure A.2: Elevation Angle Results for Measurement Point 3 at Fort Indiantown Gap, Pennsylvania

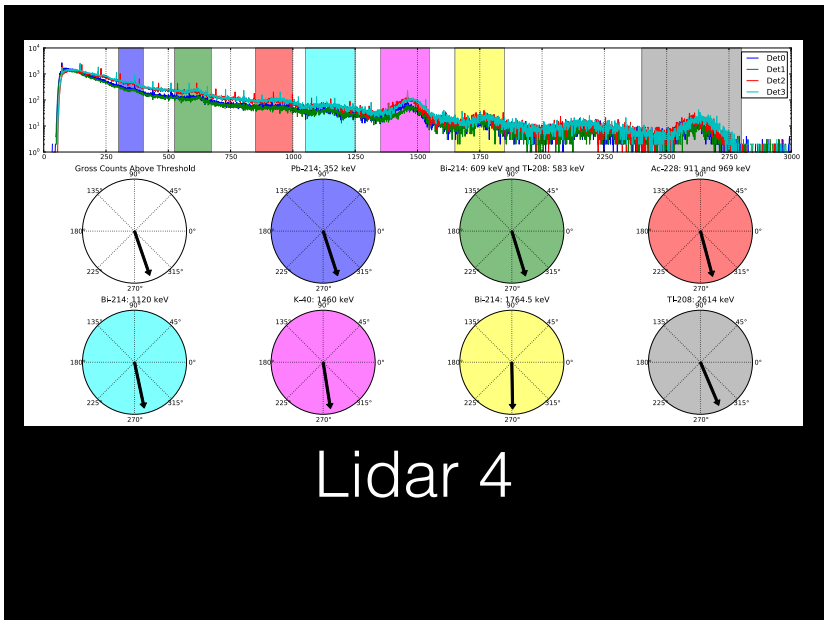


Figure A.3: Elevation Angle Results for Measurement Point 4 at Fort Indiantown Gap, Pennsylvania

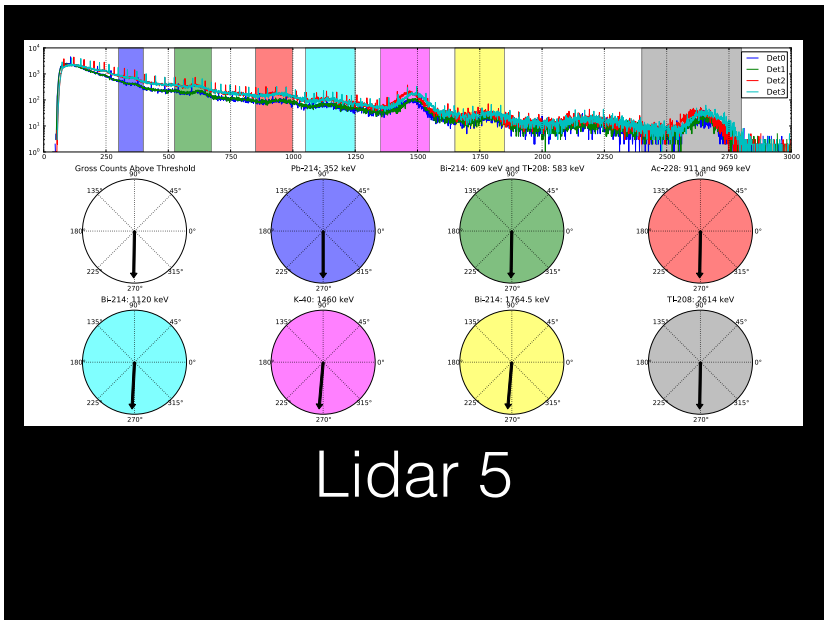


Figure A.4: Elevation Angle Results for Measurement Point 5 at Fort Indiantown Gap, Pennsylvania

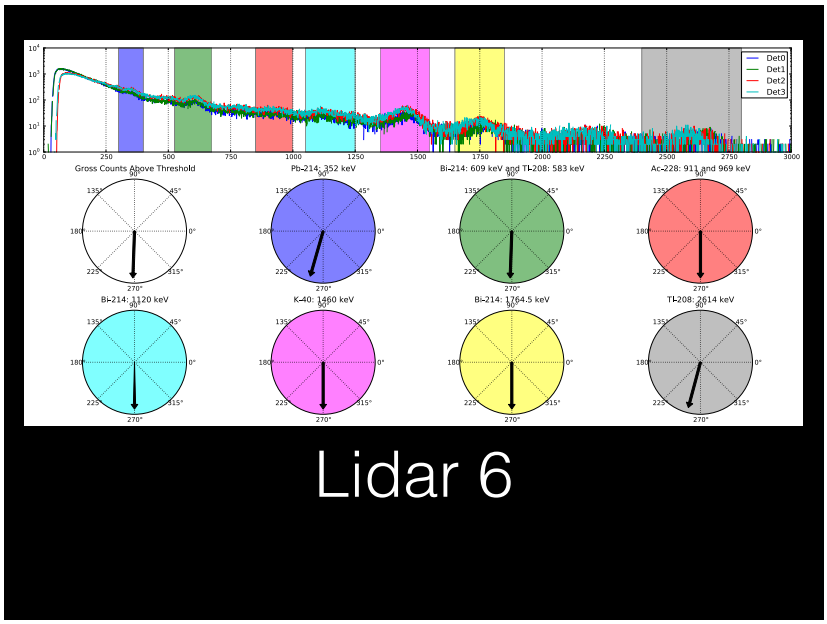


Figure A.5: Elevation Angle Results for Measurement Point 6 at Fort Indiantown Gap, Pennsylvania

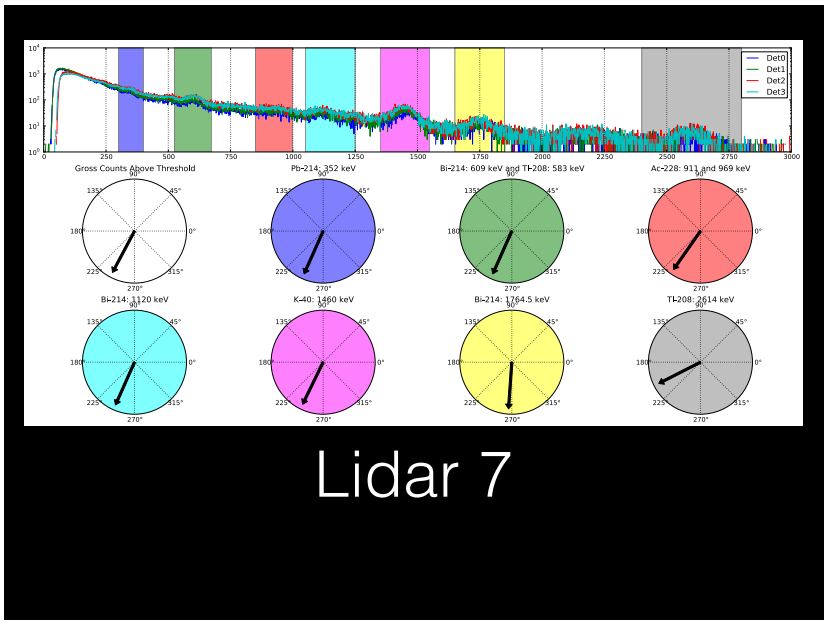


Figure A.6: Elevation Angle Results for Measurement Point 7 at Fort Indiantown Gap, Pennsylvania

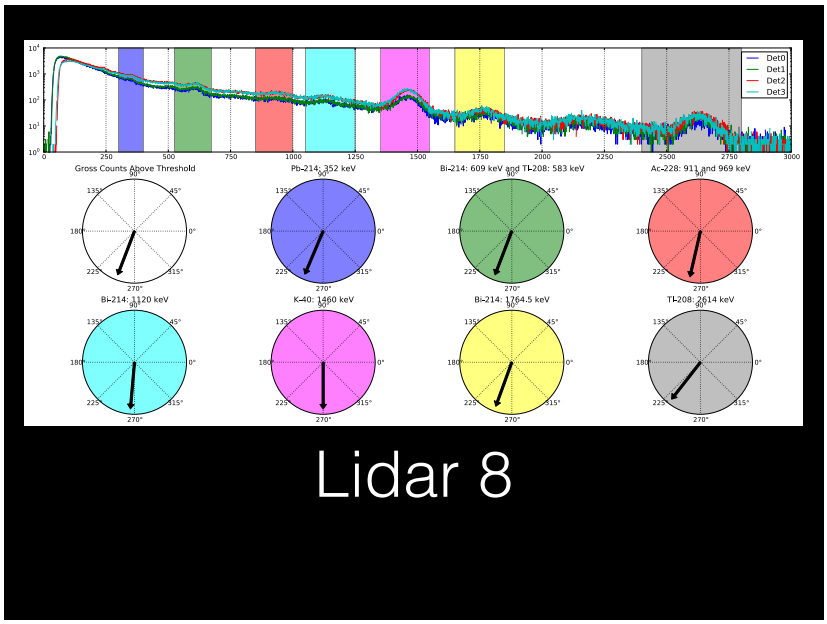


Figure A.7: Elevation Angle Results for Measurement Point 8 at Fort Indiantown Gap, Pennsylvania

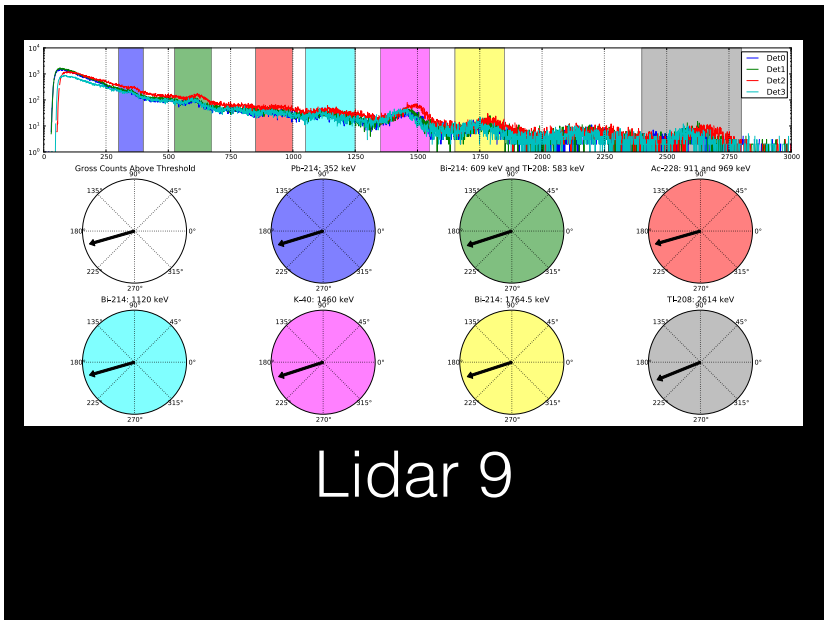


Figure A.8: Elevation Angle Results for Measurement Point 9 at Fort Indiantown Gap, Pennsylvania

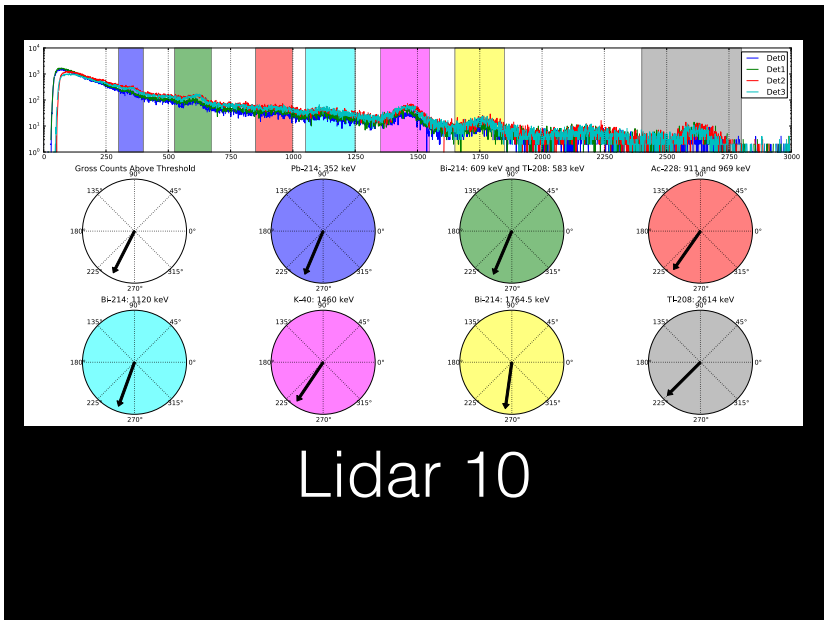


Figure A.9: Elevation Angle Results for Measurement Point 10 at Fort Indiantown Gap, Pennsylvania

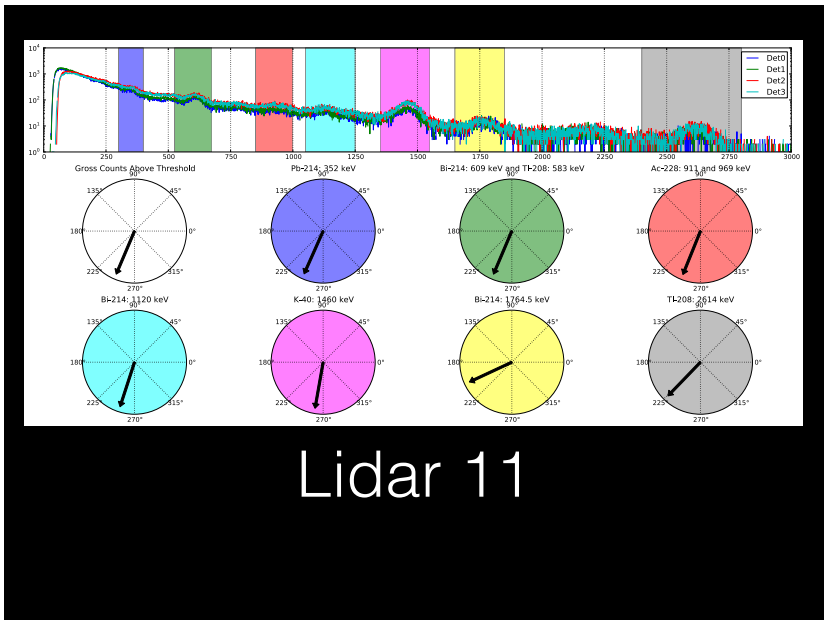


Figure A.10: Elevation Angle Results for Measurement Point 11 at Fort Indiantown Gap, Pennsylvania

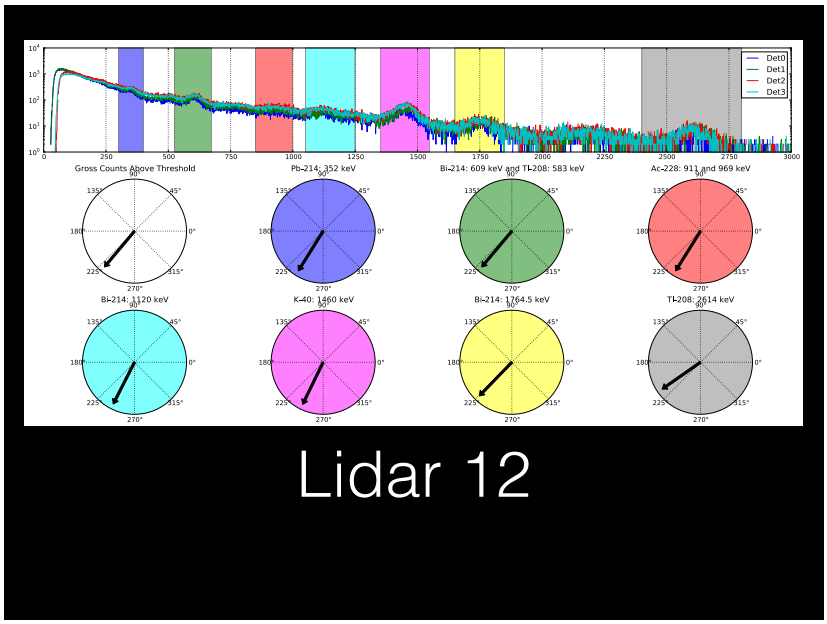


Figure A.11: Elevation Angle Results for Measurement Point 12 at Fort Indiantown Gap, Pennsylvania

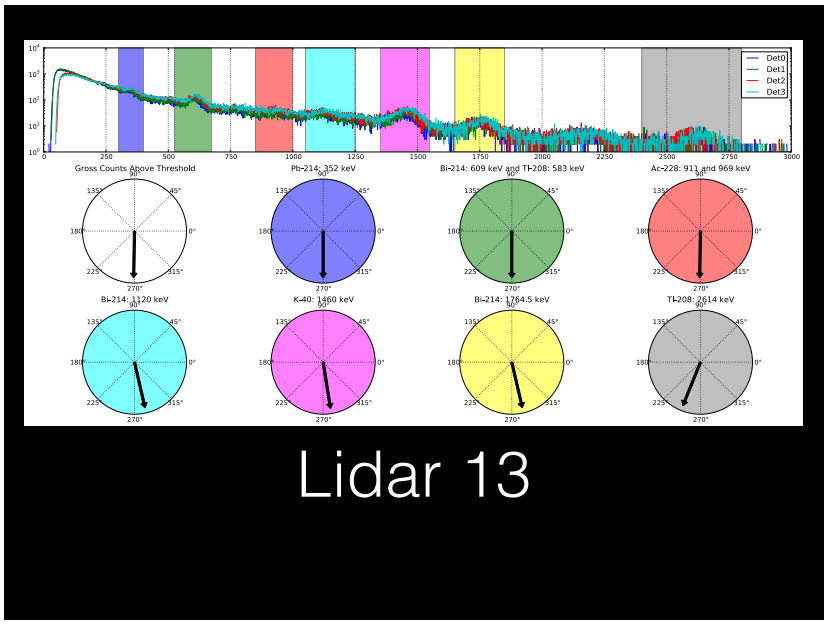


Figure A.12: Elevation Angle Results for Measurement Point 13 at Fort Indiantown Gap, Pennsylvania

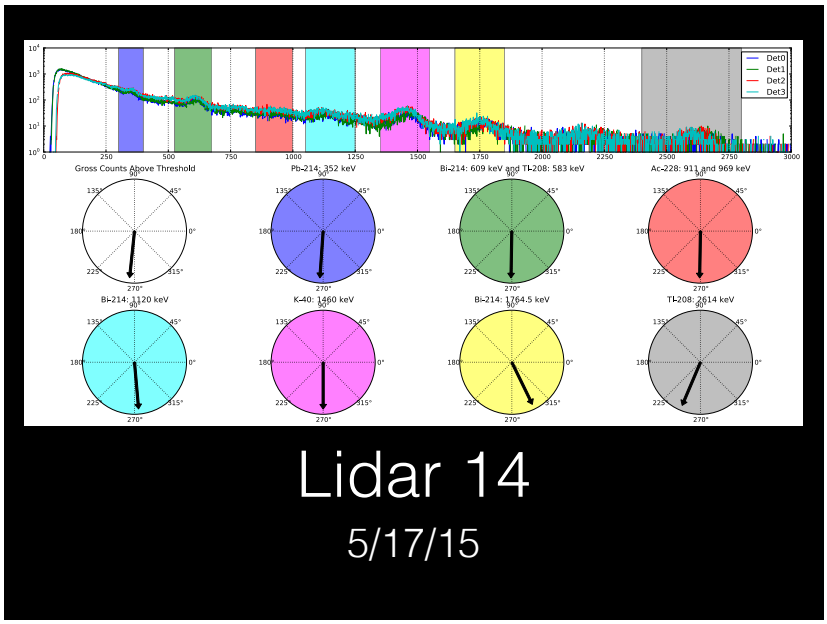


Figure A.13: Elevation Angle Results for Measurement Point 14 (05/17/15) at Fort Indiantown Gap, Pennsylvania

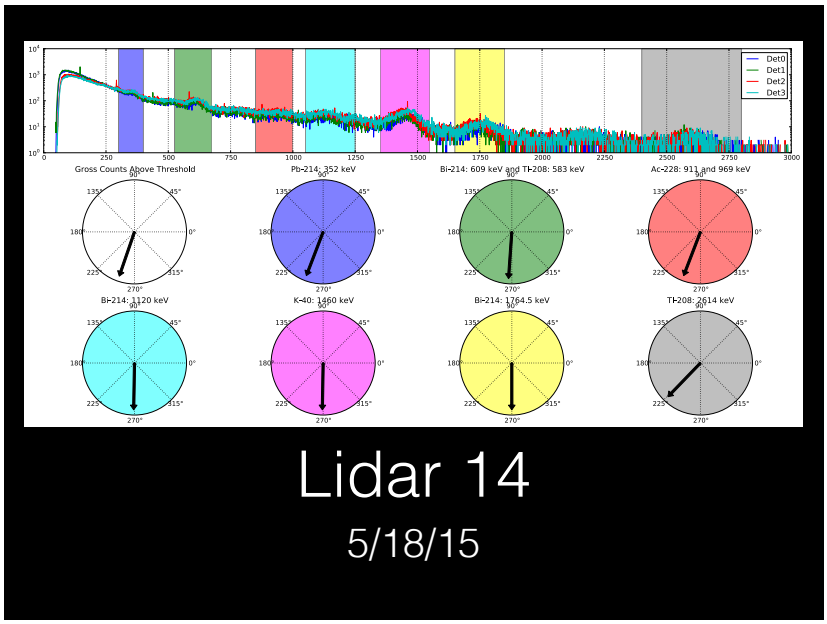


Figure A.14: Elevation Angle Results for Measurement Point 14 (05/18/15) at Fort Indiantown Gap, Pennsylvania

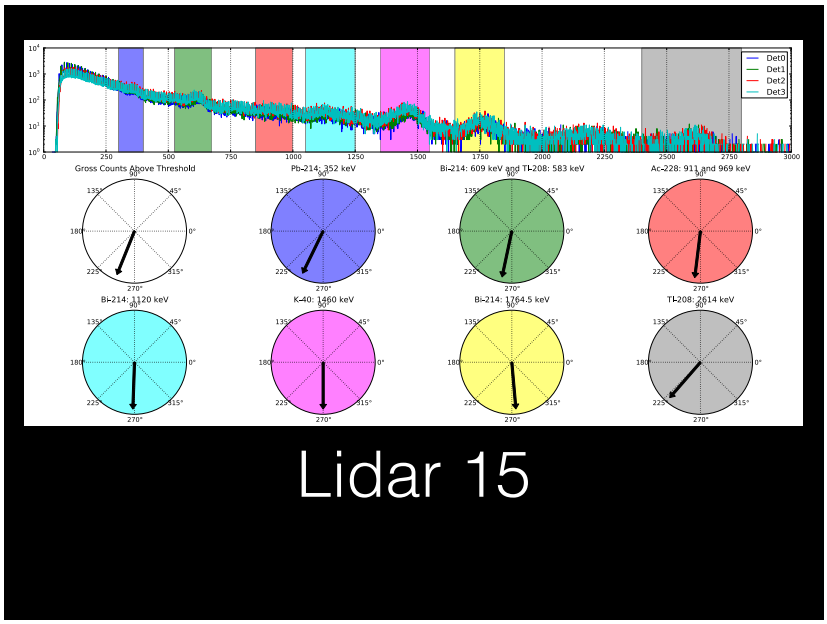


Figure A.15: Elevation Angle Results for Measurement Point 15 at Fort Indiantown Gap, Pennsylvania

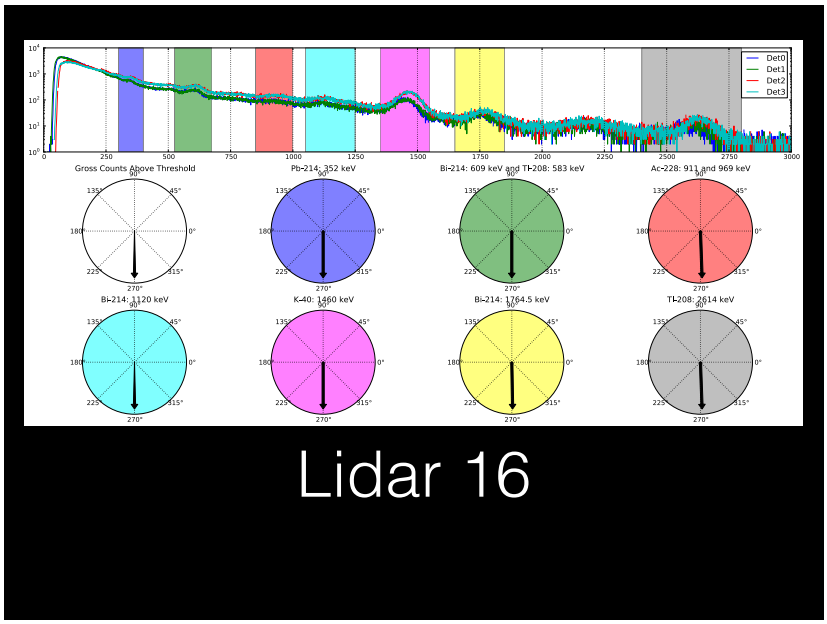


Figure A.16: Elevation Angle Results for Measurement Point 16 at Fort Indiantown Gap, Pennsylvania

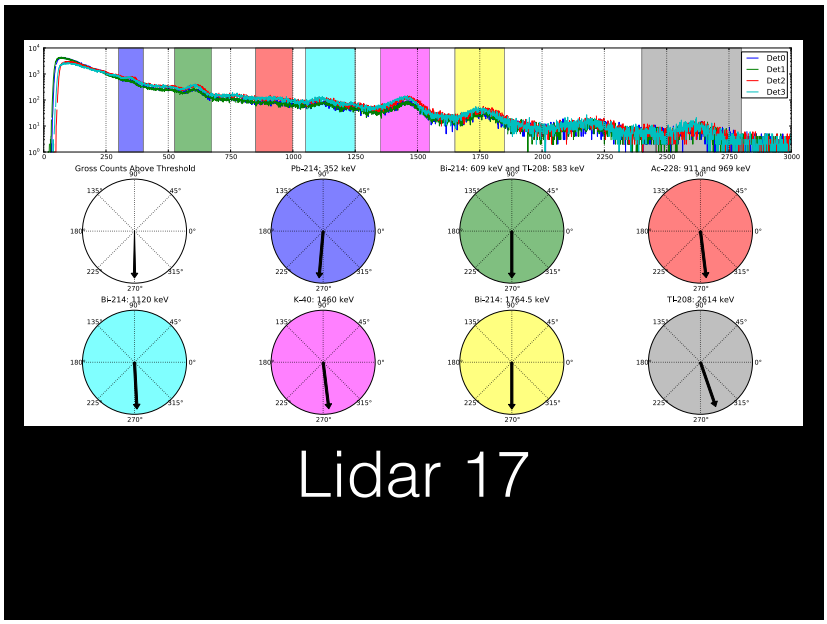


Figure A.17: Elevation Angle Results for Measurement Point 17 at Fort Indiantown Gap, Pennsylvania

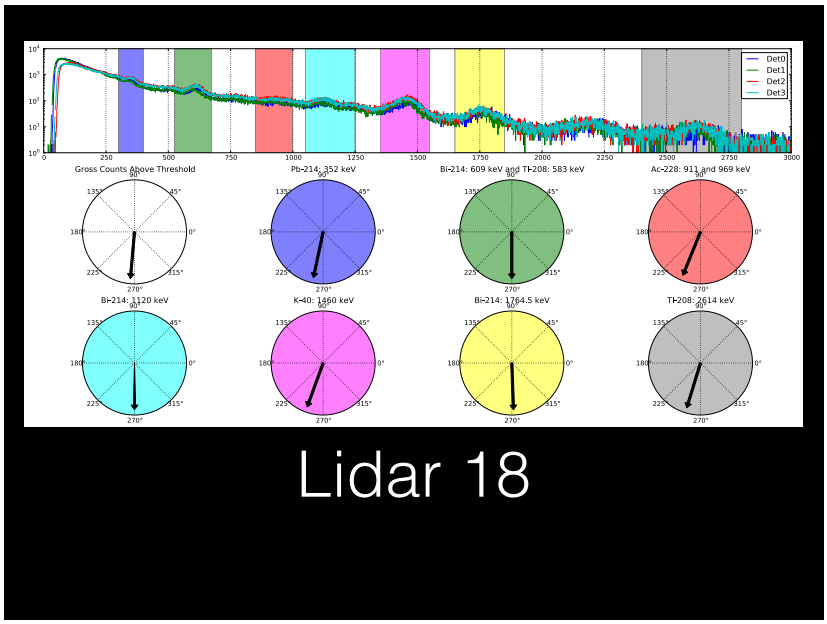


Figure A.18: Elevation Angle Results for Measurement Point 18 at Fort Indiantown Gap, Pennsylvania

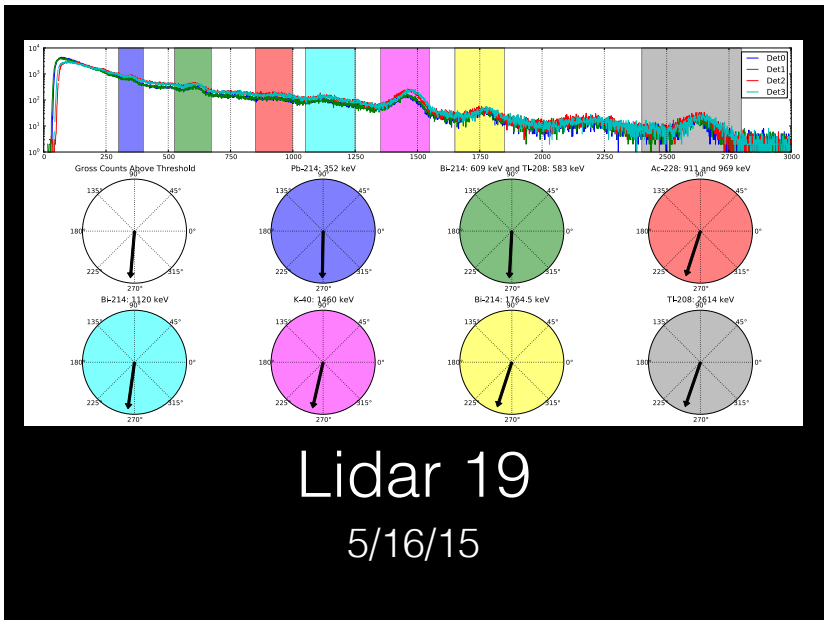


Figure A.19: Elevation Angle Results for Measurement Point 19 (05/16/15) at Fort Indiantown Gap, Pennsylvania

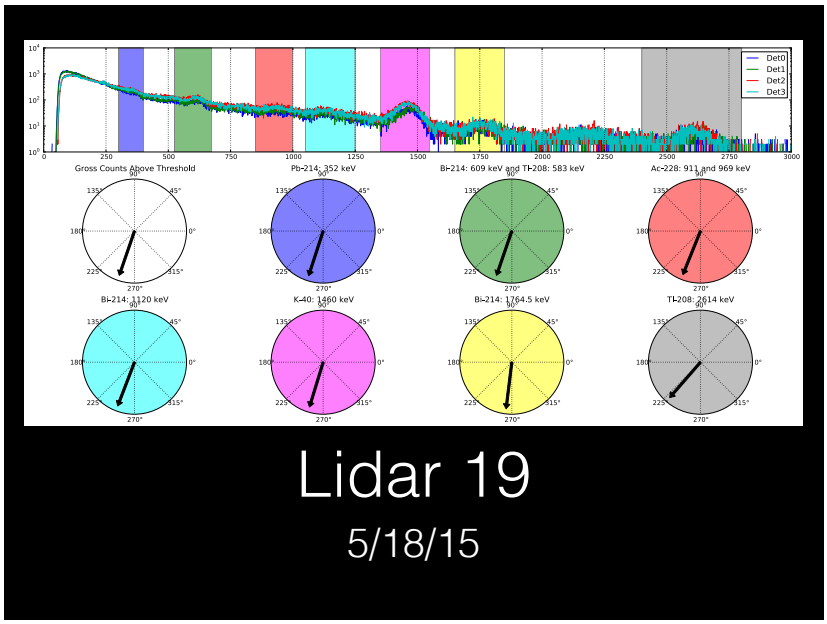


Figure A.20: Elevation Angle Results for Measurement Point 19 (05/18/15) at Fort Indiantown Gap, Pennsylvania

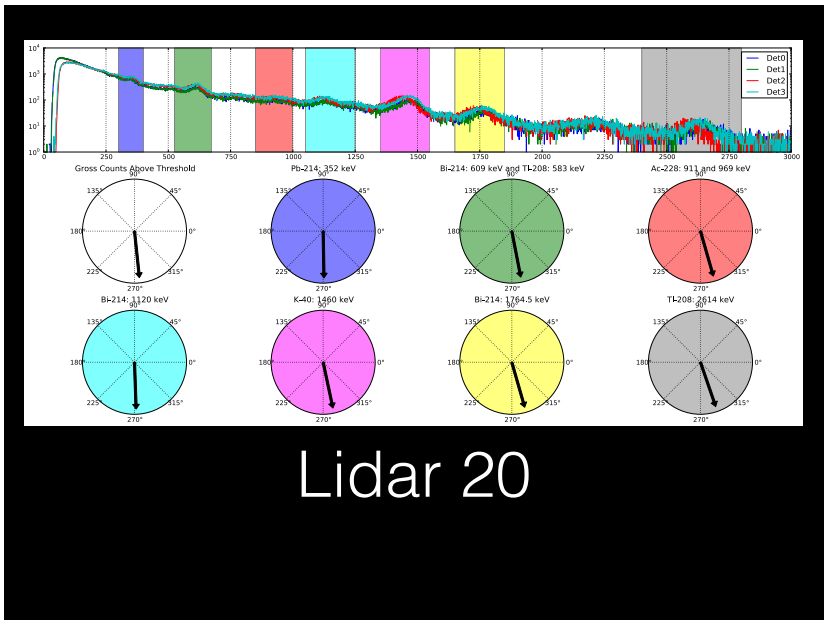


Figure A.21: Elevation Angle Results for Measurement Point 20 at Fort Indiantown Gap, Pennsylvania

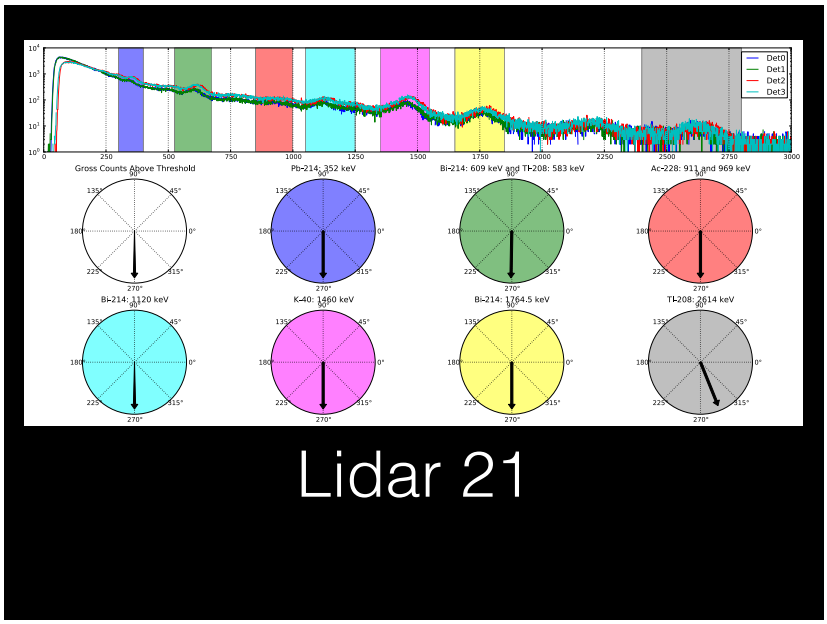


Figure A.22: Elevation Angle Results for Measurement Point 21 at Fort Indiantown Gap, Pennsylvania

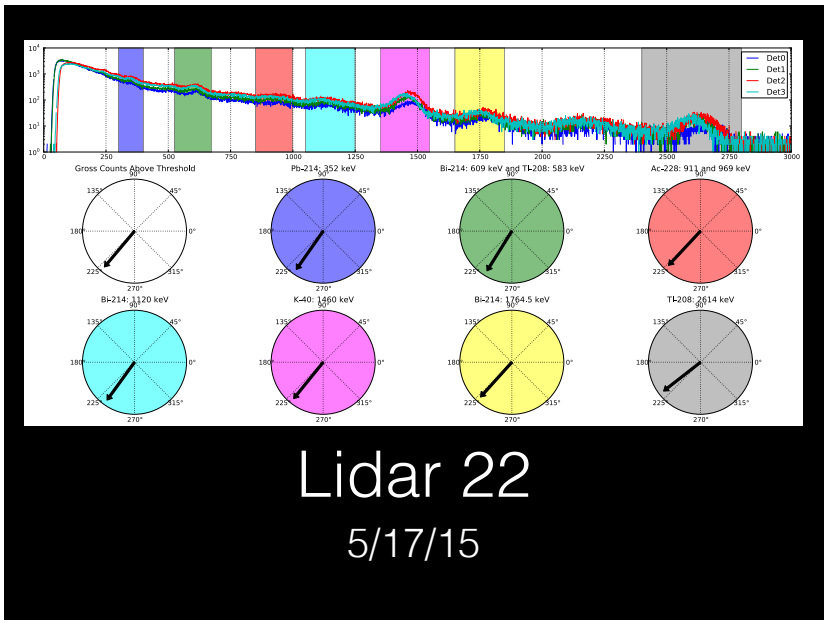


Figure A.23: Elevation Angle Results for Measurement Point 22 (05/17/15) at Fort Indiantown Gap, Pennsylvania

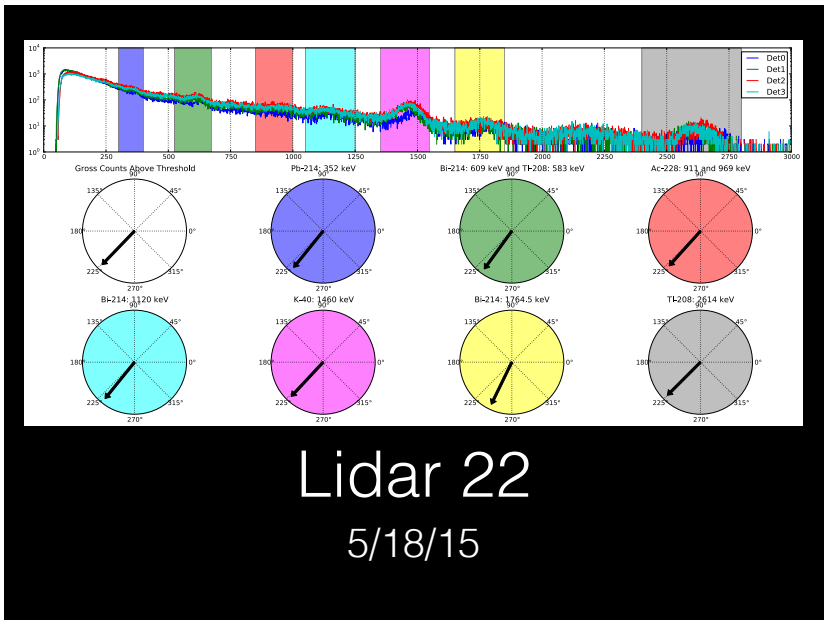


Figure A.24: Elevation Angle Results for Measurement Point 22 (05/18/15) at Fort Indiantown Gap, Pennsylvania

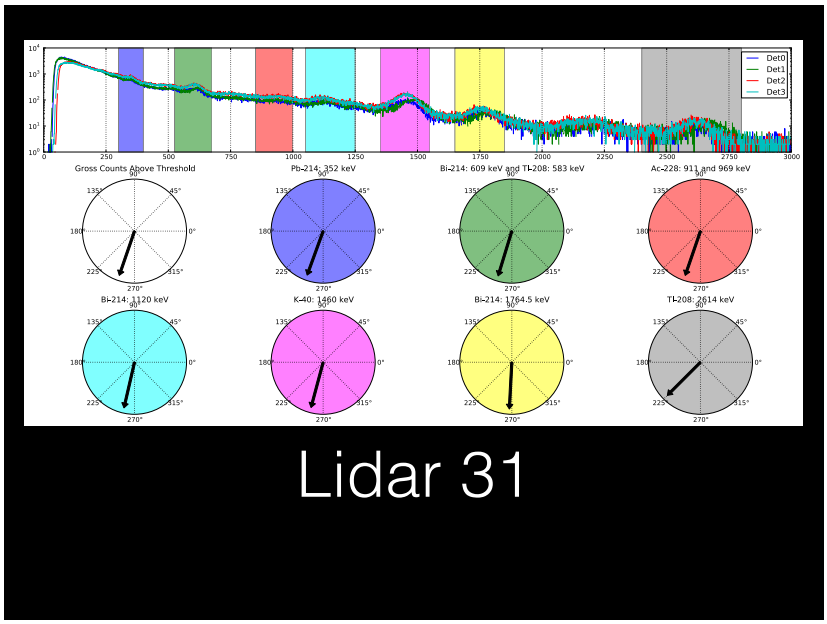


Figure A.25: Elevation Angle Results for Measurement Point 31 at Fort Indiantown Gap, Pennsylvania

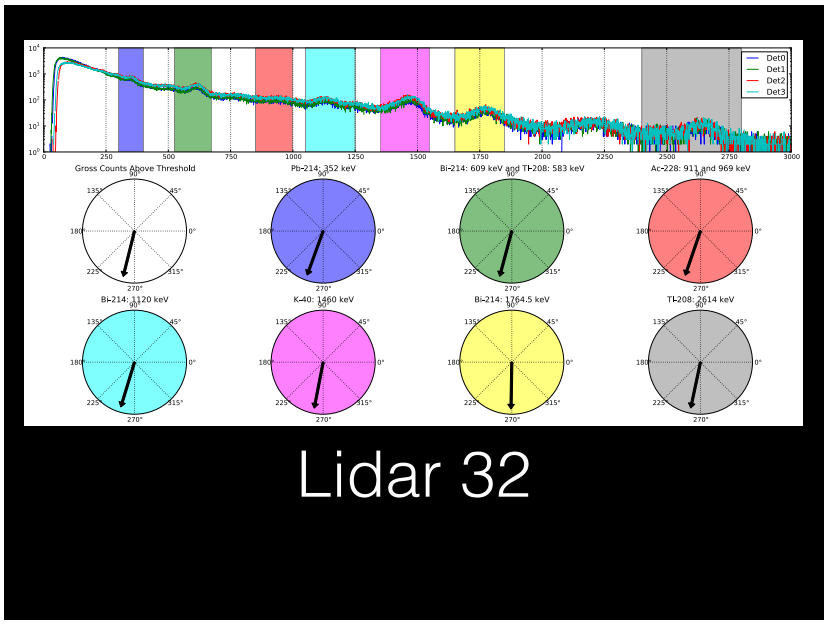


Figure A.26: Elevation Angle Results for Measurement Point 32 at Fort Indiantown Gap, Pennsylvania

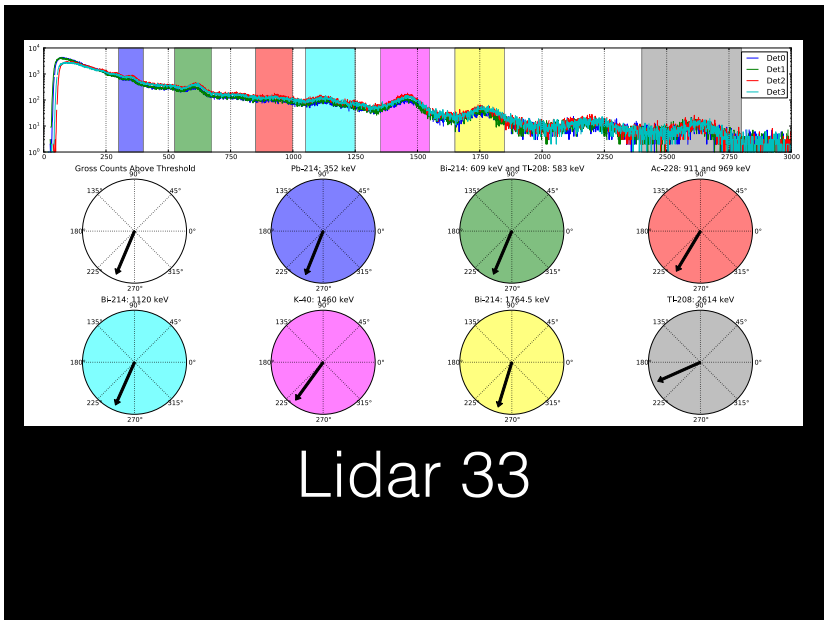


Figure A.27: Elevation Angle Results for Measurement Point 33 at Fort Indiantown Gap, Pennsylvania

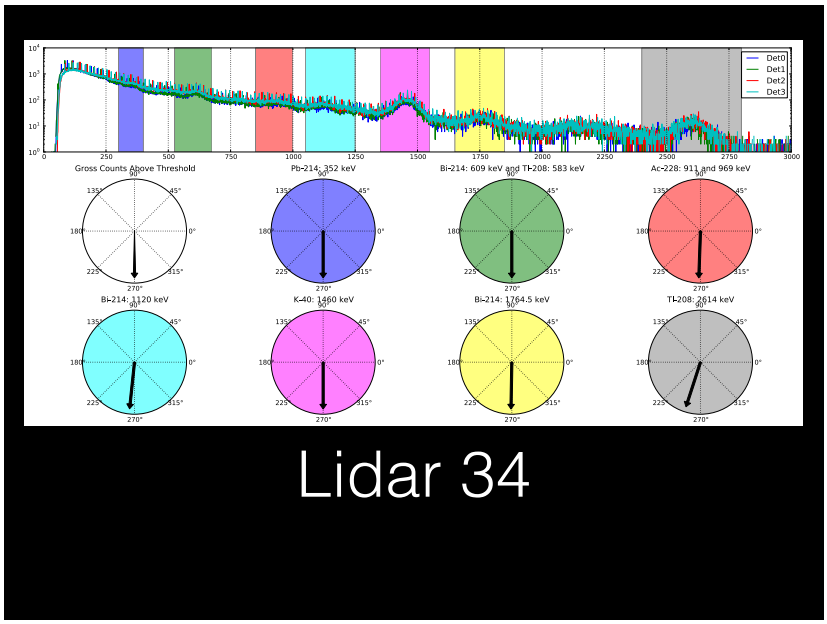


Figure A.28: Elevation Angle Results for Measurement Point 34 at Fort Indiantown Gap, Pennsylvania

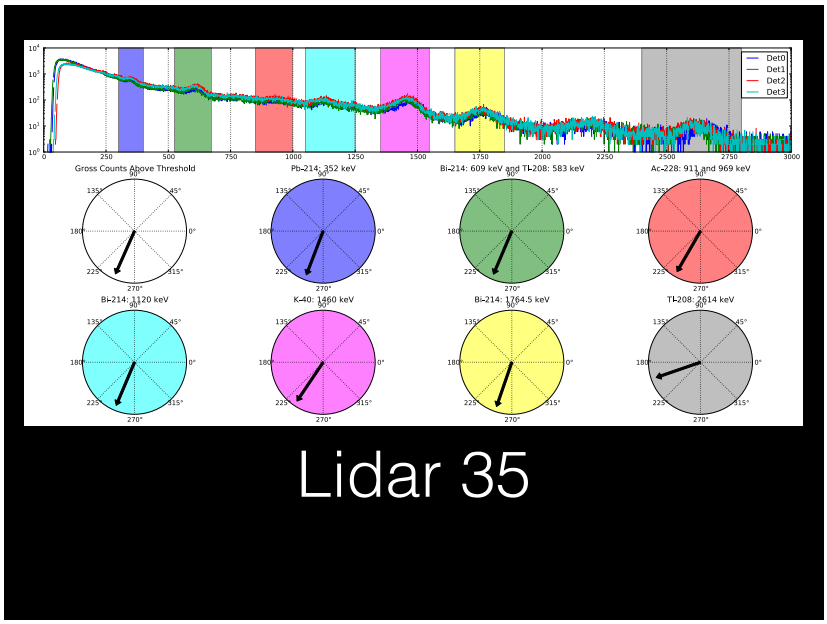


Figure A.29: Elevation Angle Results for Measurement Point 35 at Fort Indiantown Gap, Pennsylvania

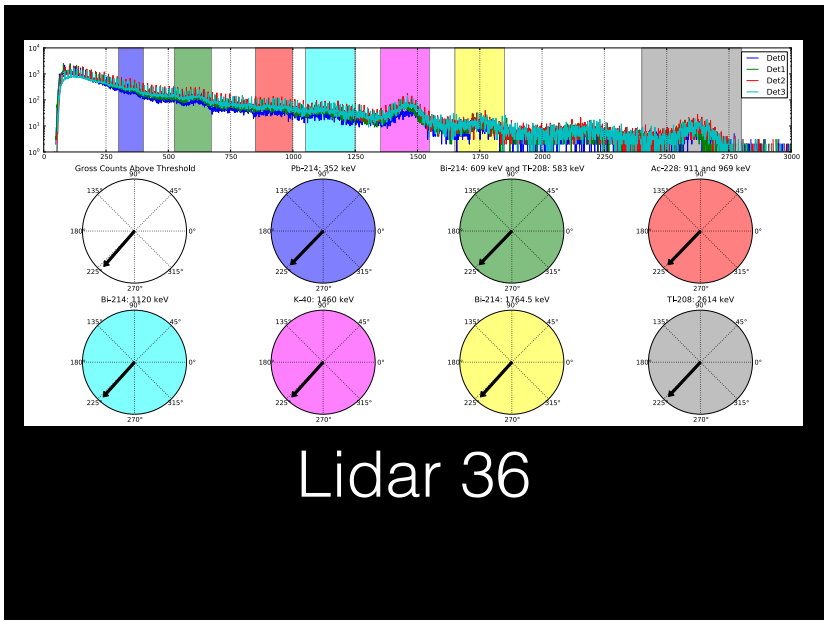


Figure A.30: Elevation Angle Results for Measurement Point 36 at Fort Indiantown Gap, Pennsylvania

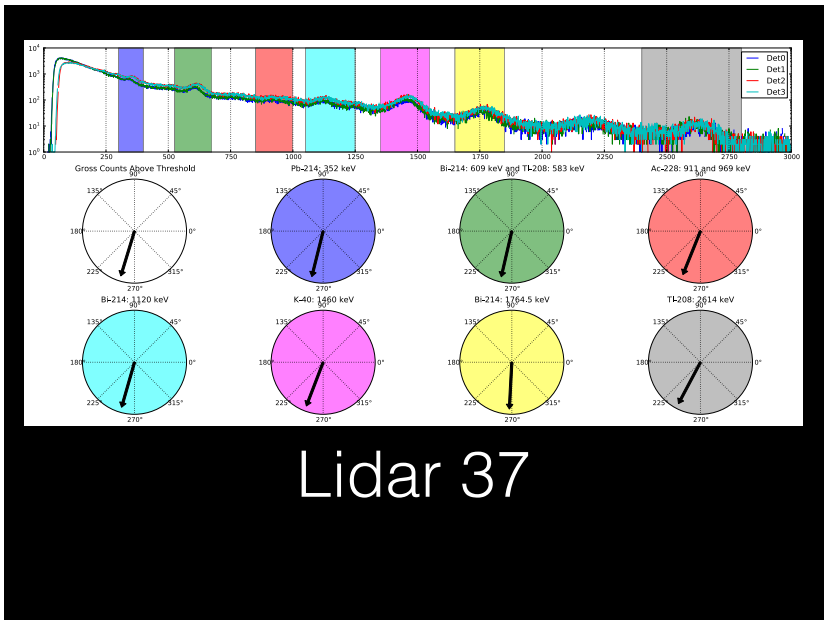


Figure A.31: Elevation Angle Results for Measurement Point 37 at Fort Indiantown Gap, Pennsylvania

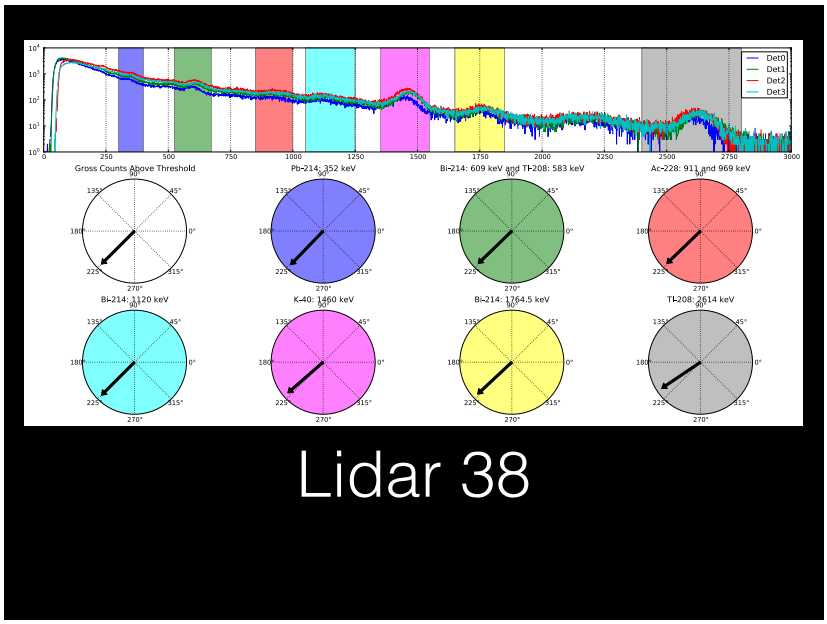


Figure A.32: Elevation Angle Results for Measurement Point 38 at Fort Indiantown Gap, Pennsylvania

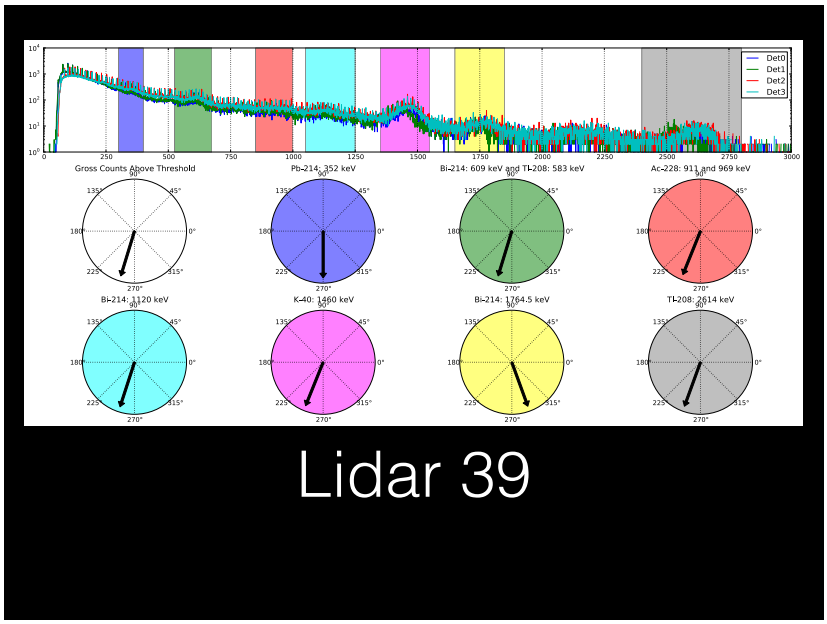


Figure A.33: Elevation Angle Results for Measurement Point 39 at Fort Indiantown Gap, Pennsylvania

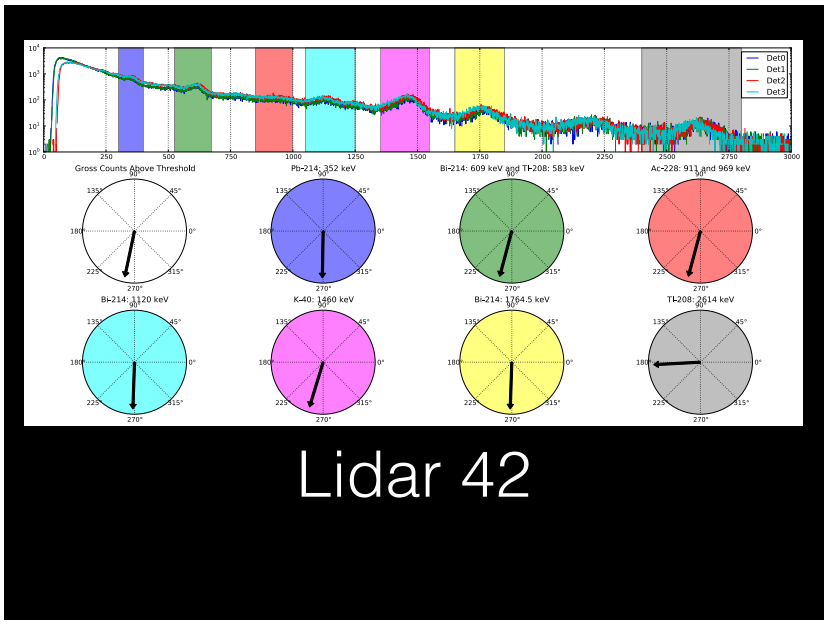


Figure A.34: Elevation Angle Results for Measurement Point 42 at Fort Indiantown Gap, Pennsylvania

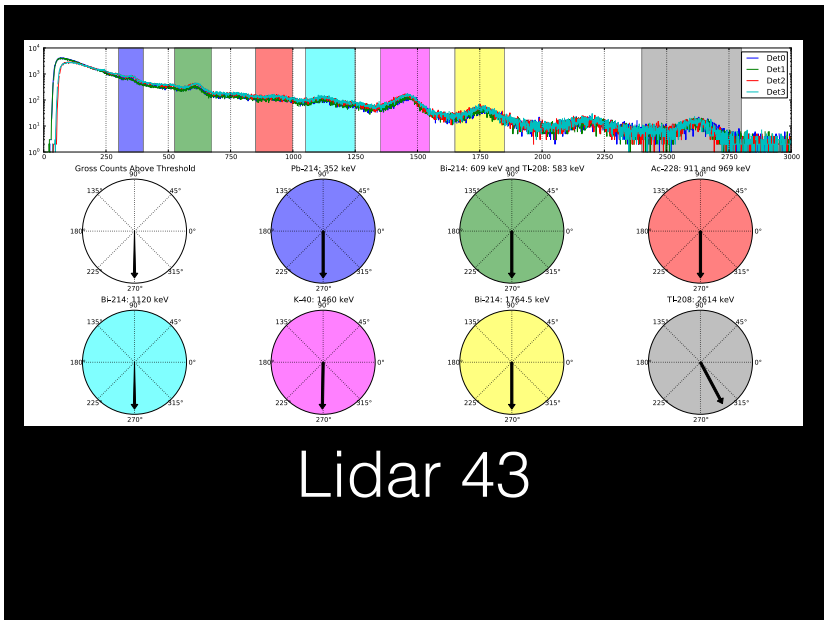


Figure A.35: Elevation Angle Results for Measurement Point 43 at Fort Indiantown Gap, Pennsylvania

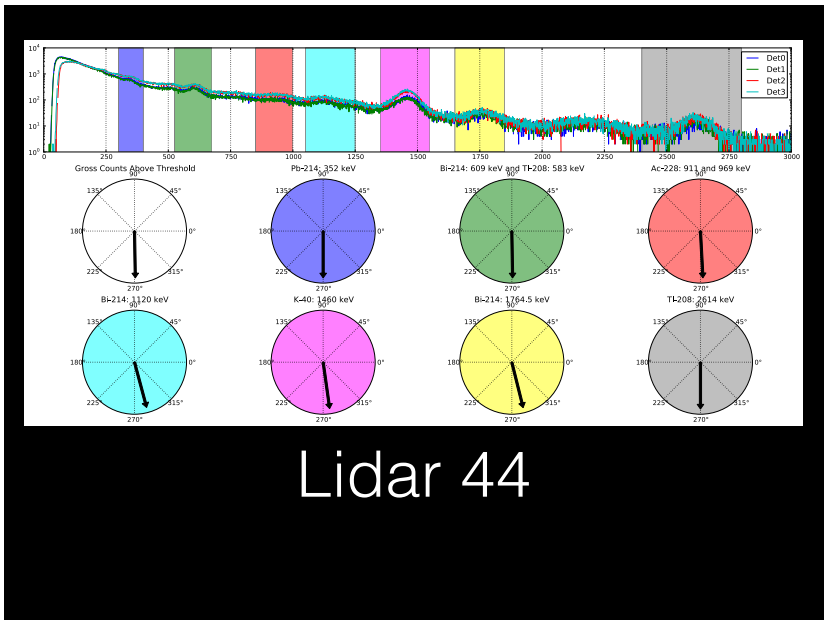


Figure A.36: Elevation Angle Results for Measurement Point 44 at Fort Indiantown Gap, Pennsylvania

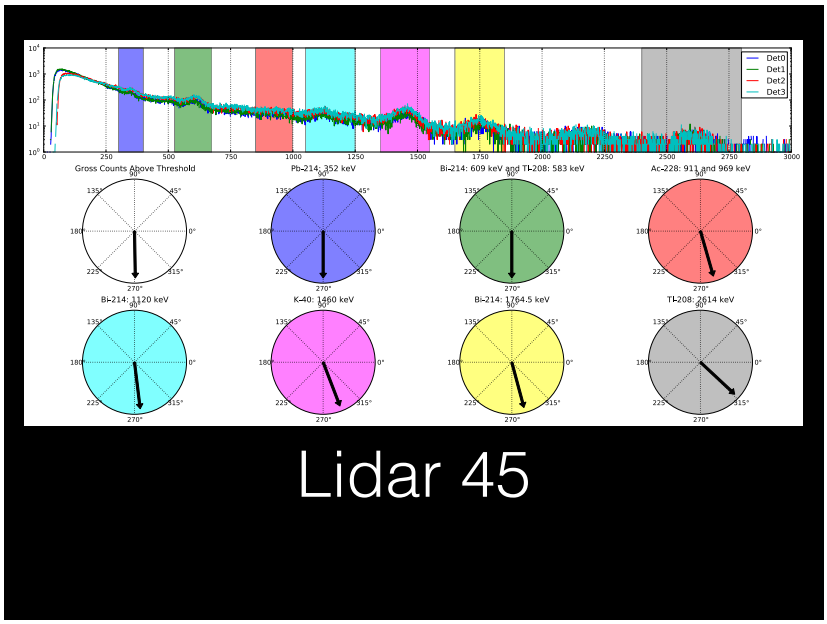


Figure A.37: Elevation Angle Results for Measurement Point 45 at Fort Indiantown Gap, Pennsylvania

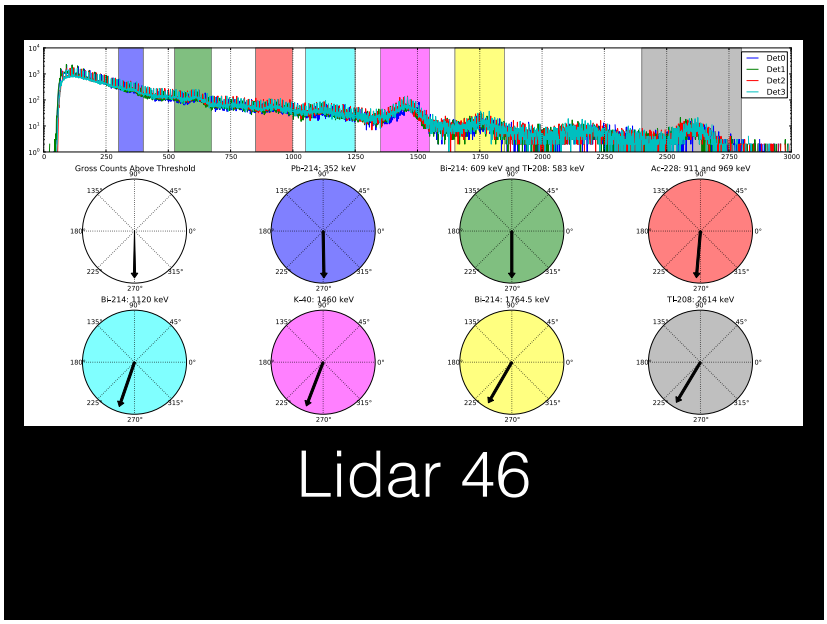


Figure A.38: Elevation Angle Results for Measurement Point 46 at Fort Indiantown Gap, Pennsylvania

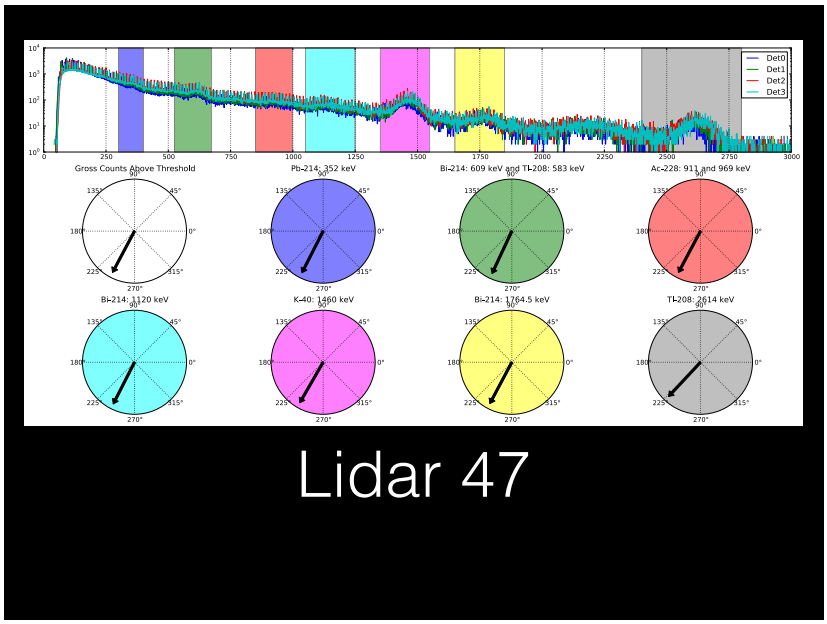


Figure A.39: Elevation Angle Results for Measurement Point 47 at Fort Indiantown Gap, Pennsylvania

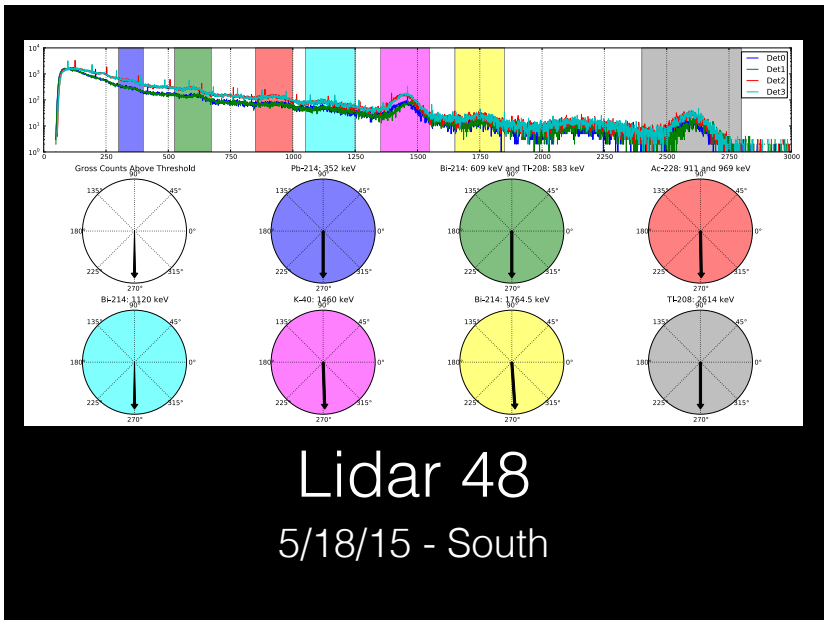


Figure A.40: Elevation Angle Results for Measurement Point 48 at Fort Indiantown Gap, Pennsylvania

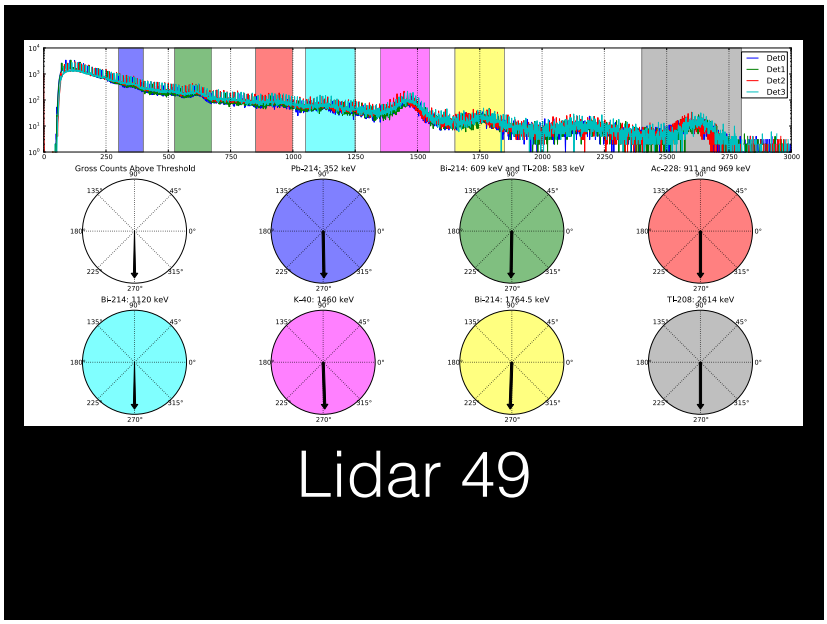


Figure A.41: Elevation Angle Results for Measurement Point 49 at Fort Indiantown Gap, Pennsylvania

Appendix B

Simulated Parking Lot Directional Results

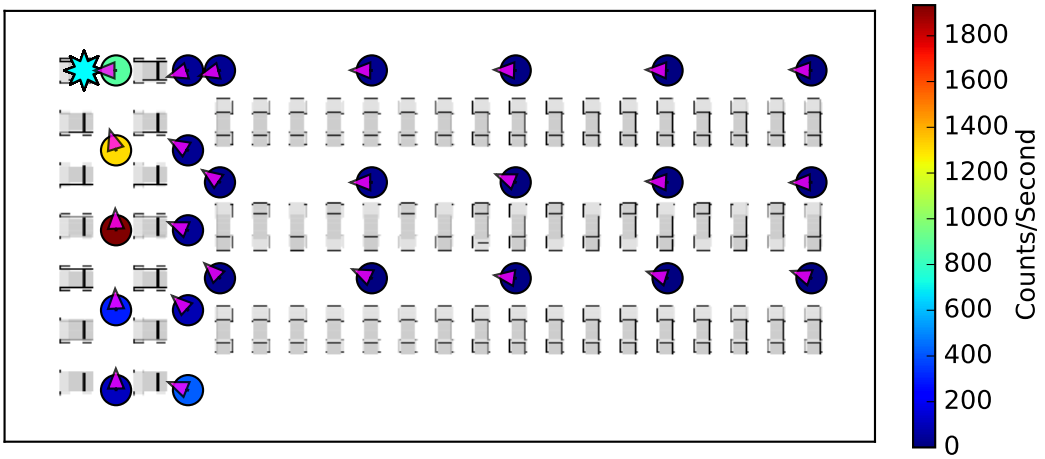


Figure B.1: Counts per Second Response and Directional Determination with Source at Location S0

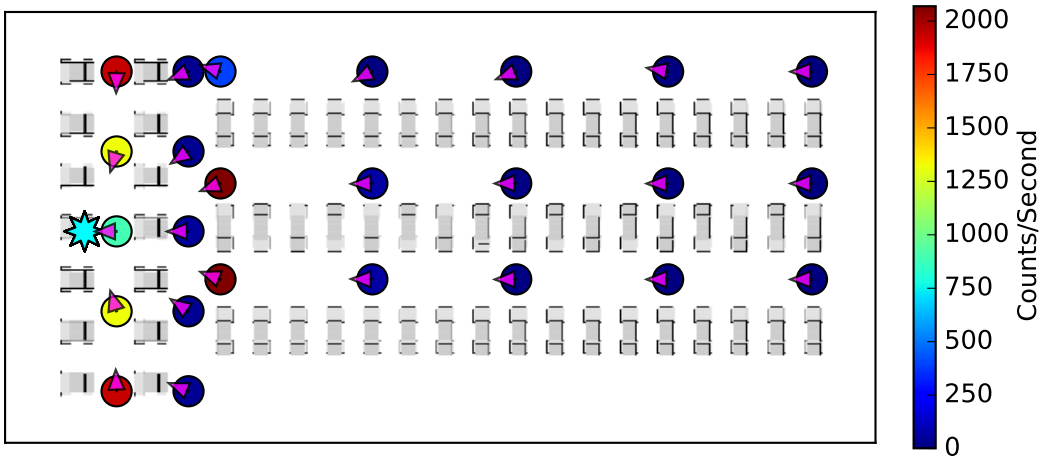


Figure B.2: Counts per Second Response and Directional Determination with Source at Location S1

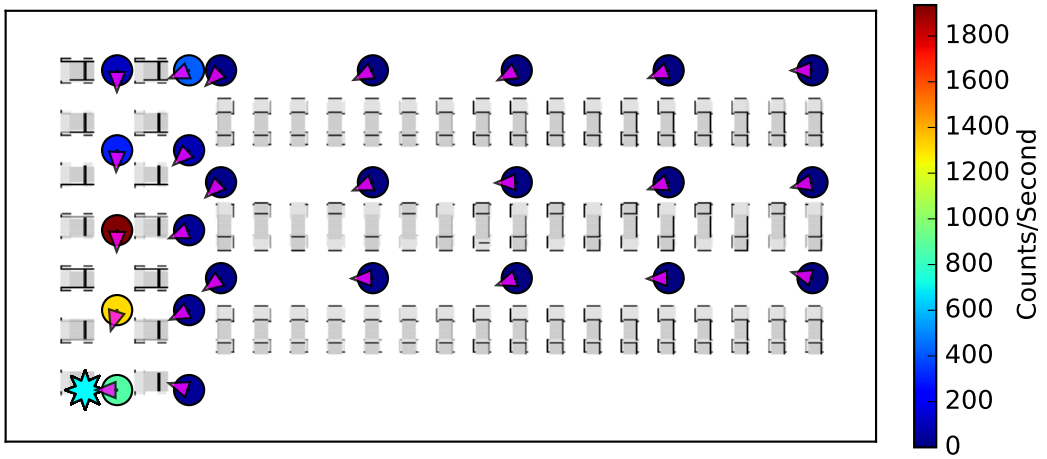


Figure B.3: Counts per Second Response and Directional Determination with Source at Location S2

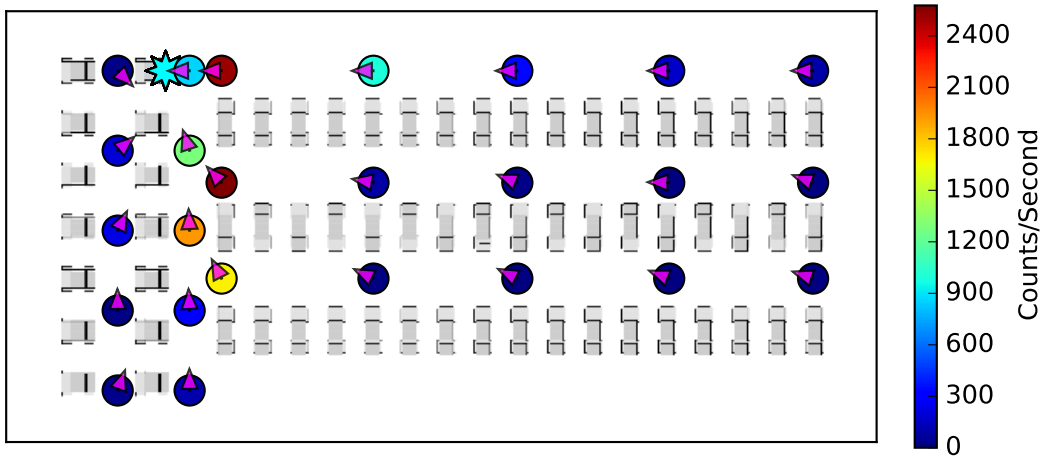


Figure B.4: Counts per Second Response and Directional Determination with Source at Location S3

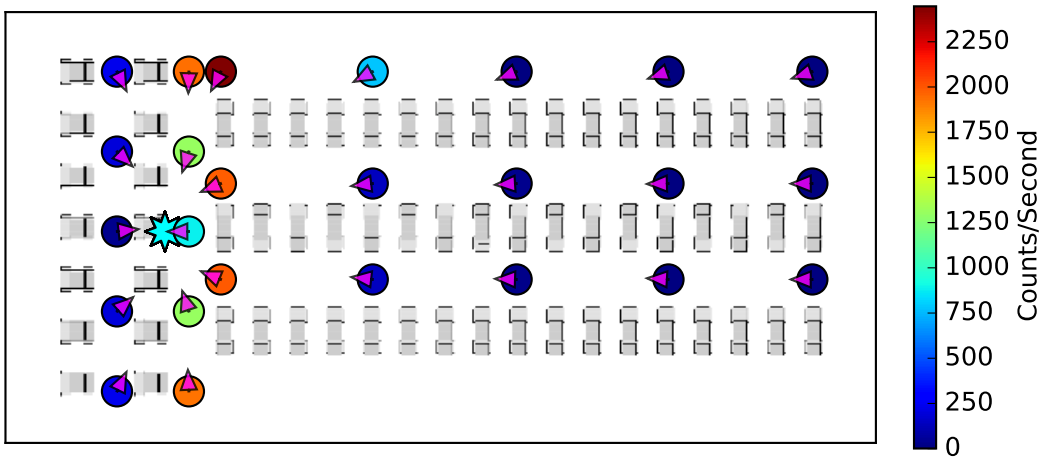


Figure B.5: Counts per Second Response and Directional Determination with Source at Location S4

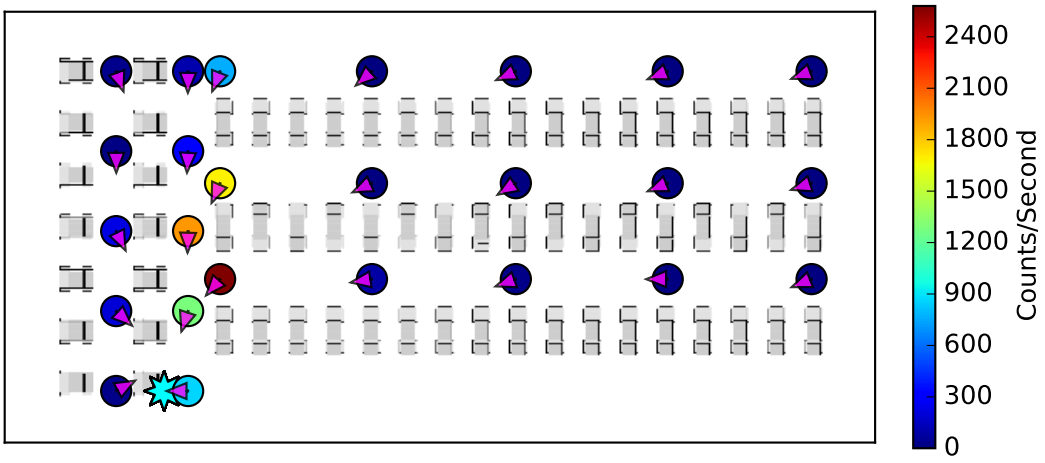


Figure B.6: Counts per Second Response and Directional Determination with Source at Location S5

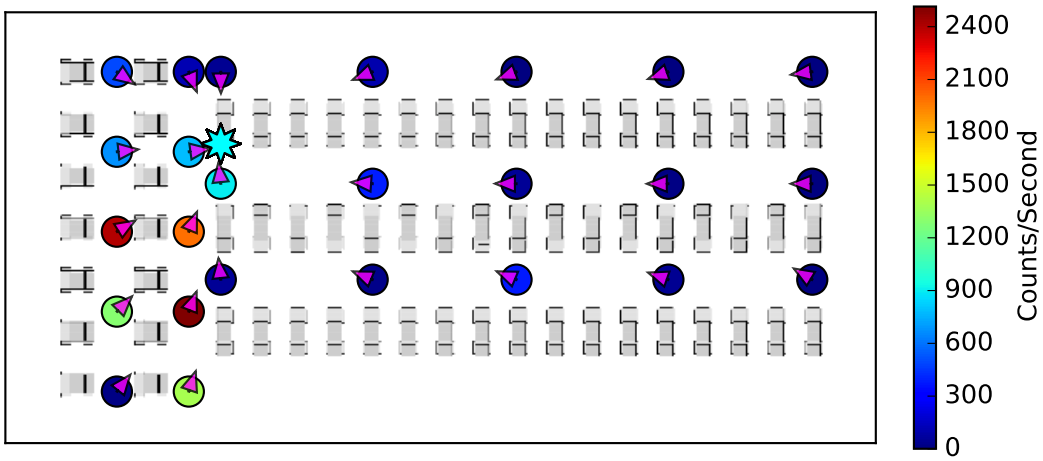


Figure B.7: Counts per Second Response and Directional Determination with Source at Location S6

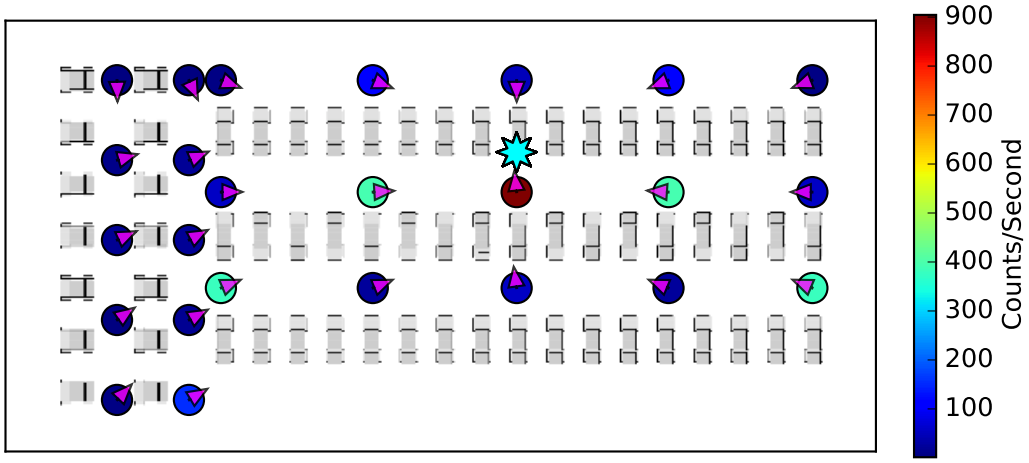


Figure B.8: Counts per Second Response and Directional Determination with Source at Location S7

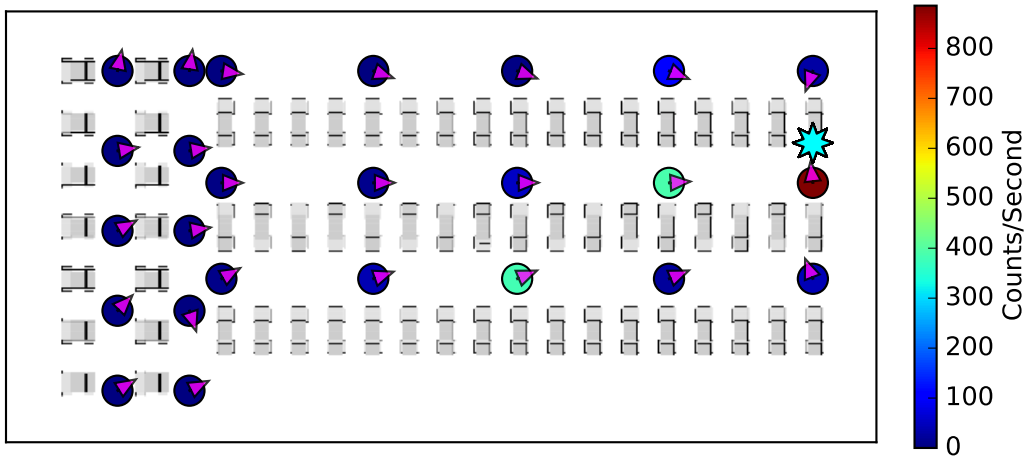


Figure B.9: Counts per Second Response and Directional Determination with Source at Location S8

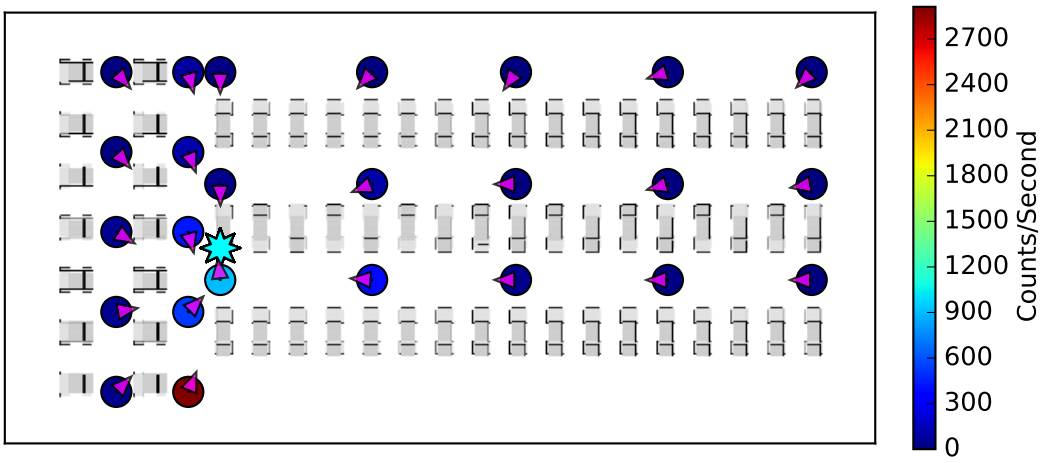


Figure B.10: Counts per Second Response and Directional Determination with Source at Location S9

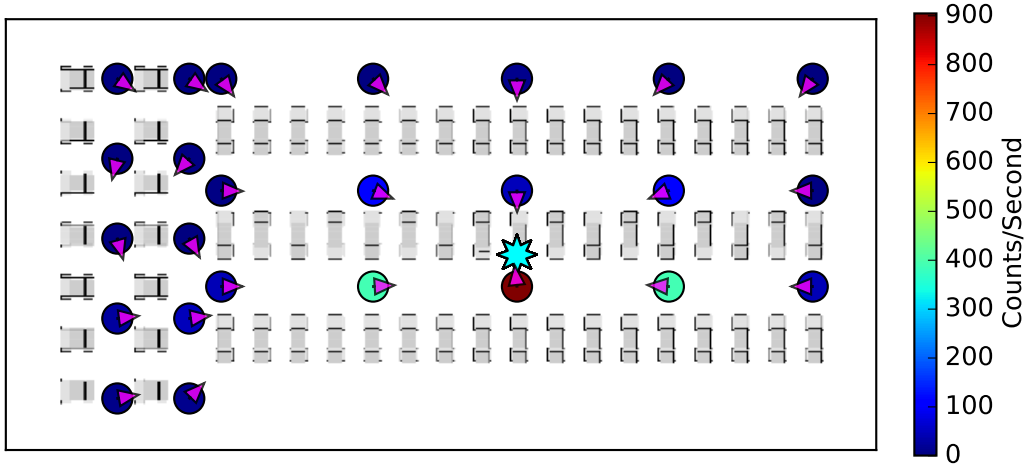


Figure B.11: Counts per Second Response and Directional Determination with Source at Location S10

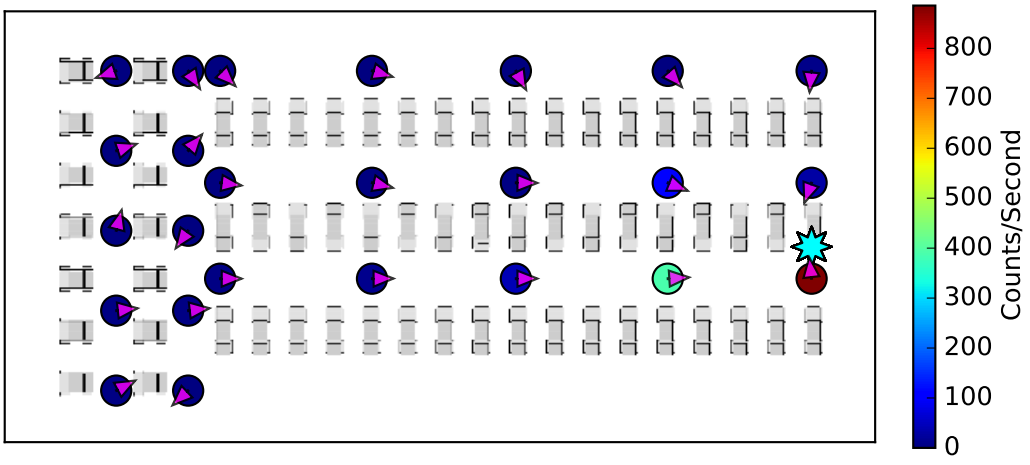


Figure B.12: Counts per Second Response and Directional Determination with Source at Location S11

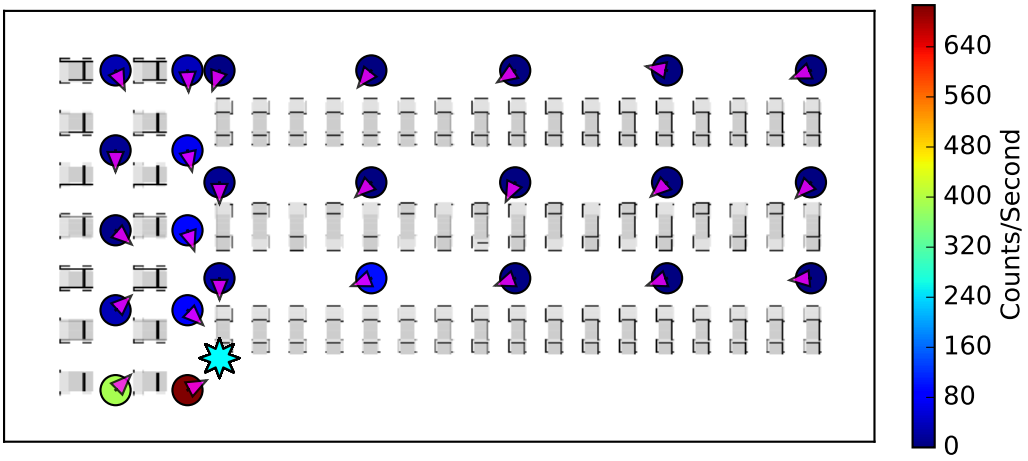


Figure B.13: Counts per Second Response and Directional Determination with Source at Location S12

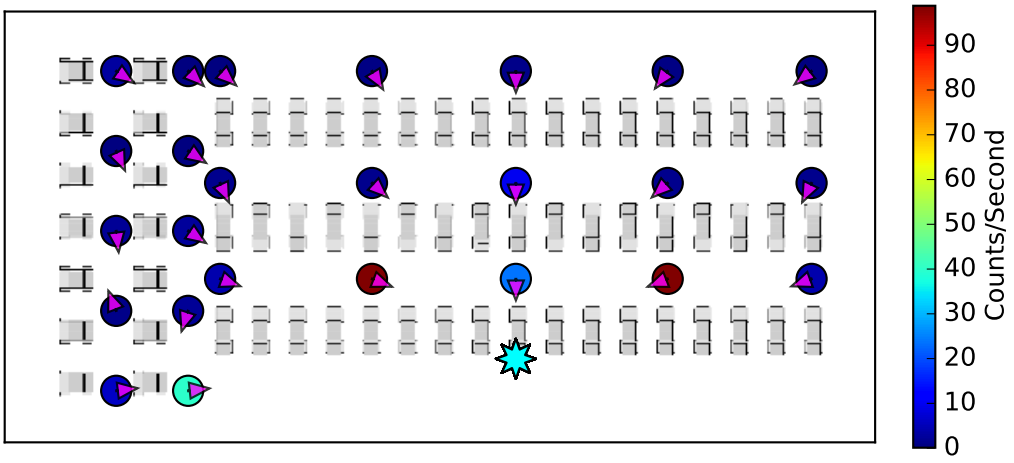


Figure B.14: Counts per Second Response and Directional Determination with Source at Location S13

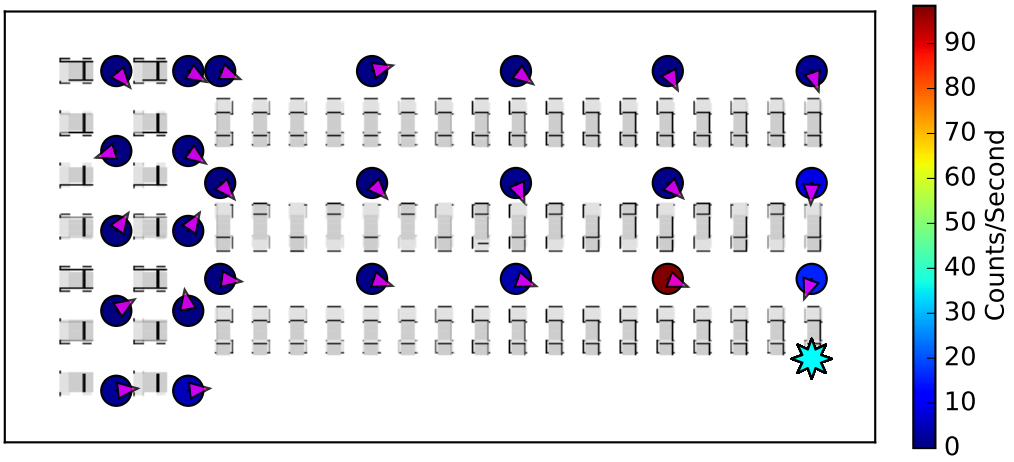


Figure B.15: Counts per Second Response and Directional Determination with Source at Location S14

Vita

Michael Willis was born in 1987 in Knoxville, Tennessee, to the family of parents Ken and Janice Willis and older brother, Jonathan. After graduating from Powell High School in 2005, Michael enrolled at the University of Tennessee.

His undergraduate work in nuclear engineering began as a path for a graduate degree in nuclear medicine. During his time as an undergraduate, however, he became interested in radiation detection and nuclear security and continued his studies in this field. In 2009, he married Kayla, and they became proud parents of a son named Colton in 2015.

Willis earned his Bachelor of Science in Nuclear Engineering degree in 2010 and went on to oursue graduate studies in nuclear engineering. His master's degree research involved the creation and laboratory testing of a novel directional radiation detection algorithm. This work was later patented under the title "System and Method for Detecting and Positioning A Radioactive Source" and assigned the patent number US 20140361190 A1.

Willis continued the development of this work for his Ph.D. The culmination of his Ph.D. research involved the further development and characterization of detection system using the fuzzy logic algorithm. He completed his Ph.D. work in 2015 and upon graduation plans to pursue a career in nuclear security, radiation detection, and safeguards.